FLUX-LIMITED DIFFUSION COEFFICIENT APPLIED TO REACTOR ANALYSIS

A Dissertation
Presented to
The Academic Faculty

By

Steven Ede Keller

In Partial Fulfillment
Of the Requirements for the Degree
Doctor of Philosophy in Nuclear and Radiological Engineering in the
School of Mechanical Engineering

Georgia Institute of Technology

August, 2007

FLUX-LIMITED DIFFUSION COEFFICIENT APPLIED TO REACTOR ANALYSIS

Approved by:

Dr. Farzad Rahnema
Nuclear and Radiological Engineering
and Medical Physics Program
Georgia Institute of Technology

Dr. Weston M. Stacey, Jr.
Nuclear and Radiological Engineering
and Medical Physics Program
Georgia Institute of Technology

Dr. Nolan E. Hertel
Nuclear and Radiological Engineering
and Medical Physics Program
Georgia Institute of Technology

Dr. Thomas D. Morley
School of Mathematics
Georgia Institute of Technology

Dr. Daniel W. Tedder
School of Chemical & Biomolecular
Engineering
Georgia Institute of Technology

Date Approved: July 5, 2007

ACKNOWLEDGEMENTS

I would first like to thank my advisor Dr. Farzad Rahnema for his years of mentorship and patience. Many thanks also go to my committee members from Georgia Tech, Dr. Weston Stacey and Dr. Nolan from the Nuclear and Radiological and Medical Physics Program , Dr. Thomas D. Morley of the School of Mathematics, and Dr. Daniel Tedder, Emeritus Professor of the School of Chemical and Biomolecular Engineering.

My final thanks go to my wife, Lucia Guadalupe Keller, and my parents, Ilona Keller and Ede Gusztav Keller. They have been very supportive of my endeavor.

CONTENTS

LIST OF TABLES

LIST OF FIGURES

SUMMARY

The purpose of this thesis is to evaluate a new definition of the diffusion coefficient used in reactor physics types of calculations. The currently used definitions encompass certain approximations, and are only accurate when used in the types of calculations they were intended. The diffusion coefficient evaluated here is based on naturally flux-limited (Levermore) diffusion theory, which has its own set of approximations, and this work determines what types of calculations it is most accurate in. Another diffusion coefficient more loosely based on flux-limited diffusion theory is also evaluated in this work.

The evaluations are performed using fine-mesh diffusion theory. They are in one spatial dimension and in 47, 4, and 2 energy groups.

The results show that the flux-limited diffusion coefficient (FD) outperforms the standard diffusion coefficient in calculations of single assemblies with vacuum boundaries, according to flux- and eigenvalue-errors. In single assemblies with reflective boundary calculations, the FD yielded smaller improvements, and tended to improve only the fast-group results, while, on average, worsened the thermal-group and eigenvalue-errors. With reflective boundaries, combinations of the FD in fast groups and the standard diffusion coefficient in thermal groups produced lower flux- and eigenvalue errors than either of the diffusion coefficients used by itself for the entire energy range.

1 INTRODUCTION

1.1 REACTOR PHYSICS CALCULATIONS

The current status of reactor core calculations can be divided into two stages; an assembly-level transport theory calculation, followed by a core-level diffusion theory calculation. A transport calculation is performed for each fuel assembly type in a fine energy group structure. This calculation outputs diffusion theory parameters by homogenizing the heterogeneous materials in and around the assembly into a single cell having a coarse group structure. Many of these homogenized cells are assembled to create a core and used as input into the diffusion code. It is presently not practical to replace this process with whole-core calculations using fine-mesh transport theory, despite recent advances in computational capability, although less computationally expensive fine-mesh diffusion theory is sometimes used.

In addition to broad group cross sections, usually in two to twenty energy groups, multigroup diffusion coefficients and/or transport cross sections are provided by the transport calculation. The diffusion coefficient is important in diffusion theory calculations because it accounts for the anisotropy of the scattering and cell-leakage. An exact relation exists for the diffusion coefficient in one energy group, but no such relation exists for more than one energy group. This can be seen in the definition of the energy dependent diffusion coefficient,

$$D(\mathbf{r},E)=\frac{1}{3}\left[\Sigma_t\left(\mathbf{r},E\right)-\frac{\int_0^\infty \Sigma_{s1}(E'\rightarrow E)J(\mathbf{r},E')\,dE}{\int_0^\infty J(\mathbf{r},E')\,dE}\right]^{-1} \tag{1.1}$$

where the current *J(**r**,E)* is unknown, and from its multigroup definition

$$\nabla\cdot D_g(\mathbf{r})\nabla\phi_g(\mathbf{r})\equiv\int_{E_{g-1}}^{E_g} dE\nabla\cdot D(\mathbf{r},E)\nabla\phi(\mathbf{r},E)\quad , \tag{1.2}$$

which has no exact analytical solution. But because of the significance of the diffusion coefficient, many methods of estimating it have been developed, with each one presenting a different level of accuracy or specialization to a certain type of application. In addition, the various definitions are not always in agreement, and the choice of which one to use may require an extensive analysis of the case under consideration.

1.2 STANDARD DIFFUSION COEFFICIENT AND DIFFUSION THEORY LIMITATIONS

One widely used diffusion coefficient is defined as

$$D_g\left(r\right)=\frac{1}{3\left(\sigma_{tr,g}\left(r\right)\right)} \tag{1.3}$$

with

$$\sigma_{tr,g}=\sigma_{t,g}-\sigma_{1,g\rightarrow g}\quad , \tag{1.4}$$

where $\sigma_{1,g\rightarrow g}$ is the first order Legendre moment of scattering, and its presence accounts for linearly anisotropic scattering only for self-scattering, which presents a limitation of this definition of the transport cross section. Because this definition is widely used, in

this work it will be referred to as the standard transport cross section (Std), and used as a point of comparison for the new methods examined in this thesis.

A limitation of diffusion theory that is often overlooked is related to the use of Fick's Law,

$$\mathbf{J} = -\mathrm{D}\nabla\phi \quad , \tag{1.5}$$

in the diffusion equation used to relate the neutron current to the scalar flux. Fick's Law is a first order approximation, not an exact definition. One consequence of this approximation occurs in regions of a large spatial gradient, where the right hand side of Eq. (1.5) becomes large, causing the left hand side, the current, to also become large to the point where its magnitude is greater than the scalar flux. However, based on the exact analytical definitions of the neutron current,

$$\boldsymbol{J} = \int_{4\pi} d\Omega \Omega \psi(\Omega) \quad , \tag{1.6}$$

and the scalar flux,

$$\phi = \int_{4\pi} d\Omega \psi(\Omega) \quad , \tag{1.7}$$

where $\psi(\Omega)$ is the angular flux, the magnitude of the current must always be less than or equal to the scalar flux. To see this, consider that in the integrand of Eq. (1.6), the unit vector Ω has positive and negative values as it spans 4π steradians, and is multiplied by the value of $\psi(\Omega)$ that points in the same direction as Ω is pointing in. When the integral of this product is compared to the integral in Eq. (1.7), the latter integral will be greater because its integrand doesn't have any negative values in it. Another way to explain this is with a simple one-dimensional example, representing the two possible extremes. If two neutrons are traveling to the right, and two to the left, the application of Eq. (1.6)

yields zero neutron current. If all four neutrons are traveling to the right, or to the left, the magnitude of the neutron current is four neutrons (per unit area per second). In both cases the scalar flux is four neutrons (per unit area per second), with the current being less than the scalar flux in the first case (the isotropic extreme), and exactly equal to the scalar flux in the second case (the monodirectional extreme).

This work evaluates a novel method to estimate a diffusion coefficient based on flux-limited diffusion theory (FDT) that has neither of the shortcomings of the standard transport cross section described in Eq. (1.4) above, that is the lack of anisotropic scattering across all energy groups and, more significantly, the calculation of a neutron current whose magnitude exceeds the scalar flux. It evaluates the new diffusion coefficient and another transport cross section that is more loosely based on FDT alongside the standard transport cross section by comparing them against transport benchmarks.

2 PROPOSED METHOD

The primary feature of the new diffusion coefficient investigated in this thesis is its ability to prevent the neutron current calculated with it using Fick's Law from exceeding the scalar flux, a property known as flux-limiting. FDT has, and continues to have, great success in the field of radiative transfer (Szilard and Pomraning 1992). These diffusion coefficients usually contain a gradient term that adjusts the diffusion coefficient, so that as the gradient becomes large flux-limiting is enforced. Some of these diffusion coefficients are *ad hoc* in nature that perform well for specific applications (Olson, Auer, and Hall 2000), but the FDT examined here is naturally flux-limited diffusion theory developed by Levermore and Pomraning (1981), sometimes referred to as Levermore diffusion theory. This was adapted to multigroup neutron diffusion by Pomraning (1984), which serves as the basis for the work here. It was modified to be used in one spatial dimension and has the external source replaced by a fission term.

2.1 BRIEF DERIVATIONS AND DESCRIPTIONS OF FLUX-LIMITED PARAMETERS

A brief introduction to the flux-limited diffusion coefficient, with notes of major assumptions and the final equations solved, is given in this subsection. For a detailed derivation refer to the APPENDIX.

2.1.1 Flux-limited Diffusion Coefficient $\left(D^{FD}\right)$

The starting point is the time-independent multigroup transport equation,

$$\begin{aligned}\boldsymbol{\Omega}\cdot\nabla I_g\left(\boldsymbol{r},\boldsymbol{\Omega}\right)+\sigma_g I_g\left(\boldsymbol{r},\boldsymbol{\Omega}\right)=\sum_{g'=1}^{G}\int_{4\pi}d\boldsymbol{\Omega}'\sigma_{s,g'\to g}\left(\boldsymbol{\Omega}'\cdot\boldsymbol{\Omega}\right)I_{g'}\left(\boldsymbol{r},\boldsymbol{\Omega}'\right)+\\ \frac{1}{k}\frac{X_g\left(r\right)}{4\pi}\sum_{g'=1}^{G}\nu_{g'}\left(r\right)\sigma_{f,g'}\left(r\right)\int_{4\pi}d\boldsymbol{\Omega}'I_{g'}\left(\boldsymbol{r},\boldsymbol{\Omega}'\right)\quad,\end{aligned}\tag{2.1}$$

its angle-integrated result, the time-independent multigroup conservation equation

$$\nabla\cdot\boldsymbol{J}_g+\sigma_g\phi_g\left(\boldsymbol{r}\right)=\sum_{g'=1}^{G}\sigma_{0,g'\to g}\phi_{g'}\left(\boldsymbol{r}\right)+\frac{1}{k}X_g\left(r\right)\sum_{g'=1}^{G}\nu_{g'}\left(r\right)\sigma_{f,g'}\left(r\right)\phi_{g'}\quad,\tag{2.2}$$

the separation of the angular flux $I_g(\mathbf{r},\boldsymbol{\Omega})$ into two components as

$$I_g(\mathbf{r},\boldsymbol{\Omega})=\phi_g(\boldsymbol{r})\psi_g(\mathbf{r},\boldsymbol{\Omega})\quad,\tag{2.3}$$

where $\phi_g(\boldsymbol{r})$ is the scalar flux with its usual definition

$$\phi_g=\int_{4\pi}d\boldsymbol{\Omega}I_g(\boldsymbol{\Omega})\quad,\tag{2.4}$$

and the normalization of the angular flux $\psi_g(\mathbf{r},\boldsymbol{\Omega})$ as

$$\int_{4\pi}d\Omega\psi_g(\mathbf{r},\boldsymbol{\Omega})=1\quad.\tag{2.5}$$

The assumption is made that the spatial and energy dependencies of $I_g\left(\boldsymbol{\Omega}\right)$ are carried mostly by the scalar flux $\phi_g\left(\boldsymbol{r}\right)$, which implies that

$$\boldsymbol{\Omega}\cdot\nabla\psi_g=0\tag{2.6}$$

and

$$\psi_g=\psi_{g'}\quad.\tag{2.7}$$

With a reduction to one spatial dimension, one arrives at the set of equations

$$\left(1+\lambda_g R_g^2-\mu R_g\right)\psi_g\left(\mu\right)=\frac{1}{2}+\sum_{n=1}^{N}\left(\frac{2n+1}{2}\right)P_n(\mu)K_{n,g}\psi_{n,g} \quad , \tag{2.8}$$

where

$$\lambda_g=\frac{1}{R_g}\left\{\coth\left[\frac{R_g}{1-\hat{\mu}_g}\right]-\frac{1-\hat{\mu}_g}{R_g}\right\} \quad , \tag{2.9}$$

with

$$\hat{\mu}_g=\frac{\sum_{g'=1}^{G}\phi_{g'}\sigma_{1,g'\to g}}{\sum_{g'=1}^{G}\phi_{g'}\sigma_{0,g'\to g}+\frac{1}{k}X_g\sum_{g'=1}^{G}\phi_{g'}\nu_{g'}\sigma_{f,g'}} \quad , \tag{2.10}$$

$$R_g\left(x\right)=\frac{-d\phi_g/dx}{\sigma_g\left(x\right)\omega_g\left(x\right)\phi_g\left(x\right)} \quad , \tag{2.11}$$

where

$$\omega_g\left(x\right)= \frac{1}{\sigma_g\left(x\right)\phi_g\left(x\right)}\left(\sum_{g'=1}^{G}\sigma_{0,g'\to g}\left(x\right)\phi_{g'}\left(x\right)+\frac{1}{k}X_g\left(x\right)\sum_{g'=1}^{G}\nu_{g'}\left(x\right)\sigma_{f,g'}\left(x\right)\phi_{g'}\left(x\right)\right) \quad , \tag{2.12}$$

and $K_{n,g}$ is the nth order Legendre polynomial,

$$K_{n,g}=\int_{-1}^{1}d\xi P_n(\xi)K_g(\xi) \quad , \tag{2.13}$$

of the Legendre expansion for the expression

$$K_g\left(\mu'\cdot\mu\right)=\frac{2\pi}{\sigma_g\omega_g\phi_g}\left[\sum_{g'=1}^{G}\phi_{g'}\sigma_{s,g'\to g}\left(\mu'\cdot\mu\right)+\frac{1}{k}\frac{X_g}{4\pi}\sum_{g'=1}^{G}\phi_{g'}\nu_{g'}\sigma_{f,g'}\right] \quad . \tag{2.14}$$

With the only unknown in Eq. (2.8) being $\psi_g\left(\mu\right)$, it is assumed that it can be adequately approximated by the function

$$\psi_g(x,\mu) = \frac{1-\hat{\mu}_g}{2\left[1+\lambda_g R_g^2 - \mu R_g - \hat{\mu}_g\right]} \quad . \tag{2.15}$$

One can combine these terms to yield a spatially-dependent flux-limited diffusion coefficient as

$$D_g^{FD}(x) = \frac{-\phi_g(x)}{d\phi_g/dx} \times$$
$$\left\{ \coth\left[\frac{-d\phi_g/dx}{\sum_{g'=1}^{G}\phi_{g'}\sigma_{0,g'\to g} - \sum_{g'=1}^{G}\phi_{g'}\sigma_{1,g'\to g} + \frac{1}{k}X_g\sum_{g'=1}^{G}\phi_{g'}\nu_{g'}\sigma_{f,g'}} \right] \right. \tag{2.16}$$
$$\left. + \frac{\sum_{g'=1}^{G}\phi_{g'}\sigma_{0,g'\to g} - \sum_{g'=1}^{G}\phi_{g'}\sigma_{1,g'\to g} + \frac{1}{k}X_g\sum_{g'=1}^{G}\phi_{g'}\nu_{g'}\sigma_{f,g'}}{d\phi_g/dx} \right\} \quad .$$

This flux-limited diffusion coefficient will be referred to as FD. Note than in Eqs. (2.16) and the presence of the first order Legendre moment for scattering, $\sigma_{1,g'\to g}$, which accounts for linearly anisotropic across all groups. This diffusion coefficient has been shown analytically (Pomraning 1981) to be flux-limited, that is, a neutron current calculated by using it in Fick's Law will never exceed the scalar flux. This property will be confirmed computationally in this thesis.

Note also the presence of the gradient term of the scalar flux. Because the gradient is not typically output by transport lattice and cross section codes, the method used in this thesis to calculate it requires examination of its accuracy.

2.1.2 "Flux-limited" Transport Cross Section $\left(\sigma^{FX}\right)$

By starting with the assumptions of Eq. (2.3), Eq. (2.7), and the P_1 approximation to the transport equation, it is possible to derive a "flux-limited" transport cross section (FX) as

$$\sigma_{tr,g}^{FX} = \sigma_g - \sum_{g'=1}^{G} \sigma_{1,g'\to g} \left(\frac{\phi_{g'}}{\phi_g} \right) \quad . \tag{2.17}$$

Flux-limited is enclosed in quotation marks to indicate that it has never been shown analytically that the transport cross section in Eq. (2.17) actually is flux-limited. It will be determined in this thesis if it is. The FX has the advantage over the FD that it is much simpler to calculate.

2.2 DIFFUSION COEFFICIENT EVALUATION PROCESS AND COMPUTATIONAL MODELS

The performance of the flux-limited diffusion coefficient from Eq. (2.16), D^{FD}, also referred to as FD, the possibly flux-limited transport cross section from Eq. (2.17), σ_{tr}^{FX}, referred to as FX, and the standard transport cross section in Eq. (1.4), referred to as Std, were evaluated with fine-mesh diffusion calculations. The output, described in section 4, based on each type of diffusion coefficient were concurrently compared against a transport benchmark. All computations and the analytical methods they are based on use one spatial dimension.

There were calculations using individual single-assemblies of 4 types, each with varying levels of heterogeneity, modeled one at a time, and three core types consisting of

combinations of these assemblies. Each of the four individual assembly types were modeled with vacuum boundary conditions and with reflective boundary conditions on both sides of the assembly, on a fine-mesh. The full-core calculations all had vacuum boundary conditions. The diagrams of the assemblies, cores, and their components are shown in Figure 2.1.

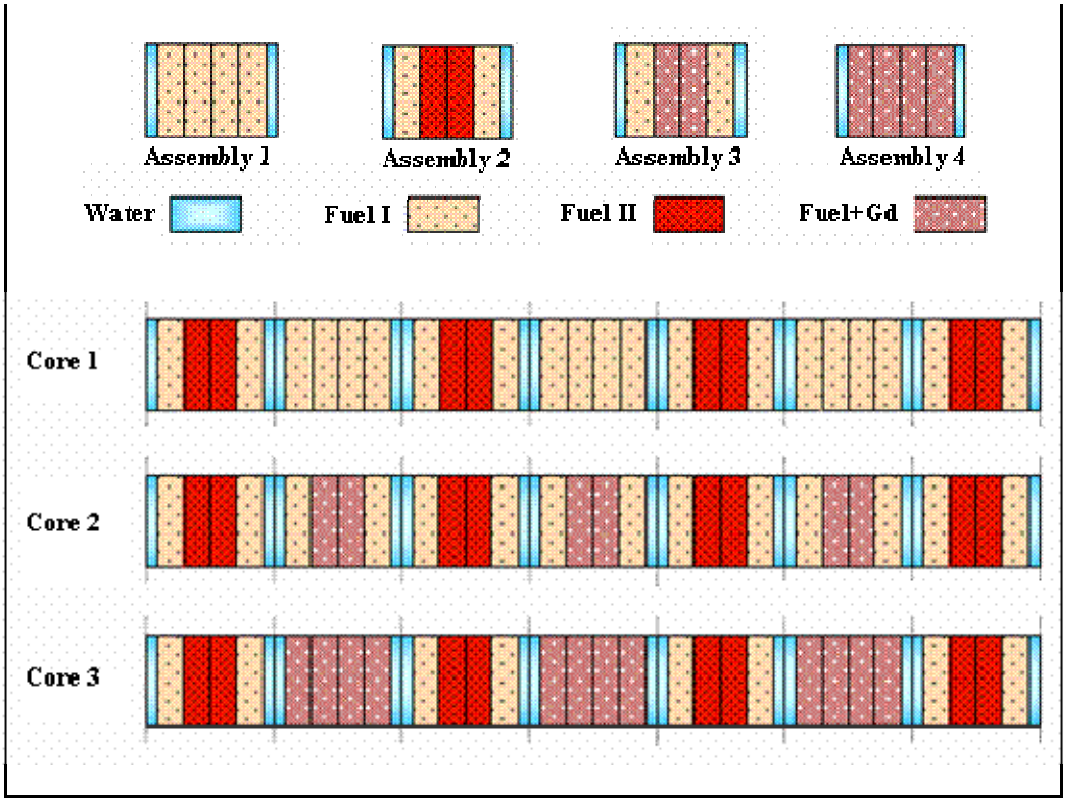

Figure 2.1: Assembly and core types used in the calculations.

Each assembly consists of 4 fuel regions composed of fuel type I or II, or a fuel and gadolinium mixture, bordered by water channels. Each fuel region is divided into sixteen 0.2032 cm subregions, and each water region is divided into sixteen 0.06985 cm

subregions, for a total of 96 subregions, and a width of 15.24 cm (6 in) per assembly. This spatial discretization is used in the transport benchmark and fine-mesh diffusion models.

Three energy structures were used for the diffusion and transport calculations, a 47-group, a 4-group, and a 2-group structure, with the 4- and 2-groups being subsets of the 47-groups. The use of the same energy structures and cross sections for the transport and fine-mesh diffusion calculations allowed direct comparisons to be made between the calculations, with the only difference among them being their diffusion or transport theory bases.

3 LITERATURE REVIEW

There have been many previous definitions of the diffusion coefficient for infinite uniform lattices and homogeneous regions, based on deterministic as well as Monte Carlo methods. Their applicability depends on many factors, such as the type of calculation being performed, parameter to be conserved, and problem geometry.

3.1 DETERMINISTIC METHODS FOR THE DIFFUSION COEFFICIENT

3.1.1 *B-1* and *B-3* Buckling Dependent Methods

One of the most frequently used methods to calculate a diffusion coefficient for a single homogenized lattice cell in a critical spectrum is the *B-1* method (Stamm'ler and Abbate 1983, 360). The angular flux is separated into spatial and angle-energy modes as

$$\Psi_g(\vec{\mathbf{r}}, E, \mu) = \sum_n F_{n,g}(E, \mu)\phi_{n,g}(\vec{\mathbf{r}}) \tag{3.1}$$

where n is set to equal 1 assuming the fundamental mode, in which case

$$\Psi_g(\vec{\mathbf{r}}, E, \mu) = F_g(E, \mu)\phi_g(\vec{\mathbf{r}}) \quad . \tag{3.2}$$

The angular dependence of $F_g(E, \Omega)$ is expanded in Legendre polynomials to first order, with its zeroth order moment being, for group g,

$$\psi_g = 2\pi \int F_g(E, \mu)\, d\mu \quad , \tag{3.3}$$

and the diffusion coefficient for group g is then calculated as

$$D_g = \frac{\pm \mathrm{i}\, J_g^{\pm}}{|B_1|\psi_g} \quad . \tag{3.4}$$

The critical buckling B_1 is found by first inserting Eq. (3.2) into the transport equation, separating the results into solutions for $\phi_g(\vec{r})$ and $F_g(E,\mu)$. The solution for $\phi_g(\vec{r})$ is $\phi_g(\vec{r}) = \exp[\mathrm{i}B\vec{r}]$, and $F_g(E,\mu)$ is expanded in first order Legendre polynomials. The resulting equations are solved starting with a zero buckling, and solved iteratively with a slightly different buckling until a multiplication factor of 1 is achieved. The final buckling is the sought critical spectrum buckling used in Eq. (3.4). The final results for D_g is real because the current components J_g^+ and J_g^- are purely imaginary. This method accounts for linearly anisotropic scattering across all energy groups, and if $F(E,\Omega)$ is expanded to third order Legendre polynomials it will yield the *B-3* method which accounts for third order scattering.

3.1.2 Other Buckling Dependent Methods

There have been several other buckling dependent diffusion coefficients, and they start with the assumption that the flux can be separated as

$$\psi(\vec{r},E,\Omega) = \mathrm{Re}\left\{F(\vec{r},E,\Omega)\exp(i\boldsymbol{B}\vec{r})\right\} \tag{3.5}$$

with the source

$$S(\vec{r},E,\Omega) = \mathrm{Re}\left\{s(\vec{r},E)\exp(i\boldsymbol{B}\vec{r})\right\} \quad . \tag{3.6}$$

The term $\exp(i\boldsymbol{B}\vec{r})$ accounts for the macroscopic variation in the flux shape, and $F(\vec{r},E,\Omega)$ accounts for the periodic variation of the flux caused by the lattice cells, and has the period of a lattice cell. This method is similar to the B_n method, but modified for lattices.

3.1.2.1 Benoist

Several definitions of the diffusion coefficient can be attributed to Benoist. His method is valid only for small buckling and conserves the relation between the average flux within the cell and the leakage from the cell. It sometimes produces diffusion coefficients that are infinite in regions containing voids of certain size and shape.

3.1.2.1.1 Benoist uncorrected (Benoist Modified) (Benoist 1959)

In this definition, the diffusion coefficients in the *x* and *y* directions are given by

$$D_\nu^{BU} = \int_{cell} j_\nu \, dV \Big/ \int_{cell} \phi(\vec{r}) \, dV \quad \nu = x, y \tag{3.7}$$

with the x-direction being normal to the surface of the fuel plates and

$$j_x = -\int_{-1}^{1} \Omega_x I^x \quad , \quad j_y = -\int_{-1}^{1} \Omega_y I^y \quad , \tag{3.8}$$

with I^x and I^y being the solutions to

$$\mu \frac{\partial I^x(x,\mu)}{\partial x} + \Sigma_t(x) I^x(x,\mu) = \frac{1}{2}\Sigma_s(x) \int d\mu' \; I^x(x,\mu') - \mu R_0 \quad , \tag{3.9}$$

$$I^y = \Omega_y h^y \quad , \tag{3.10}$$

$$\mu \frac{\partial h^y(x,\mu)}{\partial x} + \Sigma_t(x) h^y(x,\mu) = -R_0 \quad , \tag{3.11}$$

$$\mu \frac{\partial R_0(x,\mu)}{\partial x} + \Sigma_t(x) R_0(x,\mu) = \frac{1}{2}\Sigma_s(x) \int d\mu' \; R_0(x,\mu') + \frac{1}{2} g(x) \; , \tag{3.12}$$

with $\mu \equiv \Omega_x$ and $g \equiv \frac{1}{2\pi} \mathrm{s}$,

which can be solved by the usual transport methods.

The uncorrected Benoist coefficient can also be written as

$$D_v^{BU} = \frac{1}{2}\bar{\Sigma}_a \bar{L}_v^2 \tag{3.13}$$

where $\bar{\Sigma}_a$ is the absorption cross section weighted with the asymptotic flux, and $\bar{L}_v^2$ is the mean-square of the crow-flight distance from birth to absorption in the ν direction.

3.1.2.1.2 Corrected Benoist (Modified Benoist) (Benoist 1964)

It replaces the diffusion coefficient in the x-direction of Eq. (3.7) with

$$D_x^{BC} = \left[\int_{cell} j_x(x)\, dV + \int_{cell} (x - x_0) \frac{\partial j_x}{\partial x}\, dV \right] \Big/ \int_{cell} \phi(x)\, dV \tag{3.14}$$

where x_0 is the center of a cell about which the cell is symmetric. This equation is called the corrected Benoist coefficient because it contains the absorption correction. The absorption correction sometimes causes the *x*-direction diffusion coefficient to have multiple values, with the number of multiple values depending on the number of definitions of a cell.

3.1.2.1.3 Classical/Collision Probabilities. (Benoist 1968)

Benoist used the collision probability method, which he also used to co develop the ABH method to calculate the thermal utilization, to derive a widely used diffusion coefficient, sometimes referred to as the classical or practical Benoist diffusion coefficient. It is, for direction ν

$$D_\nu^{BP} = \frac{1}{3} \frac{\sum_{j(cell)} \sum_{i(cell)} V_i \phi_i \lambda_J P_{ij,\nu}^*}{\sum_{j(cell)} V_j \phi_j} \tag{3.15}$$

where V_i (or V_j) is the volume of region i (or j), ϕ_i is the scalar flux in region i (or j), λ_j is the transport mean free path in region j, and $P_{ij,v}$, the so-called transport probabilities, are current averaged on the volume of medium j produced by an anisotropic source in medium i.

3.1.2.2 Deniz (1967)

Using a method that is asymptotic in space and time and preserves the asymptotic lattice period, Deniz used perturbation theory to derive directional diffusion coefficients. He started with an angularly dependent neutron balance equation with zero buckling, and introduced a non-zero buckling as an operator perturbation. The Deniz diffusion coefficient can be stated in different forms, and one of them is, in direction ν

$$D_v^D = \frac{\int d\tau \, f_0^+ \, \Omega_v E_v}{\int d\tau \, f_0^+ \, \upsilon^{-1} f_0} \tag{3.16}$$

where f_0 is the angular flux f_0^+ is the angular adjoint flux, υ is the neutron velocity, Ω_v is the ν^{th} component of neutron direction, and E_v is the solution of

$$\left(H - \frac{\alpha_0}{\upsilon} \right) E_v = \Omega_v f_0 \tag{3.17}$$

where H is the Boltzmann operator, and α_0 is the eigenvalue in the unperturbed system.

3.1.2.3 Deniz-Gelbard

In the Deniz-Gelbard (Gelbard 1974) method Gelbard adapted Deniz's approach and defined a homogenized diffusion coefficient that preserves the eigenvalue. In one group for direction ν it is

$$D_v^G = -4\pi \frac{\int d\Omega \int_L^R \Omega_v \tilde{R}(-\mu)\tilde{I}_v(\hat{\Omega})dx}{\int_L^R \nu\Sigma_f \tilde{\phi}^2 dx} \frac{\int_L^R \nu\Sigma_f \tilde{\phi} dx}{\int_L^R \tilde{\phi} dx} \tag{3.18}$$

where $\tilde{R}(-\mu)$ is defined by

$$\mu \frac{\partial \tilde{R}}{\partial x} + \Sigma_t \tilde{R} = \frac{1}{4\pi}\Sigma_s \tilde{\phi} + \frac{\nu\Sigma_f}{4\pi\lambda_0}\tilde{\phi} \quad , \tag{3.19}$$

$$\tilde{\varphi} \equiv \int \tilde{R} d\Omega \quad , \tag{3.20}$$

and the $\tilde{I}_v$ defined

$$\mu \frac{\partial \tilde{I}_x}{\partial x} + \Sigma_t \tilde{I}_x = \frac{\Sigma_s}{4\pi}\tilde{X}_x + \frac{\nu\Sigma_f}{4\pi\lambda_0}\tilde{X} - \mu\tilde{R} \quad , \tag{3.21}$$

$$\mu \frac{\partial \tilde{I}_y}{\partial x} + \Sigma_t \tilde{I}_y = -\Omega_y \tilde{R} \quad , \quad \tilde{X}_x \equiv \int d\Omega \tilde{I}_x \quad . \tag{3.22}$$

3.1.2.4 Kohler (1975)

Kohler derived directional diffusion coefficients from leakage rates based on minimizing the mean square differences between the absorption rates in the heterogeneous cell and the least square fit to the absorption rates. He defined the diffusion coefficient as

$$D_x^K = \frac{-\int_{cell} dx \int d\hat{\Omega}\, \Omega_x f^{(1,0)}(x,\hat{\Omega})}{\int_{cell} dx X^{(0,0)}(x)} \tag{3.23}$$

where the functions $f^{(m,n)}$ and $X^{(m,n)}$ are defined by the expansions

$$f(x,\hat{\Omega}) = \sum_{n,m=0}^{\infty} (i)^{m+n} B_x^n B_y^m f^{(n,m)}(x,\hat{\Omega}) \tag{3.24}$$

$$X(x) = \sum_{n,m=0}^{\infty} (i)^{m+n} B_x^n B_y^m X^{(n,m)}(x) \tag{3.25}$$

and $f(x,\hat{\Omega})$, and $X(x)$ are the lattice-periodic components of

$$F(\vec{\boldsymbol{r}},\hat{\Omega}) = f(x,\hat{\Omega})\exp(i\boldsymbol{B}\vec{\boldsymbol{r}}) \text{ and } \Phi(\vec{\boldsymbol{r}}) = X(x)\exp(i\boldsymbol{B}\vec{\boldsymbol{r}}) \quad , \tag{3.26}$$

where $F(\vec{\boldsymbol{r}},\hat{\Omega})$ is the angular flux and $\Phi(\vec{\boldsymbol{r}})$ is the scalar flux in the transport equation

$$\hat{\Omega}\nabla F(\boldsymbol{r},\hat{\Omega}) + \Sigma_t(x)F(\boldsymbol{r},\hat{\Omega}) = \frac{1}{4\pi}\Sigma_s(x)\Phi(\boldsymbol{r}) + \frac{1}{4\pi}S(\boldsymbol{r}) \quad . \tag{3.27}$$

3.1.2.5 General Transport Theory Diffusion Coefficient

A buckling dependent diffusion coefficient valid in homogeneous isotropic scattering mediums is based on transport theory in lattices where the medium was treated as an infinite lattice of point cells. Its primary definition is

$$D^H(E) = -\frac{\boldsymbol{B}\cdot\boldsymbol{j}_B(E)}{B^2\phi(E)} \tag{3.28}$$

where $\boldsymbol{B}$ is the buckling vector, $B^2 = \boldsymbol{B}\cdot\boldsymbol{B}$, and its explicit definition is

$$D^H(E) = \frac{1}{3\Sigma_t(E)}\left[1 - \frac{4}{15}\left(\frac{B}{\Sigma_t(E)}\right)^2 + \frac{44}{315}\left(\frac{B}{\Sigma_t(E)}\right)^4 + O(B^6)\right] \quad . \tag{3.29}$$

3.1.3 Other Deterministic Methods

3.1.3.1 Larsen

In a more recent deterministic definitions, Larsen (Larsen 1976) used an asymptotic theory where the mean free path is small compared to the reactor spatial domain. He derived the solution to the dimensionless transport equation

$$\frac{\partial\psi}{\partial t} + \Omega\cdot\nabla\psi + \psi - \frac{c}{4\pi}\int\psi d\Omega' = q \tag{3.30}$$

$$\text{as} \quad \psi = A(x,t)\phi(x_1,\mu) + O(\varepsilon) \tag{3.31}$$

where *A(x,t)* is the solution to the diffusion equation

$$\frac{\partial A}{\partial t} = D_1 \frac{\partial^2 A}{\partial x_1^2} + D_2 \left(\frac{\partial^2 A}{\partial x_2^2} + \frac{\partial^2 A}{\partial x_3^2} \right) - \Sigma_a A + Q \tag{3.32}$$

and $\phi(x_1,\mu)$ is lattice-periodic and is determined by a cell calculation. The diffusion coefficient in the x-direction is

$$D_x^a = \frac{\int_0^p \int_{-1}^1 \mu\phi^\dagger(x_1,\mu)(T^{-1}\mu\phi)(x_1,m)d\mu dx_1}{\int_0^p \int_{-1}^1 \phi^\dagger(x_1,\mu)\phi(x_1,\mu)d\mu dx_1} \tag{3.33}$$

and in the z-direction is

$$D_y^a = \frac{\int_0^p \int_{-1}^1 (1-\mu^2)\phi^\dagger(x_1,\mu)(H\phi)(x_1,m)d\mu dx_1}{2\int_0^p \int_{-1}^1 \phi^\dagger(x_1,\mu)\phi(x_1,\mu)d\mu dx_1} \tag{3.34}$$

where $\phi^\dagger(x_1,\mu)$ is defined as $\phi(x_1,-\mu)$ and T^{-1} is the pseudo-inverse of *T*, where the operator *T* is defined as

$$\begin{aligned} 0 &= \mu\frac{\partial}{\partial x_1}\phi(x_1,\Omega) + \phi(x_1,\Omega) - \frac{c_0(x_1)}{4\pi}\int \phi(x_1,\Omega')d\Omega' \equiv T\phi(x_1,\Omega)\ ,\ 0 < x_1 < p \\ \phi(0,\Omega) &= \phi(p,\Omega) \end{aligned} \tag{3.35}$$

and the operator *H* is defined in the solution

$$f(x_1,\Omega) \equiv (Hg)(x_1,\Omega) \tag{3.36}$$

to the problem

$$\mu\frac{\partial}{\partial x_1} f(x_1,\Omega) + f(x_1,\Omega) = g(x_1,\Omega) \tag{3.37}$$

$$f(0,\Omega) = f(p,\Omega)\ ;\ \ g(0,\Omega) = g(p,\Omega)\quad . \tag{3.38}$$

Larsen compared results of calculations using his asymptotic diffusion coefficient, Benoist corrected (Benoist 1964), and the Deniz-Gelbard (Gelbard 1974), and found their values differed depending on the level of lattice heterogeneity. Although Larsen doesn't indicate his coefficients are more accurate than the others based on the numerical results, he does imply that his might be more suited to be used in the diffusion equation because of assumptions and hypotheses used by the Benoist and Deniz-Gelbard coefficients that aren't used in his.

3.2 MONTE CARLO METHODS FOR THE DIFFUSION COEFFICIENT

3.2.1 The RCP01 Code

The RCP01 (Candelore, Gast, and Ondis 1978, Gast 1981) code evaluates the equation

$$\overline{\Sigma}_{TR}^{f} = \frac{\int_V dr \int du\ \phi(\vec{r},u)\ \Sigma_{TR}(\vec{r},u)}{\int_V dr \int du\ \phi(\vec{r},u)} \quad . \tag{3.39}$$

It does not evaluate

$$\overline{D} = \frac{\int_V dr \int du\ \phi(\vec{r},u)\ D(\vec{r},u)}{\int_V dr \int du\ \phi(\vec{r},u)} \tag{3.40}$$

because Eq. (3.40) does not yield the same result as Eq. (3.39) and may not be correct if the flux is not separable in space-energy.

To evaluate Eq. (3.39) RCP01 computes, for few group *f*,

$$\Sigma_{TR}^{f} = \frac{\sum_{C_j} \phi_{C_j} \left[\Sigma_T(u) - \Sigma_S(u)\ \mu^{\nu(C_j)} \right] + \sum_{C_j} \phi_{C_j} 10^{-20}}{\sum_{C_j} \phi_{C_j}} \tag{3.41}$$

where ϕ_{C_j} is the space-integrated flux per source neutron from collision C_j. The term sum $\sum_{C_j} \phi_{C_j} 10^{-20}$ accounts for delta, or forward, scattering.

A better approximation of the diffusion coefficient can be made by weighing the transport cross section with the current instead of the flux,

$$\overline{\Sigma}_{TR}^{f} = \frac{\int_{V} dr \int du\, J(\vec{r},u)\, \Sigma_{TR}(\vec{r},u)}{\int_{V} dr \int du\, J(\vec{r},u)} \quad , \tag{3.42}$$

but the calculation of the current is subject to inaccuracies that the flux is not, so RCP01 computes Eq. (3.41) for few-group *f*, uses it to calculate the diffusion coefficient for few-group *f* as $D_f = 1/(3\Sigma_{tr}^{f})$, and then multiplies it by a few-group independent correction factor *k*, making the diffusion coefficient for few group *f* equal to

$$D_{TC}^{f} = \frac{k}{3\,\Sigma_{TR}^{f}} \quad . \tag{3.43}$$

The correction factor *k* which is used only for the fast groups, preserves the neutron age to thermal, and is calculated in an infinite reactor. RCP01 doesn't calculate a scattering matrix. The few group diffusion coefficients and cross sections calculated by RCP01 agree reasonably well in most cases with deterministic calculations.

3.2.2 Ilas and Rahnema

Ilas and Rahnema (Ilas and Rahnema 2003) used Monte Carlo methods for loosely coupled spent fuel storage racks using two different methods. In the Monte Carlo normalized diffusion method, the node homogenized diffusion coefficient in the thermal

group was defined as simply D_{th}= 1/(3$\Sigma_{t,th}$), where $\Sigma_{t,th}$ is the cell homogenized total cross section in the thermal group. For the fast group the diffusion coefficient was defined as

$$D_f = \frac{\sum_{k=1}^{2}\left(D_f^k \int_k \phi_f \, d^3r \right)}{\int_{cell} \phi_f \, d^3r} \quad , \tag{3.44}$$

where D_f^k is the fast diffusion coefficient in region k, where k=1 for the homogenized fuel and water region and 2 for the water region. In the fuel and water region D_f^1 is defined as $1/(3\Sigma_t^1)$ and in the water region it is determined using the following iterative process. Two-group total cross sections are calculated using MCNP (BRIESMEISTER 1997) with continuous energy, and are used to calculate a fast diffusion coefficient as $D_f^2 = 1/(3\Sigma_t)$. The fast group water region diffusion coefficient is input into a fine mesh calculation and varied until multiplication factor results from it agree with MCNP continuous energy, and this final diffusion coefficient is used as the fast group water region diffusion coefficient, D_f^2, in Eq. (3.44).

Ilas and Rahnema also used Monte Carlo methods to evaluate the diffusion coefficient based on its conventional definition. In this method, the diffusion coefficient is determined from a continuous energy Monte Carlo simulation of the lattice cell using MCNP. This approach is similar to that used by Gast (1981) in the code RCP01, but no correction of the fast diffusion coefficient is made. The nodal diffusion coefficient for group g is defined as $1/\left(3\overline{\Sigma}_{tr,g}\right)$, where the node-averaged transport cross section in group g, $\overline{\Sigma}_{tr,g}$, is given by:

$$\overline{\Sigma}_{tr,g} = \frac{\int_g dE \int_{\vec{r}} d\vec{r} \Sigma_{tr}(\vec{r},E)\Phi(\vec{r},E)}{\int_g dE \int_{\vec{r}} d\vec{r} \Phi(\vec{r},E)} \tag{3.45}$$

where $\vec{r}$ represents the spatial variable, E the neutron energy, $\Phi(\vec{r},E)$ the scalar flux, and $\Sigma_{tr}(\vec{r},E)$ is given by:

$$\Sigma_{tr}(\vec{r},E) = \Sigma_t(\vec{r},E) - \mu(E)\Sigma_s(\vec{r},E) \quad . \tag{3.46}$$

In Eq. (3.46) $\mu(E)$ is the average cosine of the scattering angle in the laboratory system, $\Sigma_t(\vec{r},E)$ and $\Sigma_s(\vec{r},E)$ are the total and the scattering cross sections, respectively. The value of $\mu(E)$ for a collision is calculated as a scalar product of the incident and emergent unit direction vectors.

The numerator in Eq. (3.45) is estimated by tallying the following in MCNP:

$$\left\{\Sigma_t(\vec{r},E) - \left[\Sigma_t(\vec{r},E) - \Sigma_c(\vec{r},E) - \Sigma_f(\vec{r},E)\right](uu' + vv' + ww')\right\}\Phi(\vec{r},E) \ , \tag{3.47}$$

where $\Sigma_c(\vec{r},E)$ is the capture cross section, $\Sigma_f(\vec{r},E)$ the fission cross section, (u,v,w) the incident direction cosines, and (u',v',w') the emergent direction cosines. A patch file is added to MCNP to define the fission cross section and to define user bins through the TALLYX subroutine to tally the quantity in Eq. (3.47). The denominator in Eq. (3.45) is obtained from a standard MCNP F4 (flux) tally. This method and the Monte Carlo normalized diffusion method described previously yield results of varying accuracy, depending on the level of heterogeneity.

3.2.3 Pounders

Pounders examined some methods for stochastically estimating diffusion coefficients. He tallied first order Legendre moments and applied them to what he refers to as the classical,

$$\sigma_{tr,g}^{C}(r) = \sigma_{g}(r) - \sum_{g'=1}^{G} \sigma_{s,1}^{gg'}(r) \quad , \tag{3.48}$$

and exact

$$\sigma_{tr,g}^{P1}(r) = \sigma_{g}(r) - \frac{\sum_{g'}^{G} \sigma_{s,1}^{g'g} J_{g'}(r)}{J_{g}(r)} \tag{3.49}$$

definitions of the diffusion coefficient. He also stochastically calculated a higher order diffusion coefficient,

$$D_{g}^{S} = -\frac{\bar{J}_{g} V_{T}}{\left(\bar{\phi}_{g}^{+} - \bar{\phi}_{g}^{-}\right) A_{T}} \quad , \tag{3.50}$$

and a cross section partially based on FDT,

$$\sigma_{tr,g}^{FL}(r) = \sigma_{g}(r) - \sum_{g'=1}^{G} \frac{\sigma_{s,1}^{g'g}(r)\phi_{g'}(r)}{\phi_{g}(r)} \tag{3.51}$$

which is also evaluated in more detail and with more applications in this work.

3.2.4 Milgram

Milgram (Milgram 1997) modified the MCNP code to calculate few group diffusion coefficients in the axial direction for a CANDU reactor using the definition $J_{g} = -D_{g}\nabla\phi_{g}$. He calculated the current using an ordinary current tally, and used one of three methods to determine the gradient of the flux in the axial direction of the channel.

The first one used current tallies along the length of the channel to calculate a value of B_z from the relationship $\phi = \phi_0 \cos[B_z z]$. The gradient was then calculated from $\nabla\phi = -\phi_0 B_z \sin[B_z z]$. The second method fitted cubic splines to the flux shape to get its slope, while the third used a least squares polynomial fit.

3.2.5 Other Monte Carlo Estimates of the Diffusion Coefficient

Gelbard and Lell (Gelbard and Lell 1977) used Monte Carlo techniques to calculate one-speed diffusion coefficients in an infinite and uniform but complicated lattice. It is defined as one-half the product of the cell averaged absorption cross section, weighted with the zero-buckling scalar flux, and the mean square distances from birth to fission. Gelbard and others (Gelbard et al. 1977) used Monte Carlo to calculate the modified Benoist coefficients for voided regions in a gas-cooled reactor.

4 RESULTS AND ANALYSIS

Because a very large number of graphs was used to analyze the results, the only graphs shown in this section are examples and ones that are directly referred to in the text.

All of the graphs plot a particular output as a function of fine-mesh location. There are energy-integrated plots, a 4-group case being labeled as "4 groups", and individual energy group plots, labeled as "group 1 of 4", for example. The individual energy group results have the advantage of being insusceptible to error cancellation across energy, and also allow analysis in individual groups, while the energy integrated results have neither of these features.

For the single-assembly cases, with vacuum and reflective boundary conditions, 47- and 4-group energy-integrated results, and 4- and 2-individual-group results are included. For the whole-core cases 2-individual-group results are shown.

The first type of graph plots the spatial shape of the normalized fluxes obtained from the transport benchmark calculation and the fine-mesh mesh diffusion calculation using each of the three diffusion coefficients tested throughout the entire problem space, which would be an entire half-assembly or an entire half-core. Figure 4.1 shows an example for the case of assembly type 1 with vacuum boundary conditions, group 1 of the 4-group calculation. The normalized flux for mesh point n is defined as $\tilde{\phi}_n = N \cdot \phi_n \Big/ \sum_N \phi_n$, where N is the number of mesh points. This type of plot provides a graphic presentation of the fluxes throughout the entire problem in one view. The

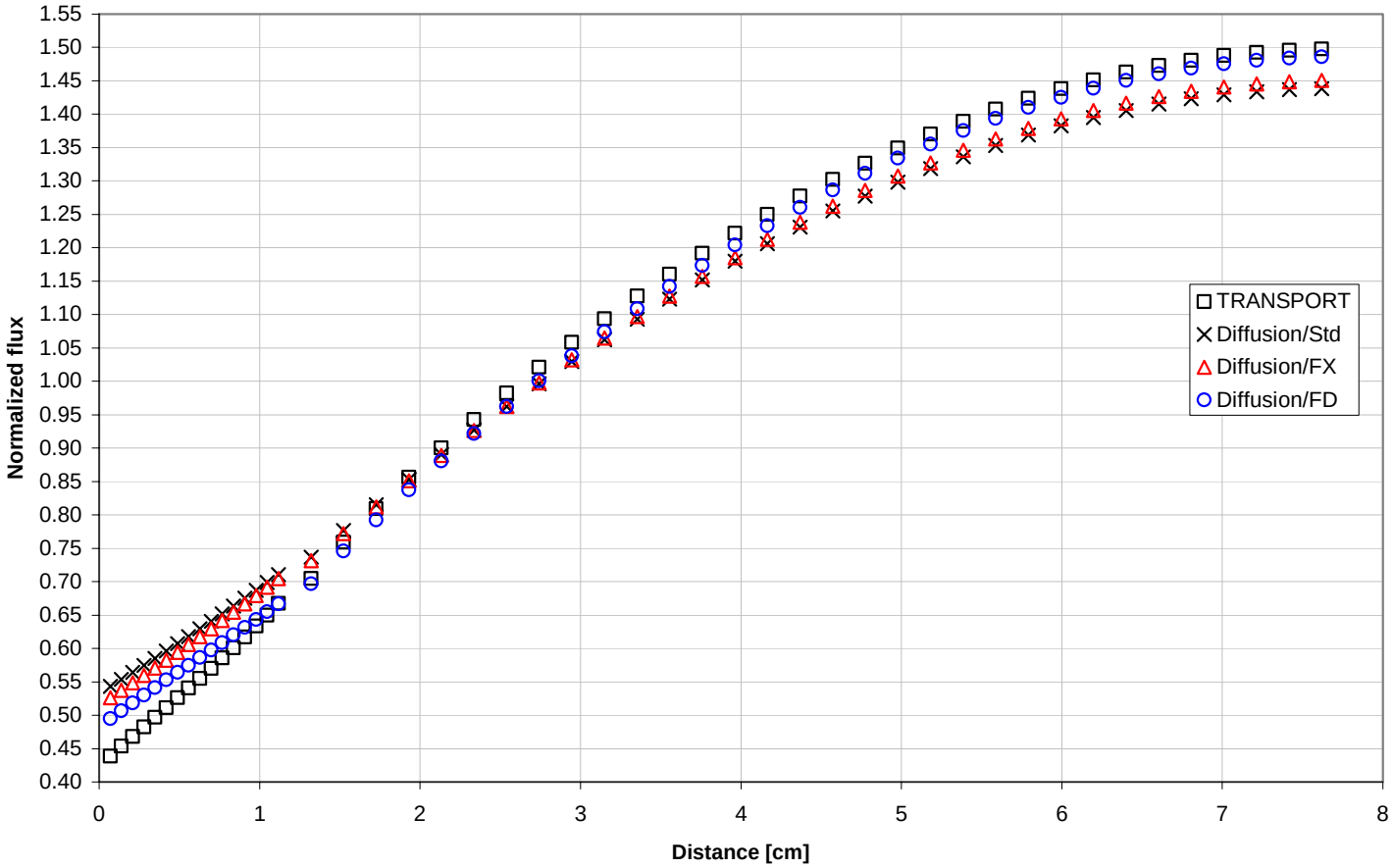

Figure 4.1: Normalized flux, Heterogeneous half-assembly 1, Vacuum BCs, group 1 of 4, Transport and Diffusion Thy. w/Std, FX, FD.

normalized flux-error spatial profiles are also plotted, with the error at mesh-point *n* defined as

$$e_n = 100\left(\phi_n^{\text{diffusion}} - \phi_n^{\text{transport}}\right)\Big/\phi_n^{\text{transport}} \quad , \tag{4.1}$$

and with the assembly 1 group 1 example in Figure 4.2. The final type of graph is the current/flux $\left(\mathbf{J}/\phi\right)$ ratio. The current here is the neutron current calculated with Fick's Law,

$$\left|\mathbf{J}\right| = -\mathrm{D}\frac{d\phi}{dx} \quad , \tag{4.2}$$

where the diffusion coefficient is either one of the three diffusion coefficients tested. This current is then divided by the scalar flux output from the transport calculation. The derivative of the flux used in Eq. (4.2) is also based on the transport calculation. Because the magnitude of the current calculated with the Fick's Law approximation can exceed the scalar flux under certain conditions, yielding a non-physical result, a current/flux ratio greater than 1 is also non-physical, and the behavior of each current/flux ratio had to be analyzed throughout the problem. These analyses were performed only for output from individual energy groups, and the results for assembly 1 group 1 are shown in Figure 4.3.

As an aid to analyze the errors in the fluxes per mesh interval, three collective error measures were used, the AVG (average), RMS (root mean square), and MRE (mean relative error) error measures. With e_n being the per cent error in the normalized flux at mesh point *n*, as defined in Eq. (4.1),

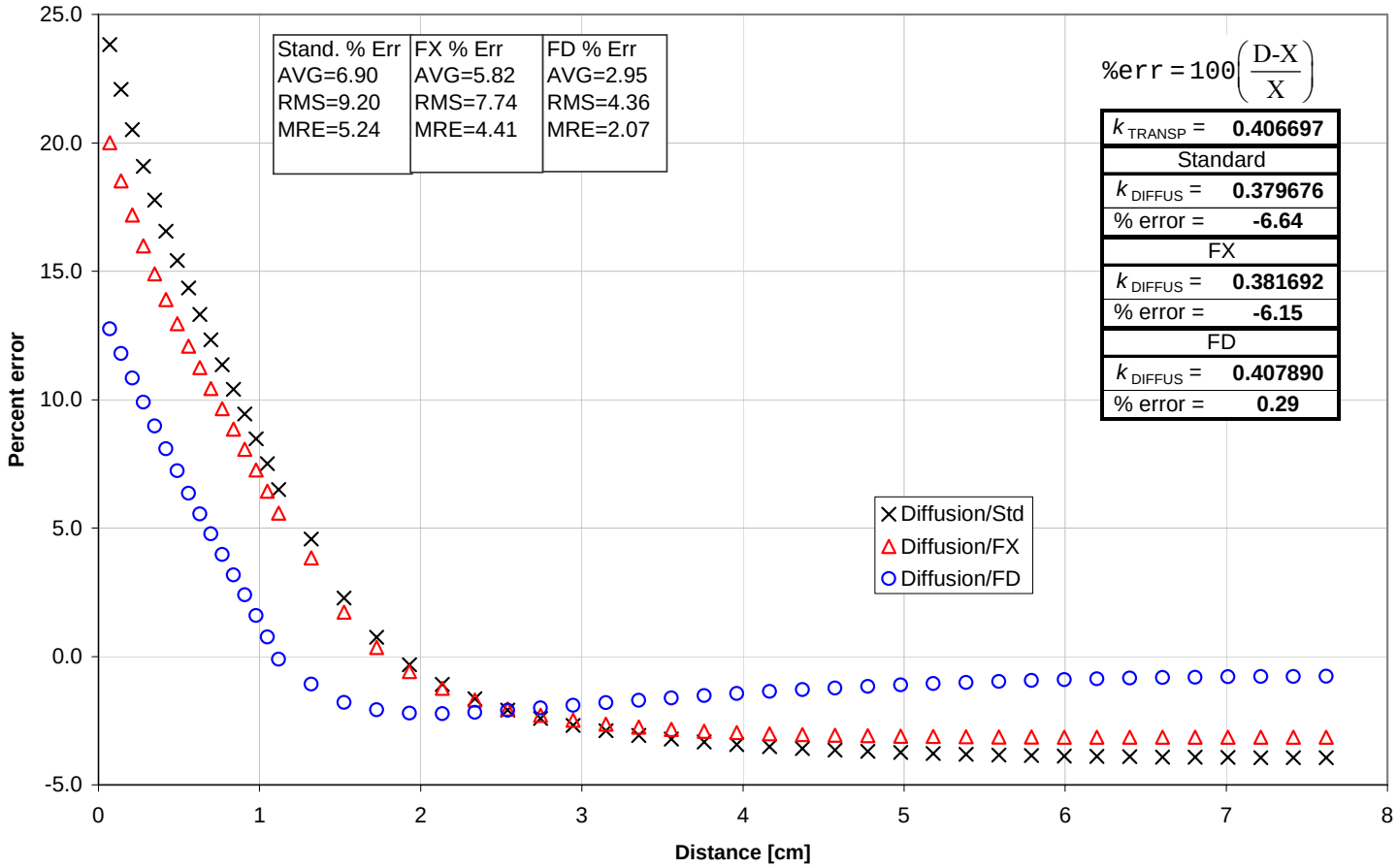

Figure 4.2: Normalized flux percent error, Heterogeneous half-assembly 1, Vacuum BCs, group 1 of 4, Diffusion Thy. w/Std, FX, FD.

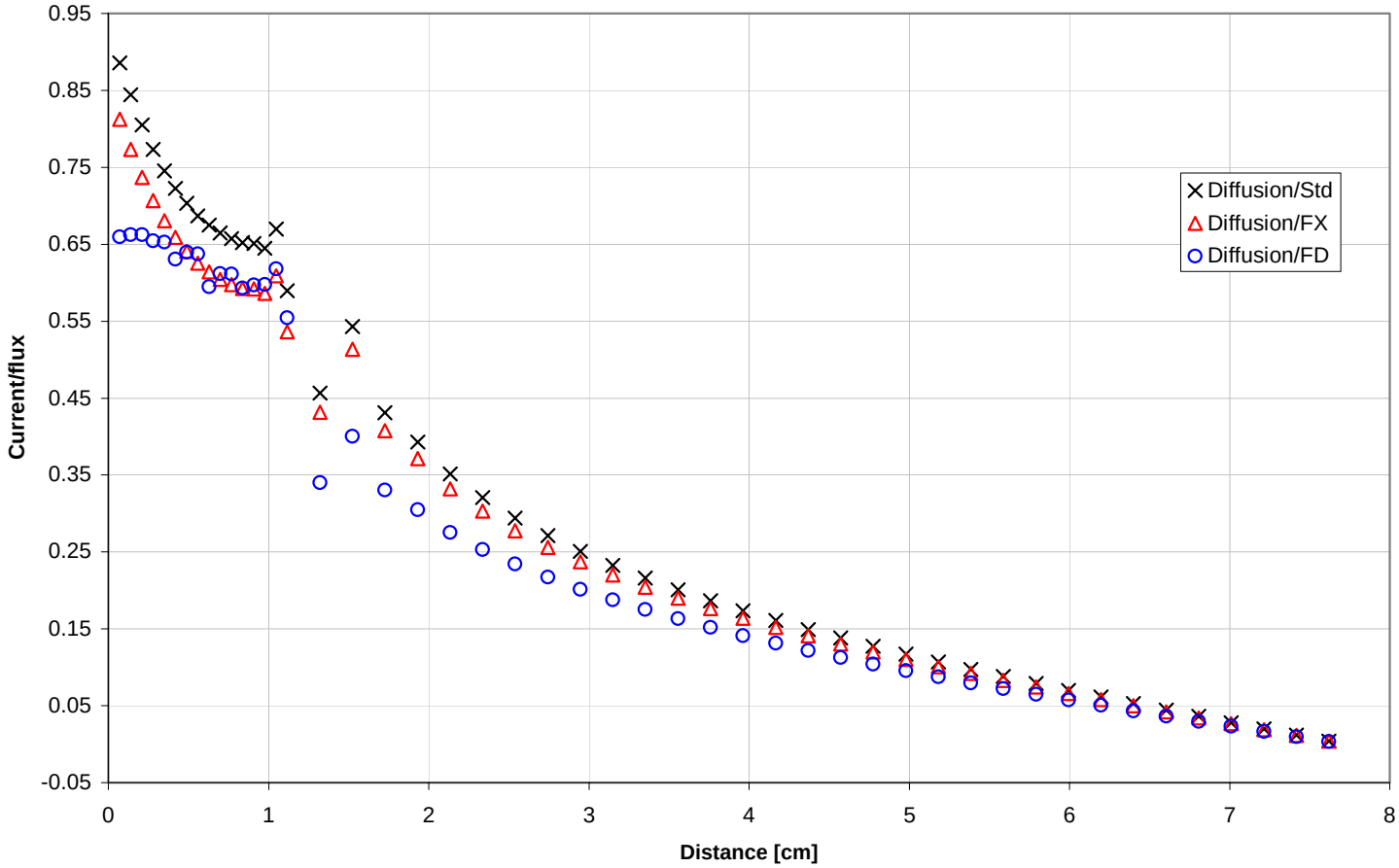

Figure 4.3: Current to flux ratio, Heterogeneous half-assembly 1, Vacuum BCs, group 1 of 4, Diffusion Thy. w/Std, FX, FD.

$$\text{AVG} = \frac{\sum_{N} |e_n|}{N} \quad , \tag{4.3}$$

$$\text{RMS} = \sqrt{\frac{\sum_{N} e_n^2}{N}} \quad , \tag{4.4}$$

and

$$\text{MRE} = \frac{\sum_{N} |e_n| \cdot \phi_{n,Transport}}{N \cdot \phi_{Transport}^{avg}} \quad . \tag{4.5}$$

The MRE error is sometimes referred to as the flux-weighted error, and its value approaches that of AVG when the normalized fluxes are spatially flat, because in that case each ϕ_n would be close to 1.

Because the results and conclusions based on comparisons using the RMS and MRE measures are consistent with those based on the AVG, only the AVG measures are shown in the tables of results to save space. However, the results that have plots of flux-error profiles also have all three error measures embedded in the graph plot area, as in Figure 4.2.

4.1 SINGLE-ASSEMBLIES

4.1.1 47, 4, and 2 Groups with Vacuum Boundary Conditions

Because individual energy-group results for 47 groups would make the results even more voluminous than it already is, these results are not shown. However, as will be seen below, because the errors in the individual 4-group results are consistent with

their energy-integrated counterpart, error cancellation is largely absent in 4 groups, and is likely absent in 47 groups as well, and 47 integrated group results provide an accurate indication of the methods' errors. One can also confirm the absence of error cancellation in 4 groups by noting that for a constant mesh location, the flux-errors usually do not change signs across energy groups. In the 2-group results, however, there was significant error cancellation in the energy-integrated results, and therefore only individual group results will be shown for 2-group calculations. The eigenvalue errors, however, are the same in energy-integrated groups as in individual energy groups because they're always calculated as energy-integrated neutron production to loss ratios.

The plots in Figure 4.4 and Figure 4.5 show the normalized flux spatial profiles for 47 and 4 energy-integrated groups, respectively, while Figure 4.6 and Figure 4.7 show the energy-integrated flux-errors in these energy structures, for the case of assembly type 1. For both of these energy structures the error profiles show that all of the diffusion theories perform much worse approaching the boundary of the assembly, where the vacuum boundary condition causes diffusion theory to break down because of transport effects. This effect is typical in all of the energy structures and assemblies using vacuum boundary conditions.

The results in the previous four figures, and for the remaining assembly types, are summarized in Table 4.1 through Table 4.4, which contain eigenvalues from the transport and diffusion calculation in one type of table and the AVG and eigenvalue errors for all assemblies in 47 and 4 integrated groups. In the tables such as Table 4.2, the column underneath "Egy Grp" indicates for which energy group the AVG error is shown in the table, which in this case is "All", indicating integration over all groups. The row to the

right of "error$_k$" contains eigenvalue per cent errors, defined as

$error_k = 100 \times \left(k_{Diff} - k_{Transp} \right) \Big/ k_{Transp}$. The shaded values denote the lowest errors. These graphs and the tables indicate that the FD reduces flux errors by about half, and eigenvalue errors even more significantly, by between 70% and two orders of magnitude.

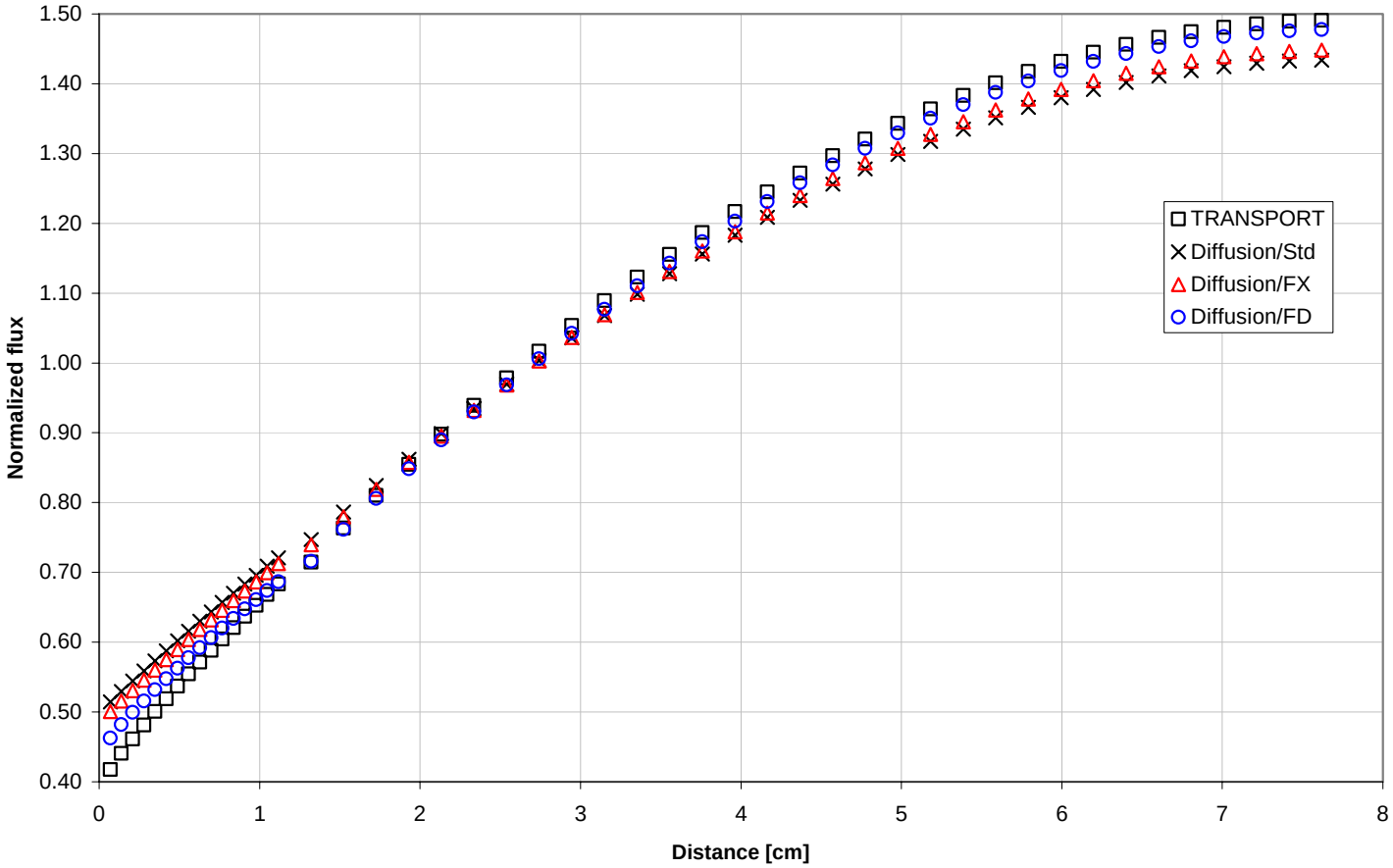

Figure 4.4: Normalized flux, Heterogeneous half-assembly 1, Vacuum BCs, 47 groups, Transport and Diffusion Thy. w/Std, FX, FD.

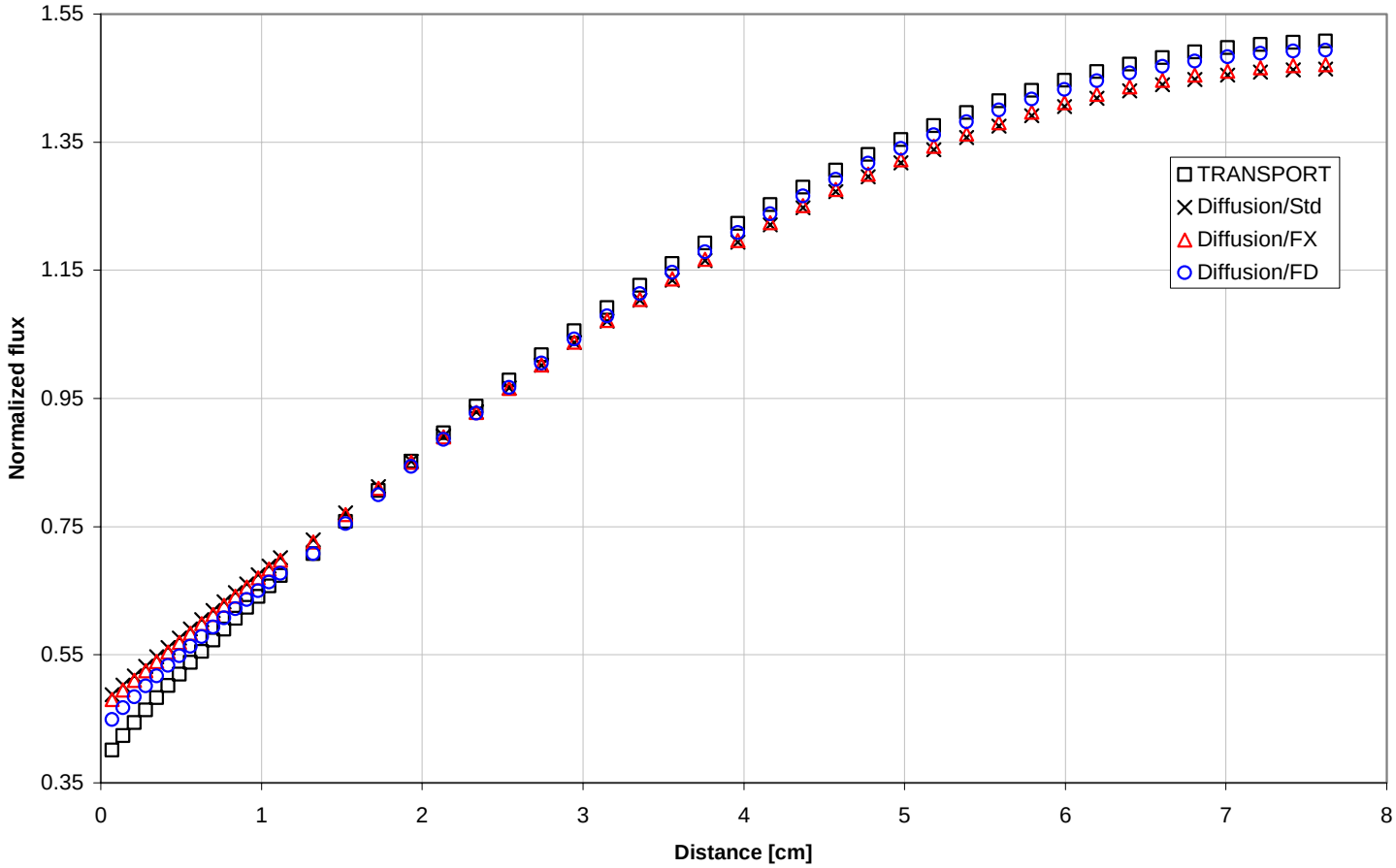

Figure 4.5: Normalized flux, Heterogeneous half-assembly 1, Vacuum BCs, 4 groups, Transport and Diffusion Thy. w/Std, FX, FD.

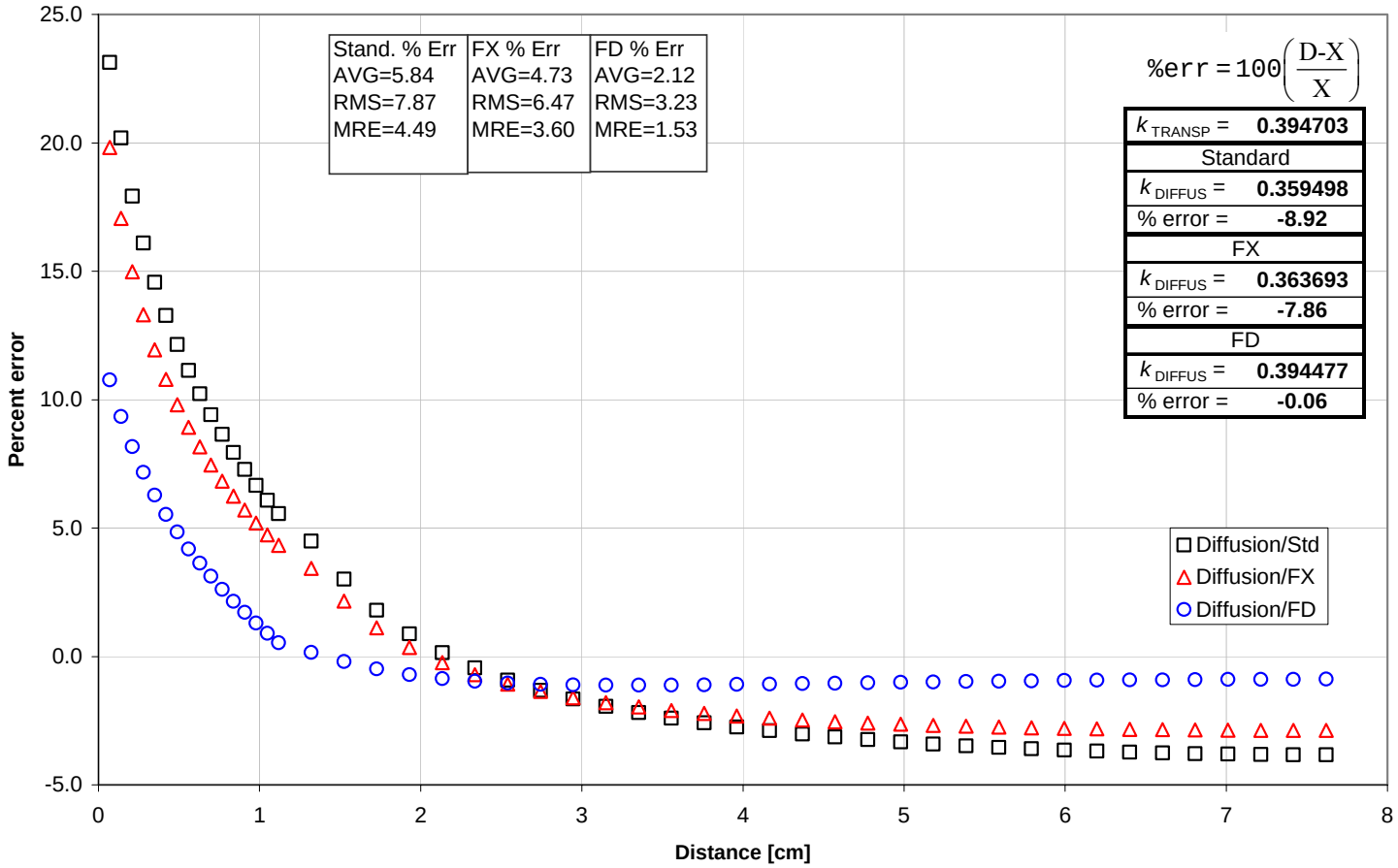

Figure 4.6: Normalized flux percent error, Heterogeneous half-assembly 1, Vacuum BCs, 47 groups, Diffusion Thy. w/Std, FX, FD.

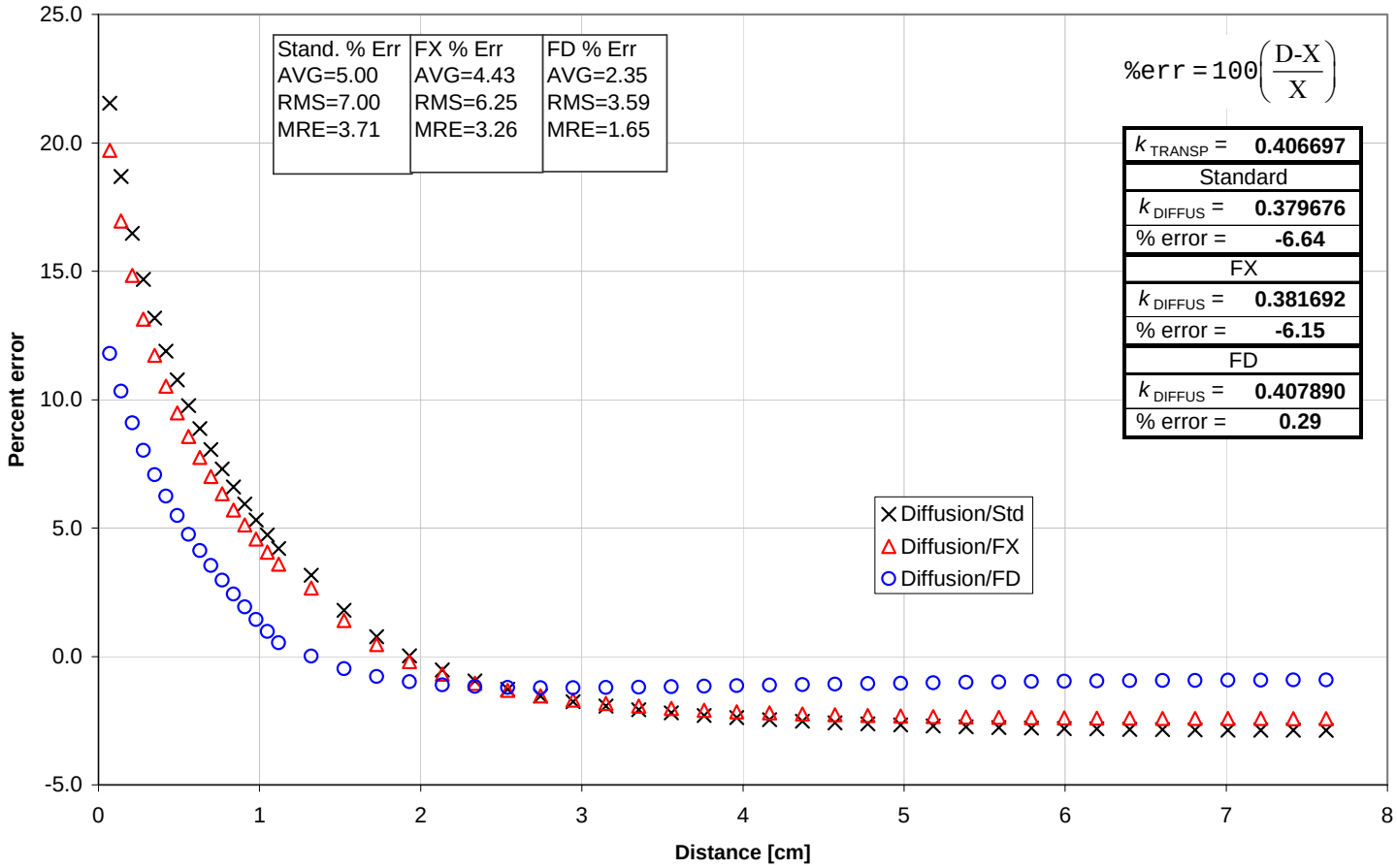

Figure 4.7: Normalized flux percent error, Heterogeneous half-assembly 1, Vacuum BCs, 4 groups, Diffusion Thy. w/Std, FX, FD.

Table 4.1: Eigenvalues, Forty-seven groups, Heterogeneous half-assemblies, Vacuum BCs, Diffusion Thy. w/Std, FX, FD.

Assy 1				Assy 2			
Transport	Std	FX	FD	Transport	Std	FX	FD
0.394703	0.359498	0.363693	0.394477	0.432455	0.393417	0.398723	0.429497
Assy 3				Assy 4			
Transport	Std	FX	FD	Transport	Std	FX	FD
0.194984	0.179625	0.182263	0.197830	0.163047	0.150736	0.154258	0.164708

Table 4.2: Errors, Forty-seven Energy Integrated groups, Heterogeneous half-assemblies, Vacuum BCs, Diffusion Thy. w/Std, FX, FD.

	Assy 1			Assy 2		
Egy Grp	Std	FX	FD	Std	FX	FD
All	5.84	4.73	2.12	6.49	5.20	2.78
$error_k$	-8.92	-7.86	-0.06	-9.03	-7.80	-0.68
	Assy 3			Assy 4		
Egy Grp	Std	FX	FD	Std	FX	FD
All	4.71	3.62	2.20	6.31	4.96	1.89
$error_k$	-7.88	-6.52	1.46	-7.55	-5.39	1.02

Table 4.3: Eigenvalues, Four groups, Heterogeneous half-assemblies, Vacuum BCs, Diffusion Thy. w/Std, FX, FD.

Assy 1				Assy 2			
Transport	Std	FX	FD	Transport	Std	FX	FD
0.406697	0.379676	0.381692	0.407890	0.445855	0.416123	0.418813	0.444870
Assy 3				Assy 4			
Transport	Std	FX	FD	Transport	Std	FX	FD
0.196958	0.183907	0.185068	0.199071	0.166116	0.157561	0.159401	0.168409

Table 4.4: Errors, Four Energy Integrated groups, Heterogeneous half-assemblies, Vacuum BCs, Diffusion Thy. w/Std, FX, FD.

	Assy 1			Assy 2		
Egy Grp	Std	FX	FD	Std	FX	FD
All	5.00	4.43	2.35	5.43	4.74	2.84
$error_k$	-6.64	-6.15	0.29	-6.67	-6.07	-0.22
	Assy 3			Assy 4		
Egy Grp	Std	FX	FD	Std	FX	FD
All	4.21	3.17	2.46	5.46	4.75	2.26
$error_k$	-6.63	-6.04	1.07	-5.15	-4.04	1.38

A more in-depth analysis is possible for the 4- and 2-group calculations because the results are broken down into individual groups and current/flux ratios were also calculated to help analyze the results. Starting with the 4 individual-group calculations, the AVG error measures in Table 4.5 indicate that the flux-errors using FD were significantly reduced in all groups and assemblies except in group 3, which showed increased errors compared to the Std method in all but assembly type 3, and in group 4 of assembly type 2, which showed about the same level of errors as the other two methods.

In spatial profiles of the 4-group current/flux ratios the FD method produces the smallest current/flux ratio approaching the boundaries of the assemblies, with the other two methods approaching 1 and with the FX even exceeding 1, as in Figure 4.8, Figure 4.9, Figure 4.10, and Figure 4.11, for group 3 in every assembly at the first mesh point in the water region, indicating that it is not flux-limited. It is in these boundary mesh points that the flux gradient, hence the current, and hence the current/flux ratio, is the largest, and where the FD is expected to yield the greatest improvement over the other diffusion

Table 4.5: Errors, Four Individual groups, Heterogeneous half-assemblies, Vacuum BCs, Diffusion Thy. w/Std, FX, FD.

	Assy 1			Assy 2		
Egy Grp	Std	FX	FD	Std	FX	FD
1	6.90	5.82	2.95	7.34	6.15	3.45
2	2.95	3.05	1.75	3.49	3.52	2.30
3	1.43	2.26	2.00	1.64	2.52	2.26
4	1.34	1.23	1.17	1.34	1.30	1.33
$error_k$	-6.64	-6.15	0.29	-6.67	-6.07	-0.22
	Assy 3			Assy 4		
Egy Grp	Std	FX	FD	Std	FX	FD
1	5.73	4.72	2.98	6.98	5.89	2.86
2	1.92	2.20	1.16	2.86	3.00	1.67
3	1.71	2.19	0.98	1.42	2.02	1.64
4	3.50	4.31	3.06	6.68	6.82	4.93
$error_k$	-6.63	-6.04	1.07	-5.15	-4.04	1.38

coefficients, which it does. But the FD also reduces flux-errors in some groups and assemblies in mesh points far from the assembly boundary, in the water and fuel region, and towards the assembly center. This occurs even though the current/flux ratios in the corresponding regions are low. For examples of this we refer to group 1 of assembly type 1 and group 2 of assembly type 2. The normalized fluxes, flux-errors and current/flux ratios, respectively, are shown in Figure 4.1 on page 39, Figure 4.2 on page 41, and Figure 4.3 on page 42 for group 1 assembly 1, and in Figure 4.12, Figure 4.13, and Figure 4.14 below for group 2 assembly 2. In some of these small-gradient regions, not only is the current/flux ratio small, but the difference between the FD and Std ratios is also very small. Error-reductions in these regions using the FD do not occur in all assemblies and groups, but occur in all four assembly types for groups 1 and 2 as in the previous examples, and because the current/flux ratios in these regions are about the same for all of the diffusion coefficients, there might be something other than the flux-limiting

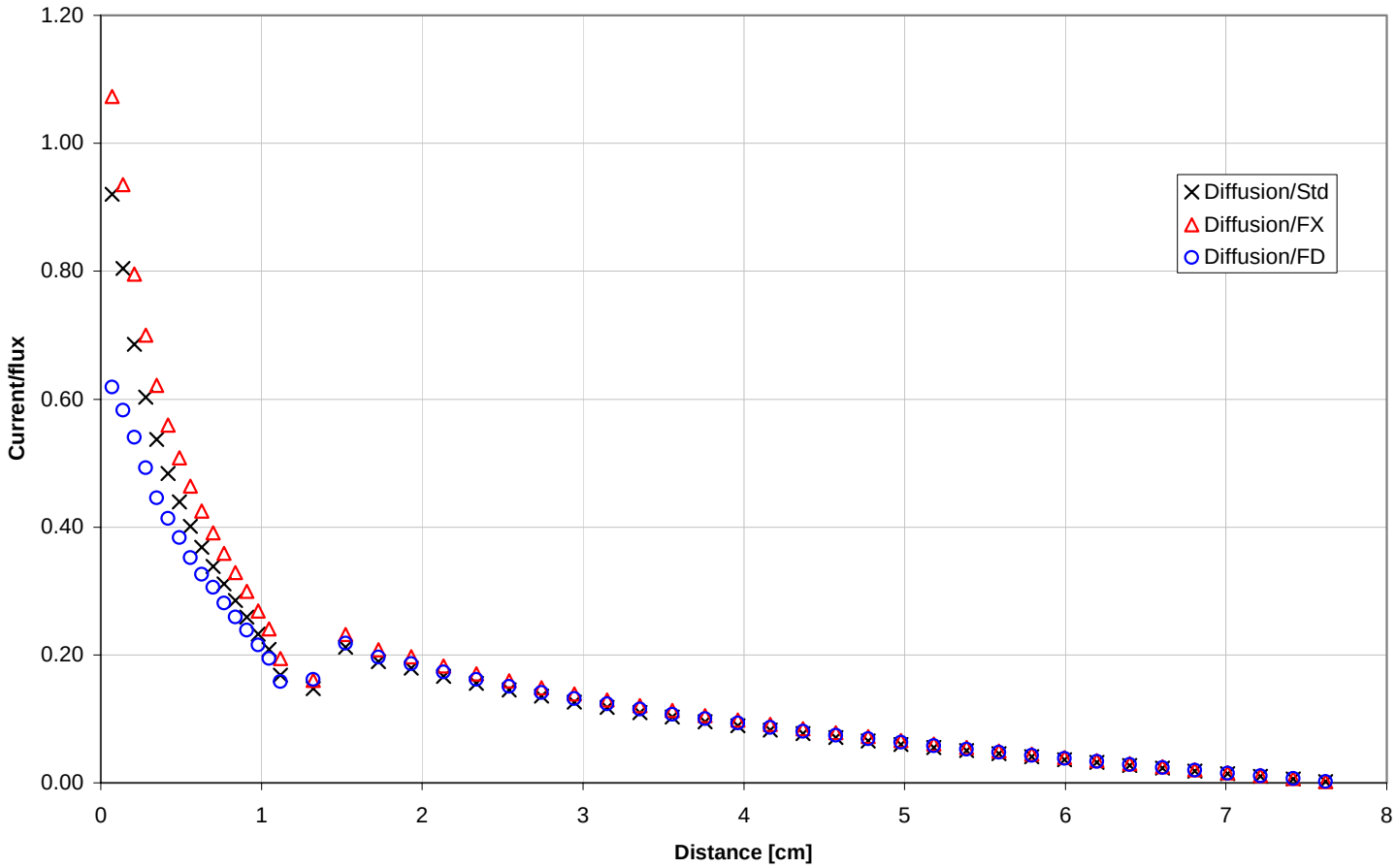

Figure 4.8: Current to flux ratio, Heterogeneous half-assembly 1, Vacuum BCs, group 3 of 4, Diffusion Thy. w/Std, FX, FD.

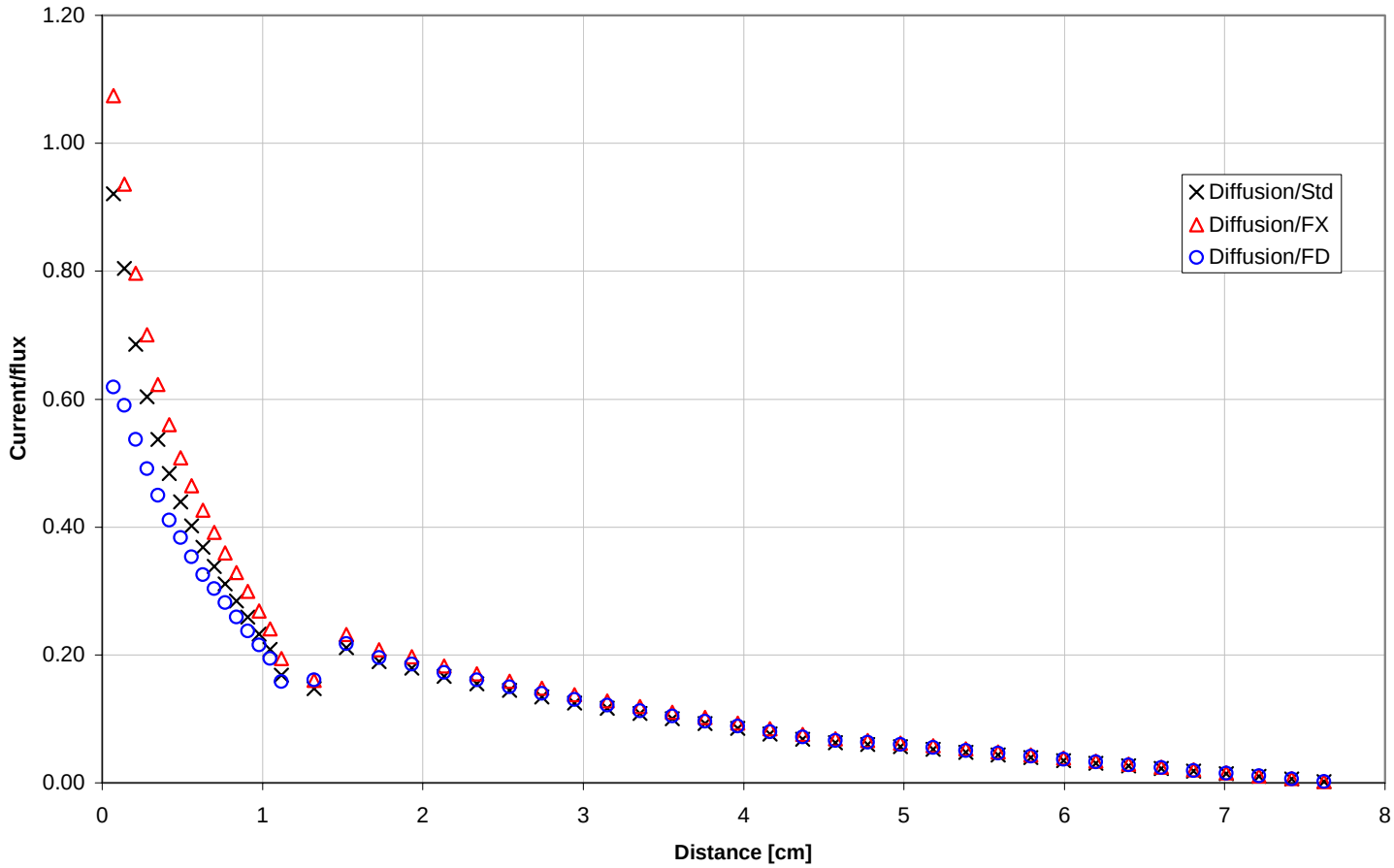

Figure 4.9: Current to flux ratio, Heterogeneous half-assembly 2, Vacuum BCs, group 3 of 4, Diffusion Thy. w/Std, FX, FD.

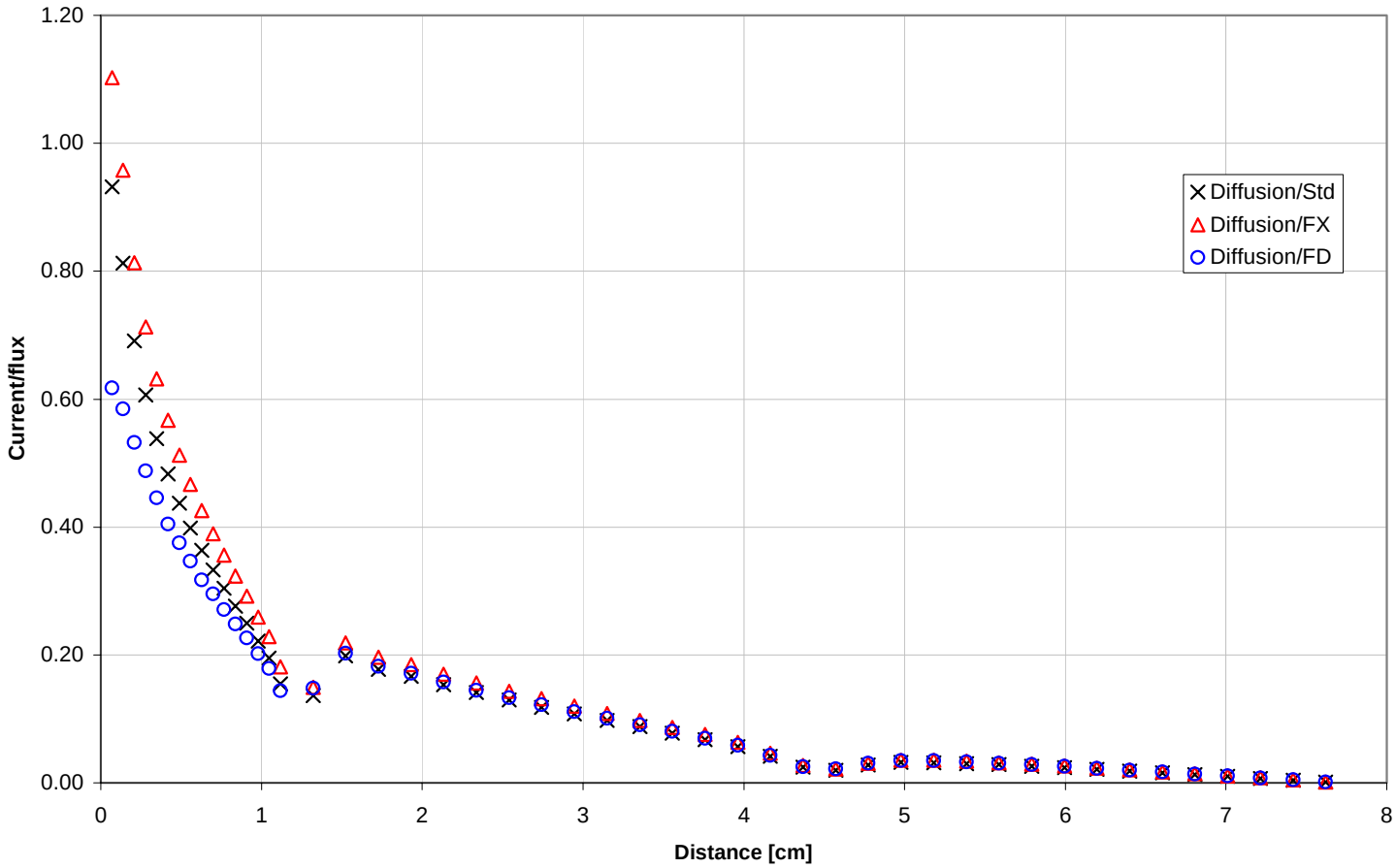

Figure 4.10: Current to flux ratio, Heterogeneous half-assembly 3, Vacuum BCs, group 3 of 4, Diffusion Thy. w/Std, FX, FD.

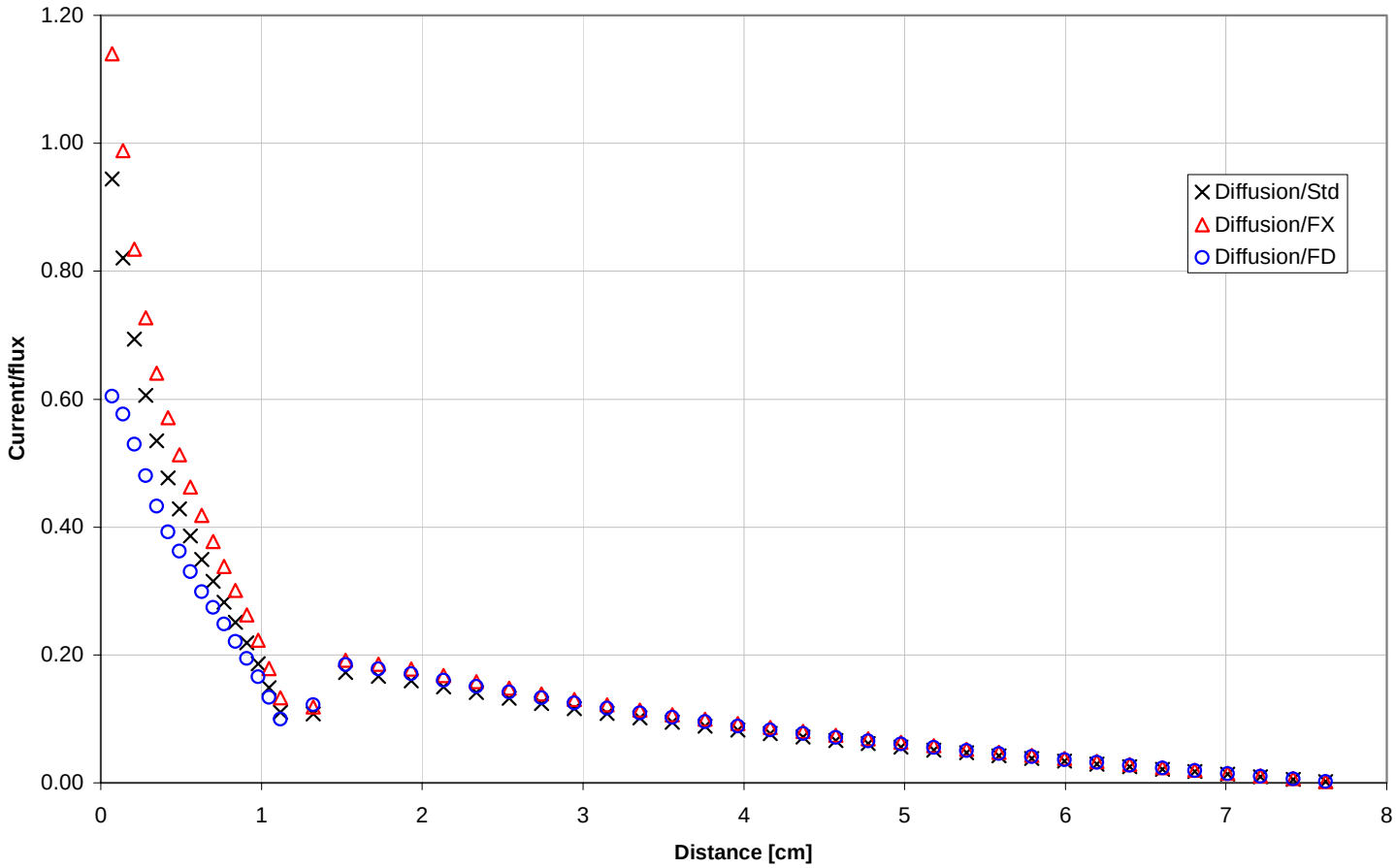

Figure 4.11: Current to flux ratio, Heterogeneous half-assembly 4, Vacuum BCs, group 3 of 4, Diffusion Thy. w/Std, FX, FD.

characteristic of the FD that reduces errors.

One might also notice that the current/flux ratios for the group 1 calculations in every assembly type oscillate at the first few mesh points, as in Figure 4.3 and Figure 4.15 through Figure 4.17, located between zero and approximately 1 cm. These oscillations are caused by convergence issues during the transport calculations and only affect the current/flux ratios in group 1 out of all of the energy structures, near vacuum boundary conditions. Apparently they affect the current/flux ratios but do not significantly affect the flux calculated using the FD as will be shown in section 4.3, which discusses the accuracy of the calculation of the derivative.

From the 2-group calculations, the eigenvalue results in Table 4.6 and errors results in Table 4.7 below show that FD reduces errors significantly in group 1, either slightly reduces or worsens errors in group 2, and significantly reduces eigenvalue errors. Overall, the single most accurate method is the FD.

In the 2-group calculations the group 1 current/flux ratios do not oscillate at the boundary of the assembly, for example in Figure 4.18, as the group 1 calculations do in the 4-group calculations, resulting from better convergence of the transport calculation.

Also, although the FX method yields the largest current/flux ratio near the boundaries of the problems, it never exceeds 1 as it did for all assembly types in group 3 of the 4-group calculations.

An interesting observation is that for all group 1 calculations of the current/flux ratio, in the 2- and 4-group energy structures, at the first few data points in the water, there is an almost horizontally asymptotic approach to a value less than 1 approaching the assembly boundary, while the Std and FX methods approach 1 at a faster rate, as

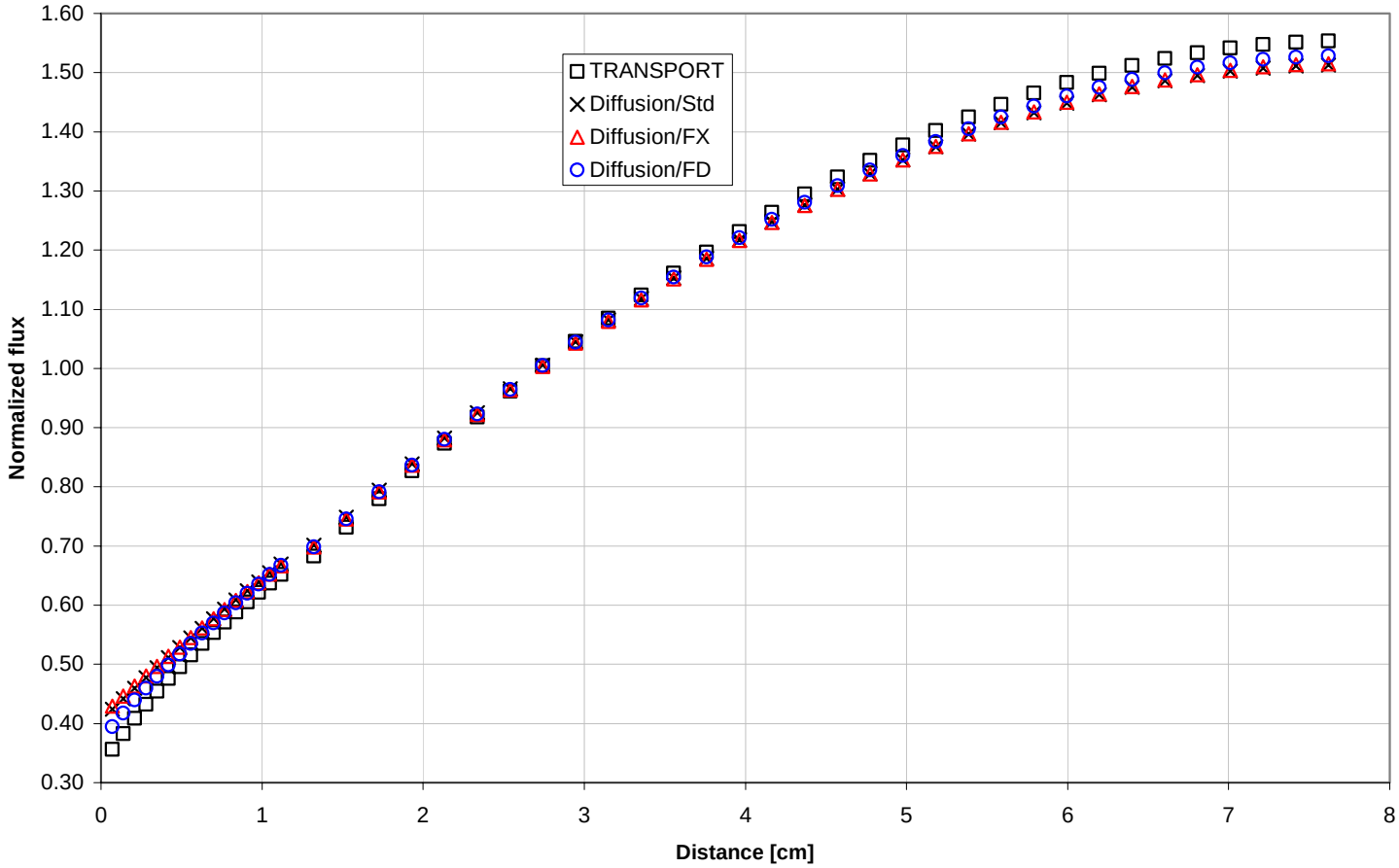

Figure 4.12: Normalized flux, Heterogeneous half-assembly 2, Vacuum BCs, group 2 of 4, Transport and Diffusion Thy. w/Std, FX, FD.

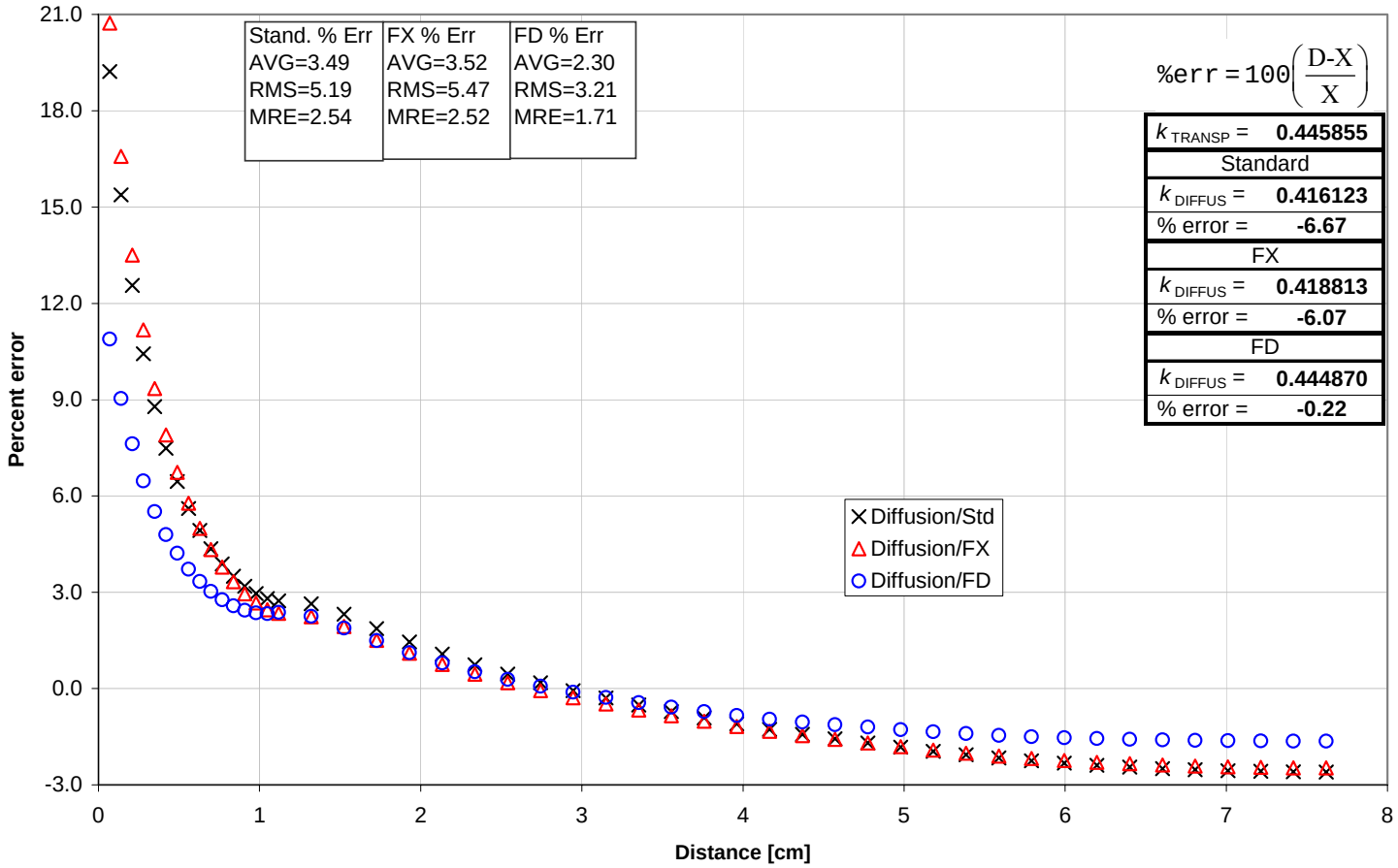

Figure 4.13: Normalized flux percent error, Heterogeneous half-assembly 2, Vacuum BCs, group 2 of 4, Diffusion Thy. w/Std, FX, FD.

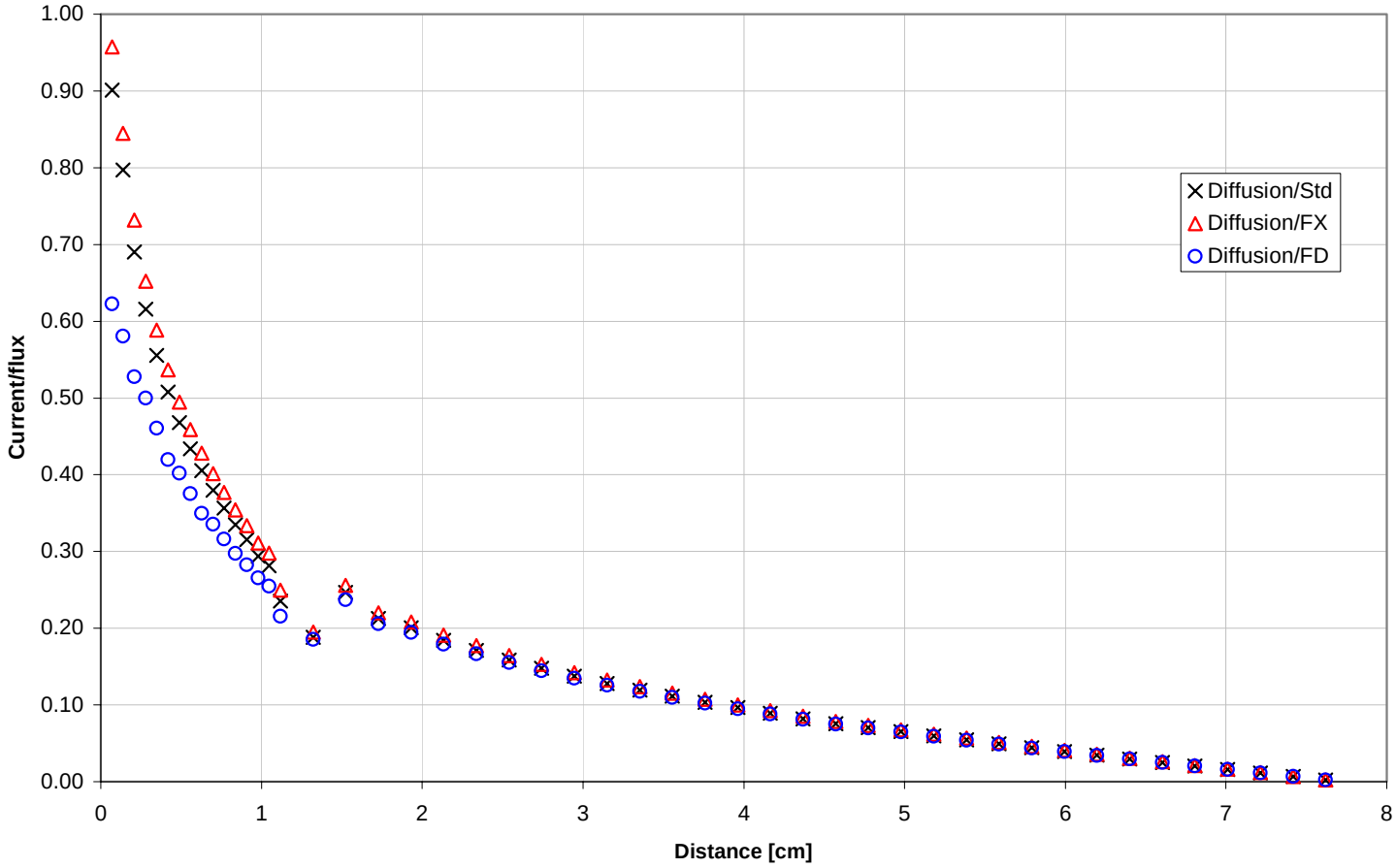

Figure 4.14: Current to flux ratio, Heterogeneous half-assembly 2, Vacuum BCs, group 2 of 4, Diffusion Thy. w/Std, FX, FD.

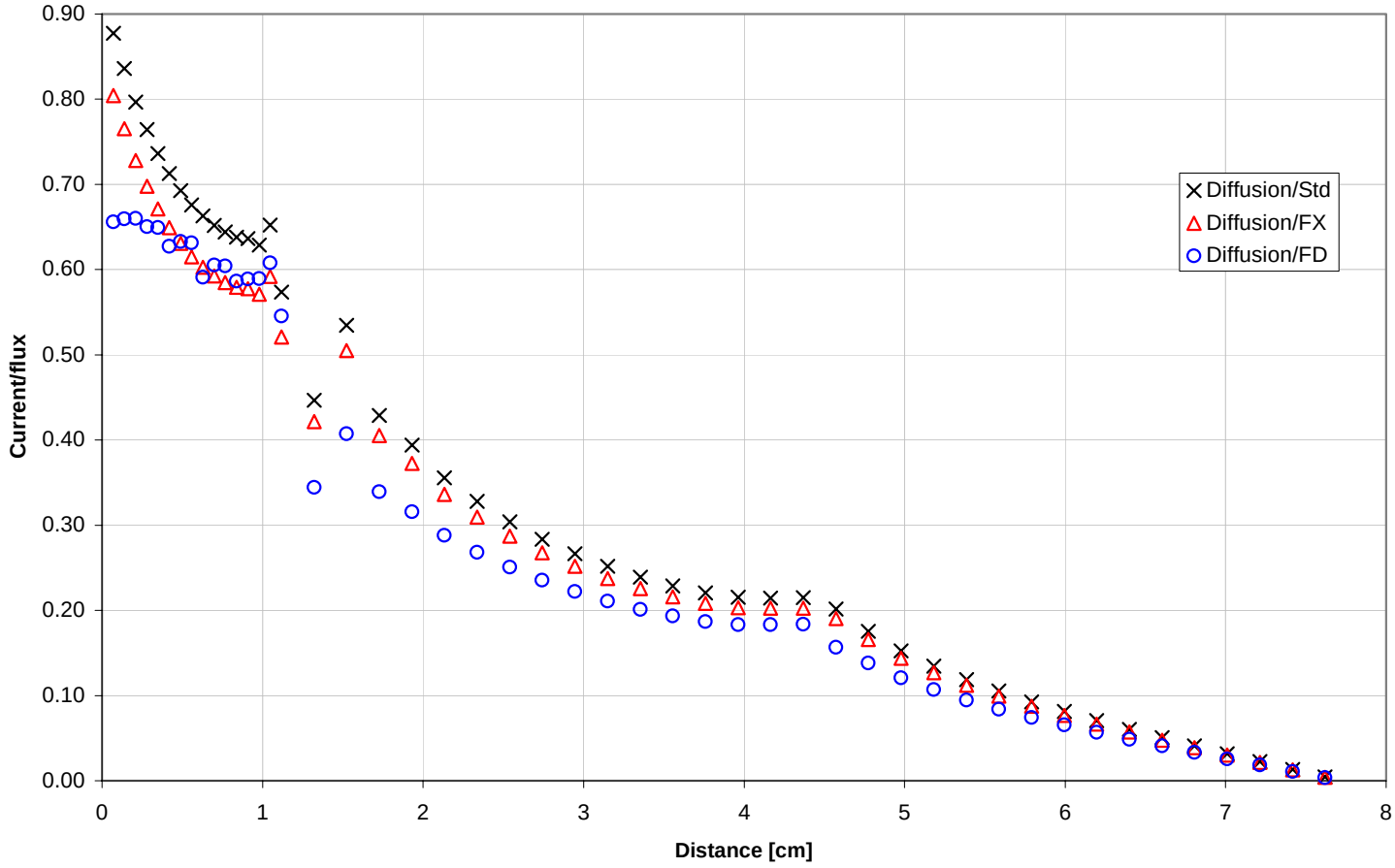

Figure 4.15: Current to flux ratio, Heterogeneous half-assembly 2, Vacuum BCs, group 1 of 4, Diffusion Thy. w/Std, FX, FD.

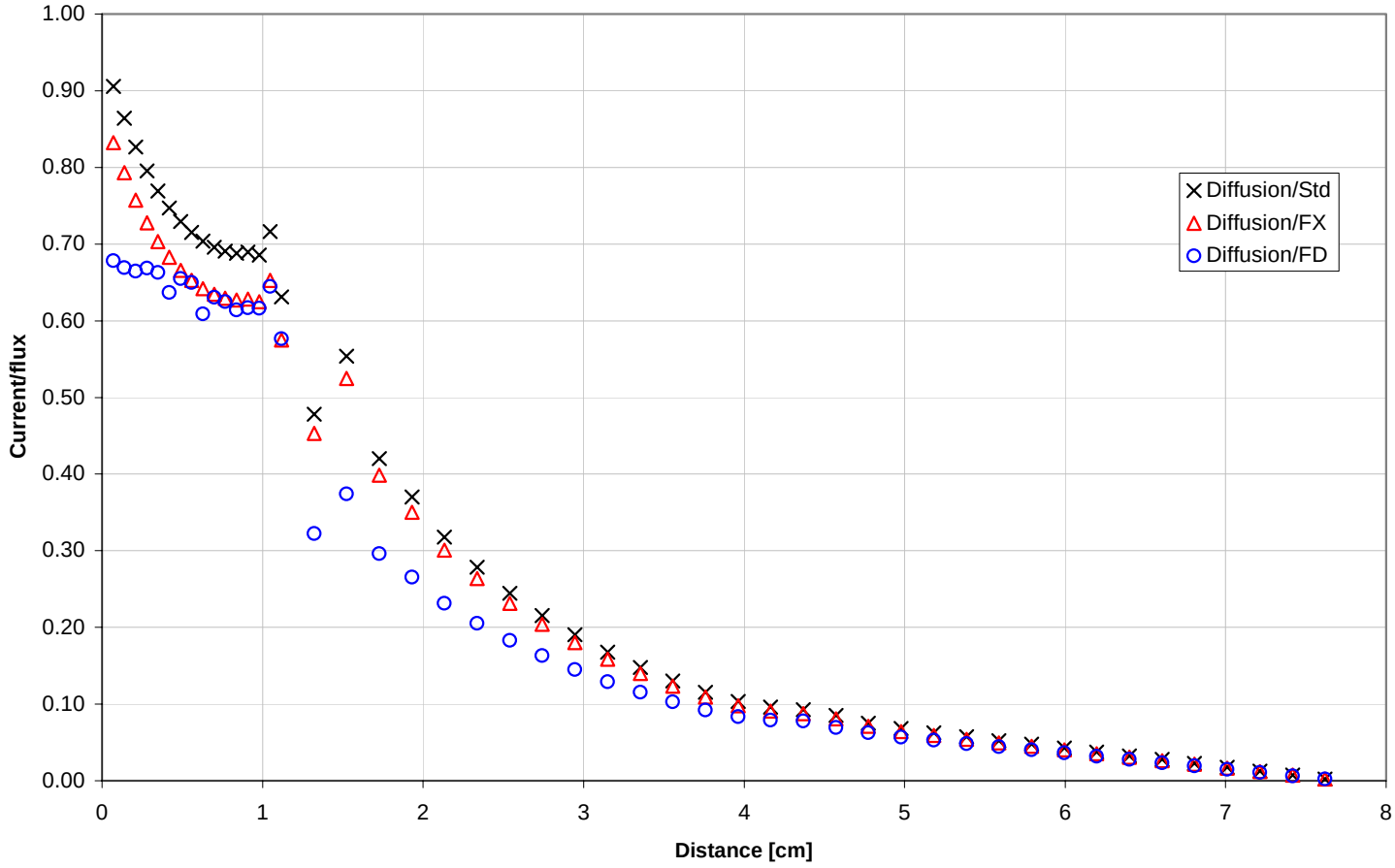

Figure 4.16: Current to flux ratio, Heterogeneous half-assembly 3, Vacuum BCs, group 1 of 4, Diffusion Thy. w/Std, FX, FD.

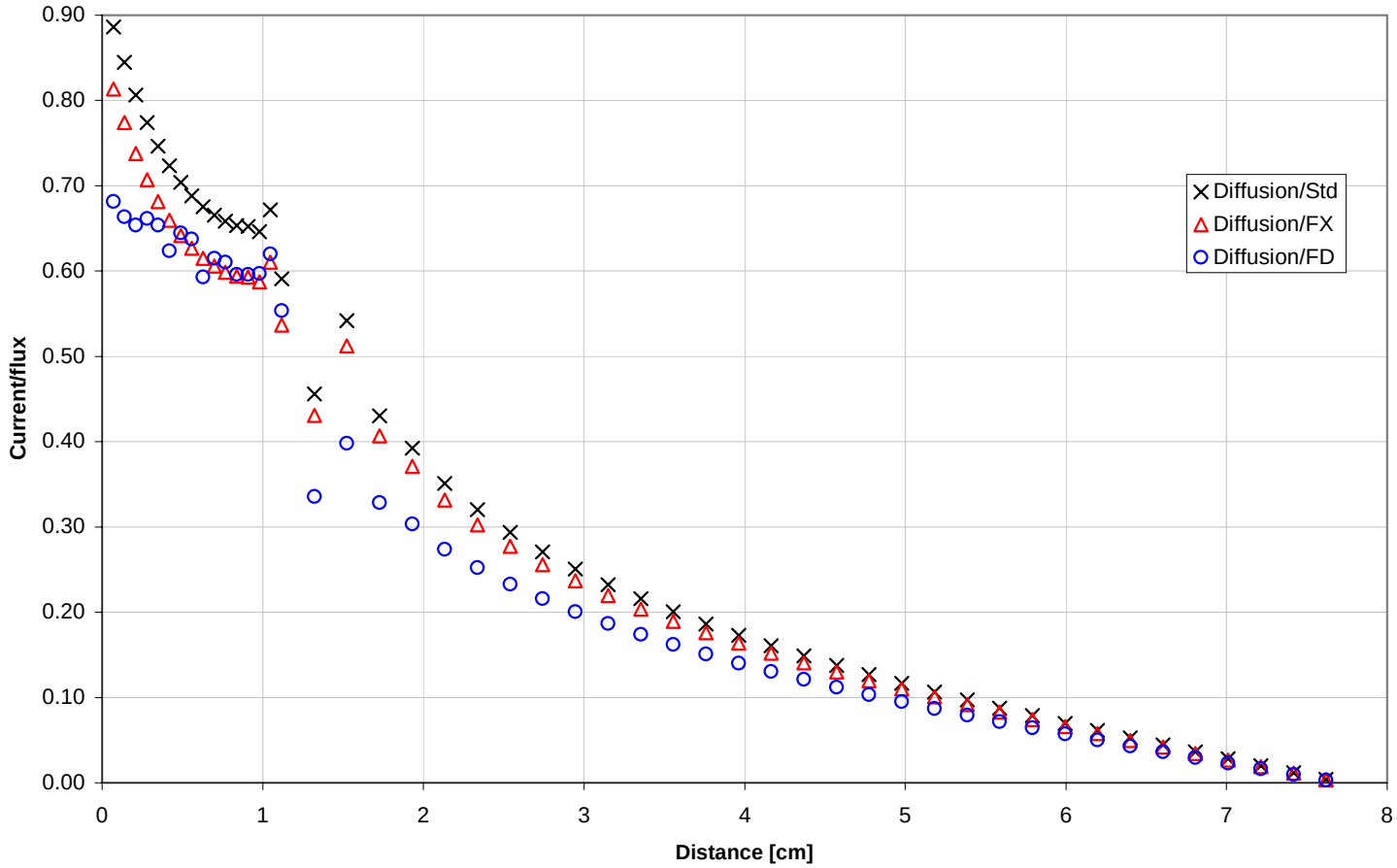

Figure 4.17: Current to flux ratio, Heterogeneous half-assembly 4, Vacuum BCs, group 1 of 4, Diffusion Thy. w/Std, FX, FD.

Table 4.6: Eigenvalues, Two groups, Heterogeneous half-assemblies, Vacuum BCs, Diffusion Thy. w/Std, FX, FD.

Assy 1				Assy 2			
Transport	Std	FX	FD	Transport	Std	FX	FD
0.414214	0.392580	0.393433	0.415074	0.455391	0.431747	0.432876	0.454412
Assy 3				Assy 4			
Transport	Std	FX	FD	Transport	Std	FX	FD
0.199868	0.189060	0.189108	0.201069	0.169543	0.162758	0.163318	0.171596

Table 4.7: Errors, Two Individual groups, Heterogeneous half-assemblies, Vacuum BCs, Diffusion Thy. w/Std, FX, FD.

	Assy 1			Assy 2		
Egy Grp	Std	FX	FD	Std	FX	FD
1	4.94	4.75	2.69	5.19	4.98	3.08
2	1.03	1.09	0.96	1.10	1.14	1.15
$error_k$	-5.22	-5.02	0.21	-5.19	-4.94	-0.22
	Assy 3			Assy 4		
Egy Grp	Std	FX	FD	Std	FX	FD
1	4.13	3.95	2.53	4.94	4.79	2.60
2	3.19	4.17	3.66	3.86	4.74	4.18
$error_k$	-5.41	-5.38	0.60	-4.00	-3.67	1.21

in Figure 4.18 through Figure 4.21. This is less apparent in the 4-group calculations in Figure 4.3, Figure 4.15, Figure 4.16, and Figure 4.17 because of instability of the current/flux ratio in this region, but is more noticeable in the 2-group results.

Another observation related to the reduction of the mesh-wise errors in 2, 4, and 47 groups is that in most of the regions that are far from the large-gradient boundaries and where error reduction takes place, the error reductions are about the same as in the large-gradient boundary regions. Examples of this can be seen in the 47- and 4-group energy-integrated results for assembly type 1 in Figure 4.6 and Figure 4.7, and for the 2-group calculations in Figure 4.22 for group 1 of assembly type 4.

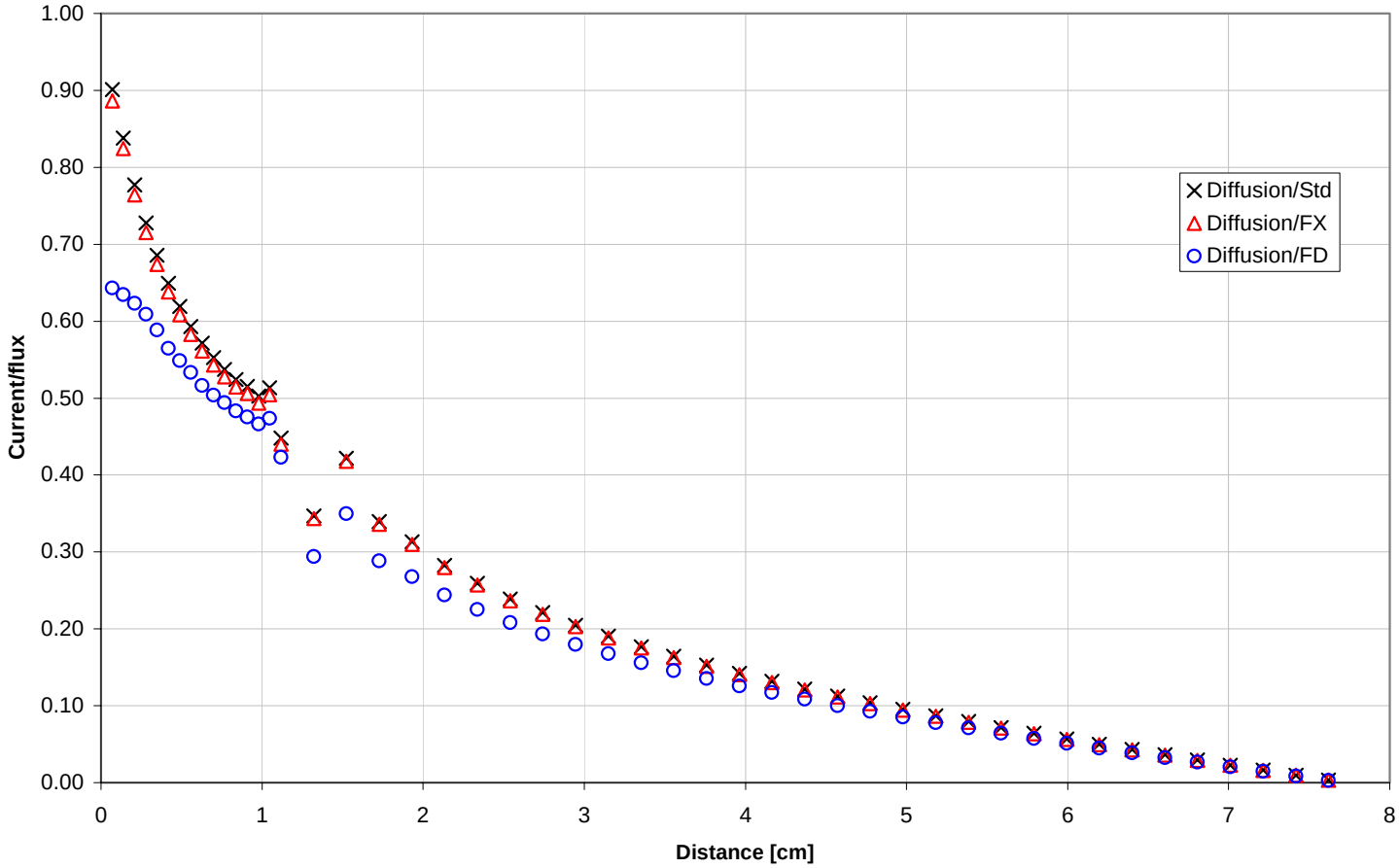

Figure 4.18: Current to flux ratio, Heterogeneous half-assembly 1, Vacuum BCs, group 1 of 2, Diffusion Thy. w/Std, FX, FD.

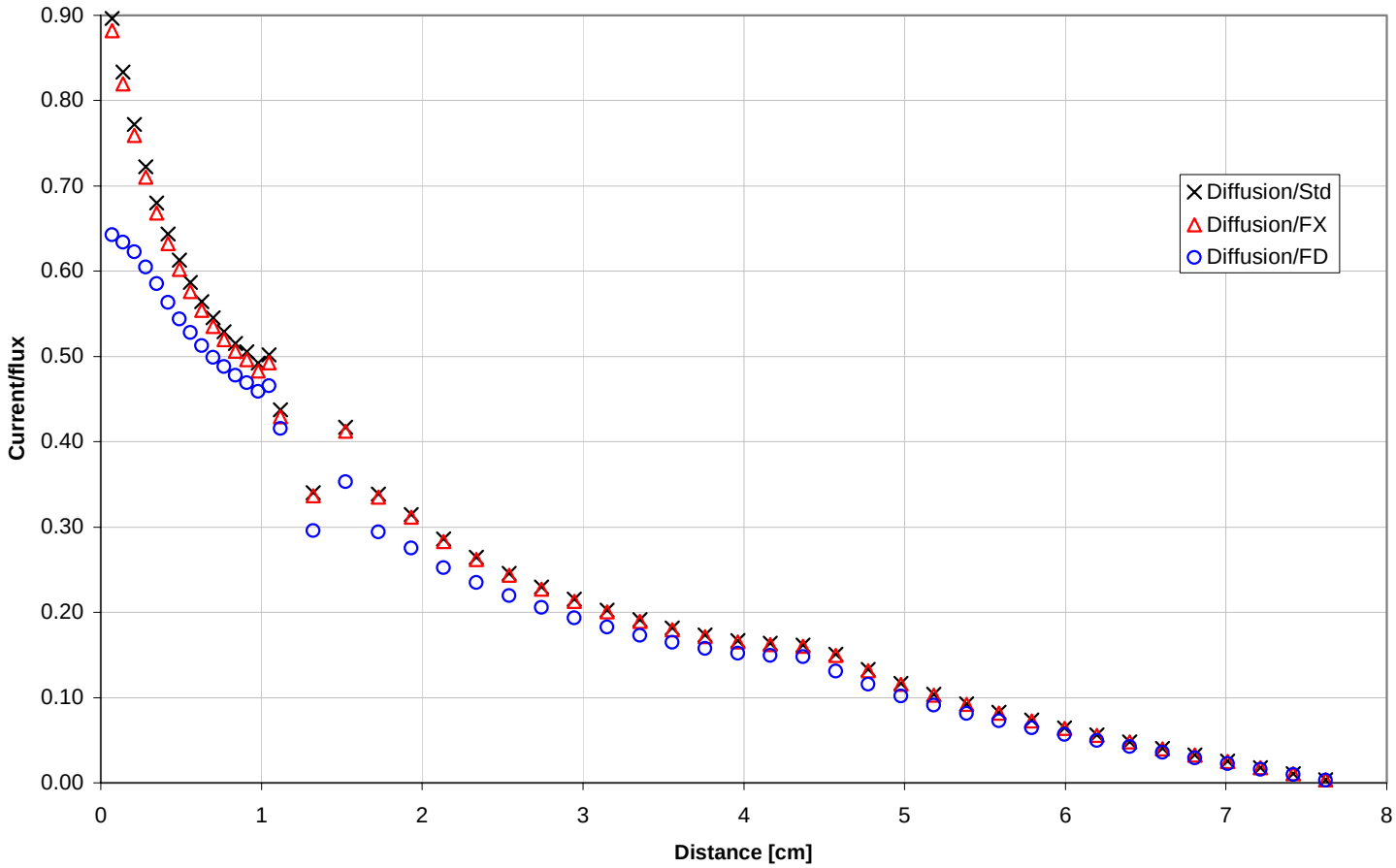

Figure 4.19: Current to flux ratio, Heterogeneous half-assembly 2, Vacuum BCs, group 1 of 2, Diffusion Thy. w/Std, FX, FD.

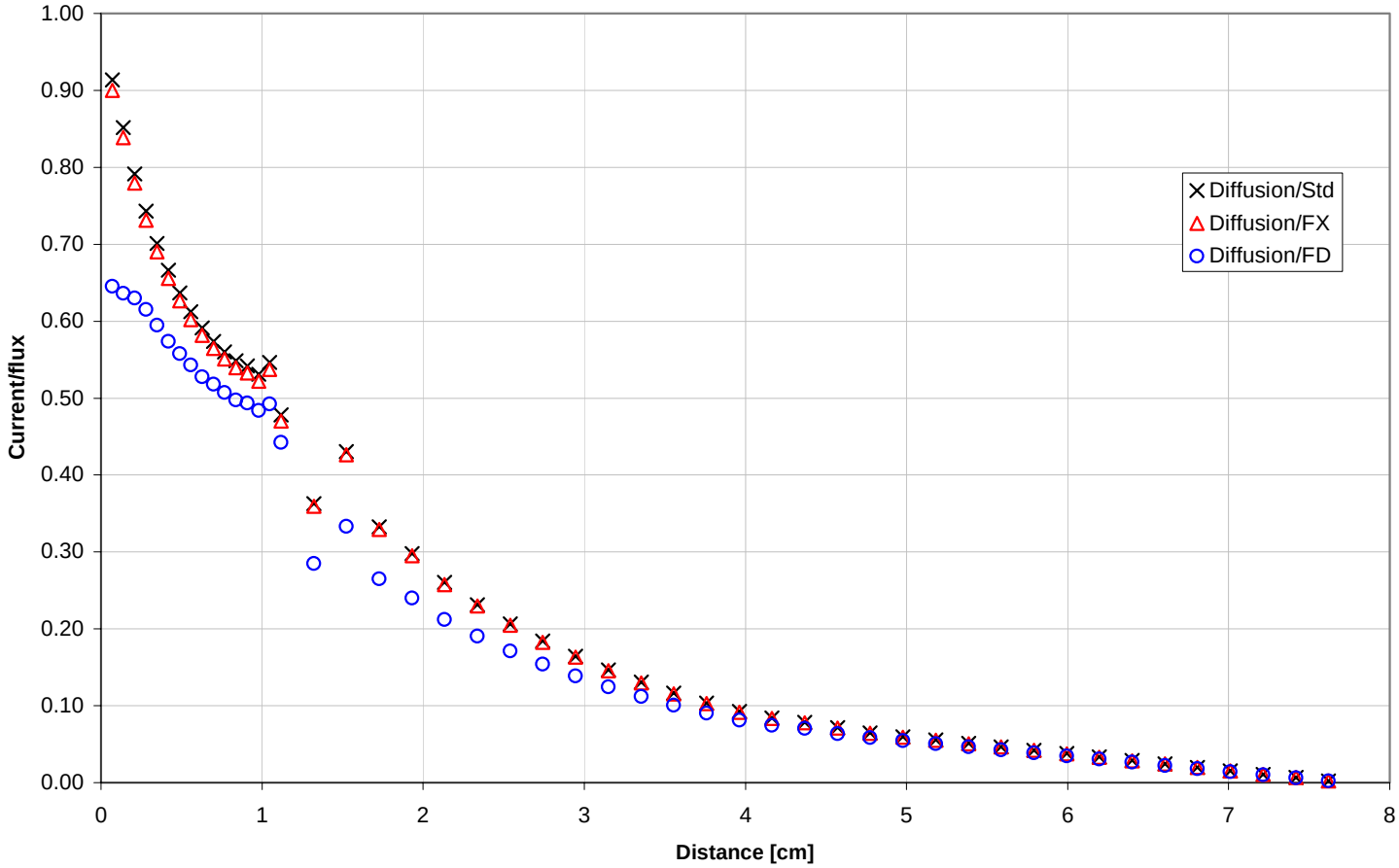

Figure 4.20: Current to flux ratio, Heterogeneous half-assembly 3, Vacuum BCs, group 1 of 2, Diffusion Thy. w/Std, FX, FD.

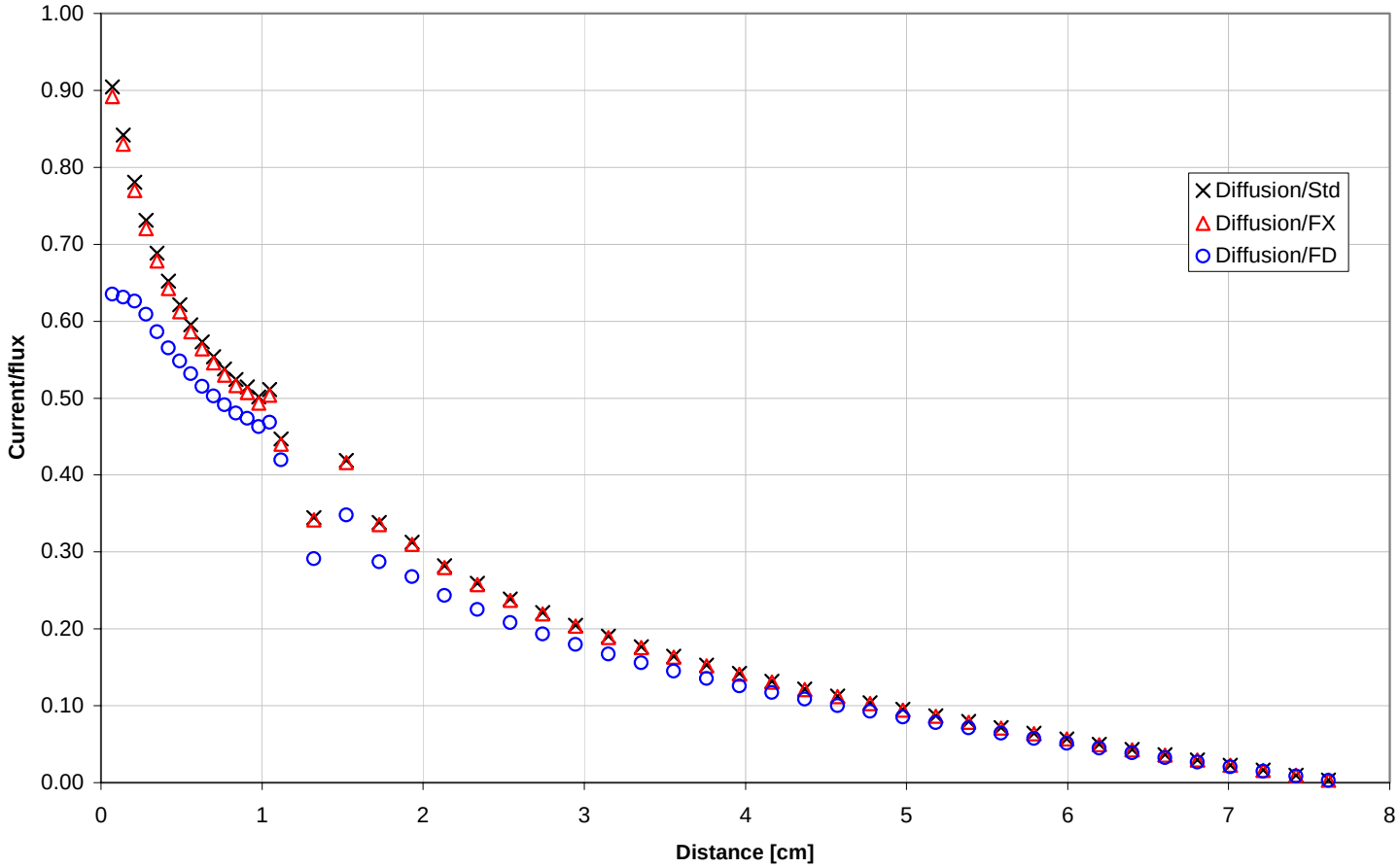

Figure 4.21: Current to flux ratio, Heterogeneous half-assembly 4, Vacuum BCs, group 1 of 2, Diffusion Thy. w/Std, FX, FD.

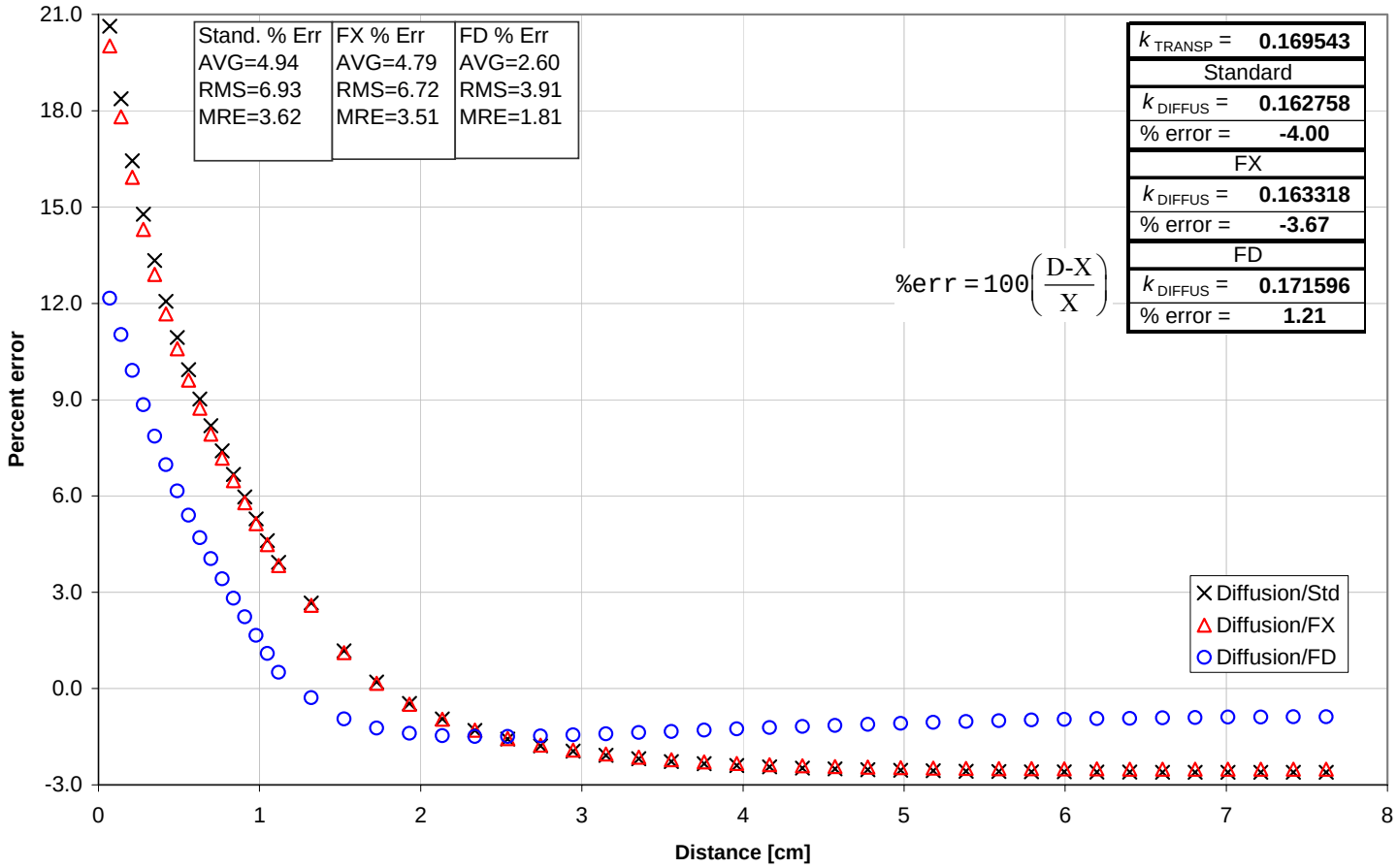

Figure 4.22: Normalized flux percent error, Heterogeneous half-assembly 4, Vacuum BCs, group 1 of 2, Diffusion Thy. w/Std, FX, FD.

4.1.2 47, 4, and 2 Groups with Reflective Boundary Conditions

The results obtained with the FD method in single-assemblies with reflective boundary conditions generally worsen the pointwise flux-errors and eigenvalue errors, although in groups 1 and 2 they reduce flux-errors in three out of four assembly types.

We begin the analysis with the 47-group energy-integrated results, whose eigenvalues are shown in Table 4.8 and error summary in Table 4.9. The results in Table 4.9 show that the FD method reduces the flux-errors in three out of the four assembly types, while worsening the eigenvalue errors compared to the Std method.

Table 4.8: Eigenvalues, Forty-seven groups, Heterogeneous half-assemblies, Reflective BCs, Diffusion Thy. w/Std, FX, FD.

Assy 1				Assy 2			
Transport	Std	FX	FD	Transport	Std	FX	FD
1.181493	1.181073	1.180740	1.180664	1.235674	1.235433	1.235268	1.235228
Assy 3				Assy 4			
Transport	Std	FX	FD	Transport	Std	FX	FD
0.614124	0.622972	0.618595	0.608026	0.322396	0.327948	0.328396	0.328023

Table 4.9: Errors, Forty-seven Energy Integrated groups, Heterogeneous half-assemblies, Reflective BCs, Diffusion Thy. w/Std, FX, FD.

	Assy 1			Assy 2		
Egy Grp	Std	FX	FD	Std	FX	FD
All	1.14	0.90	0.81	1.50	1.16	1.08
$error_k$	-0.04	-0.06	-0.07	-0.02	-0.03	-0.04
	Assy 3			Assy 4		
Egy Grp	Std	FX	FD	Std	FX	FD
All	1.62	1.64	1.82	2.35	1.87	1.25
$error_k$	-1.44	-0.73	-0.99	1.72	1.86	1.75

The 4-group energy-integrated results, whose eigenvalues and flux-errors are shown in Table 4.10 and Table 4.11 , also indicate that in most of the assemblies the FD reduces flux-errors and worsens eigenvalue errors compared to the Std method. This might cause one to conclude that in 4 groups the FD method reduces flux-errors most of the time.

Table 4.10: Eigenvalues, Four groups, Heterogeneous half-assemblies, Reflective BCs, Diffusion Thy. w/Std, FX, FD.

Assy 1				Assy 2			
Transport	Std	FX	FD	Transport	Std	FX	FD
1.182742	1.183262	1.183235	1.183226	1.236897	1.237432	1.237559	1.237615
Assy 3				Assy 4			
Transport	Std	FX	FD	Transport	Std	FX	FD
0.608375	0.604507	0.600772	0.596936	0.322793	0.327468	0.327850	0.328404

Table 4.11: Errors, Four Energy Integrated groups, Heterogeneous half-assemblies, Reflective BCs, Diffusion Thy. w/Std, FX, FD.

	Assy 1			Assy 2		
Egy Grp	Std	FX	FD	Std	FX	FD
All	1.06	0.83	0.76	1.34	1.03	0.97
$error_k$	0.04	0.04	0.04	0.04	0.05	0.06
	Assy 3			Assy 4		
Egy Grp	Std	FX	FD	Std	FX	FD
All	1.62	1.64	1.83	1.51	1.11	0.89
$error_k$	-0.64	-1.25	-1.88	1.45	1.57	1.74

But the individual 4-group results in Table 4.12 below show that the FD results for group 1 and 2 reduce errors in 3 of the 4 assembly types (6 results), while they worsen errors in the remaining groups and assembly types (10 results), thus worsening the flux errors most

of the time. This contradiction between energy-integrated and individual energy group results is caused by error cancellation, which can be seen by comparing the two types of results in 4 groups, as in the assembly type 2 case shown in Figure 4.23 through Figure 4.27. These figures show that for a particular mesh point the errors alternate between positive and negative values when going from group 1 to group 4 in Figure 4.23 through Figure 4.26, and when they're "averaged" during the calculation of the energy-integrated error, shown in Figure 4.27, the value is between the four values. It has also been confirmed that error cancellation took place in the 2-group calculations. Because of this, the strong possibility exists that error cancellation also took place in the 47-group energy-integrated flux-errors, which makes those results questionable. For the purpose of calculating the eigenvalue errors, however, the 47-group energy-integrated results shown Table 4.9 above are perfectly useful. From hereon only individual group errors will be shown for the single assemblies with reflective boundary condition.

Table 4.12: Errors, Four Individual groups, Heterogeneous half-assemblies, Reflective BCs, Diffusion Thy. w/Std, FX, FD.

	Assy 1			Assy 2		
Egy Grp	Std	FX	FD	Std	FX	FD
1	3.08	2.85	2.78	3.33	3.02	2.98
2	0.99	0.88	0.83	1.33	1.07	1.03
3	0.84	0.95	0.95	0.85	0.92	0.92
4	1.47	1.74	1.78	1.47	1.84	1.87
$error_k$	0.04	0.04	0.04	0.04	0.05	0.06
	Assy 3			Assy 4		
Egy Grp	Std	FX	FD	Std	FX	FD
1	2.86	2.75	2.80	3.30	3.02	2.97
2	0.72	0.72	0.76	1.17	1.03	0.98
3	1.62	1.97	1.98	1.48	1.79	1.85
4	2.36	3.27	4.55	8.00	10.25	13.34
$error_k$	-0.64	-1.25	-1.88	1.45	1.57	1.74

According to the 2-group eigenvalues and errors in Table 4.13 and Table 4.14 on page 79, the 2-group calculations yield the same general results as the 4-group calculations. The FD method slightly improves the flux-errors in group 1 and slightly worsens them in group 2, and slightly worsens the eigenvalues. In 2 groups, as in 4 groups, and unlike the vacuum boundary condition results, there is no clearly superior diffusion coefficient with reflective boundary conditions, for all groups.

There are a couple of other useful observations from results thus far. The current/flux ratio graphs show that the ratios near the assembly boundary with the reflective boundaries are much lower than in the vacuum case, but there are other regions where the current/flux ratios reach a strong local peak with both type of boundary conditions. These are regions where gadolinium borders another material, and occur in assembly types 3 and 4, group 4 in the 4-group calculations and group 2 in the 2-group calculations, which are the thermal groups. For example, Figure 4.28 and Figure 4.29 show the current/flux ratios and flux-errors, respectively, for assembly type 4 with vacuum boundary conditions, and for comparison, Figure 4.30 and Figure 4.31 show the same type of output with reflective conditions. In both the vacuum and reflective cases, the current/flux ratios are high in these gadolinium interface regions, located at about 1.1 cm, and the FD does not reduce flux errors here in either case. But there is a difference between the vacuum and reflective results, which is that with vacuum boundaries the FD method reduces errors in most of the other regions, while with reflective boundaries the FD worsens errors throughout the entire assembly.

In the analysis of single assemblies with vacuum boundary conditions in section 4.1.1, there was discussion of error reductions in regions not having large gradients and

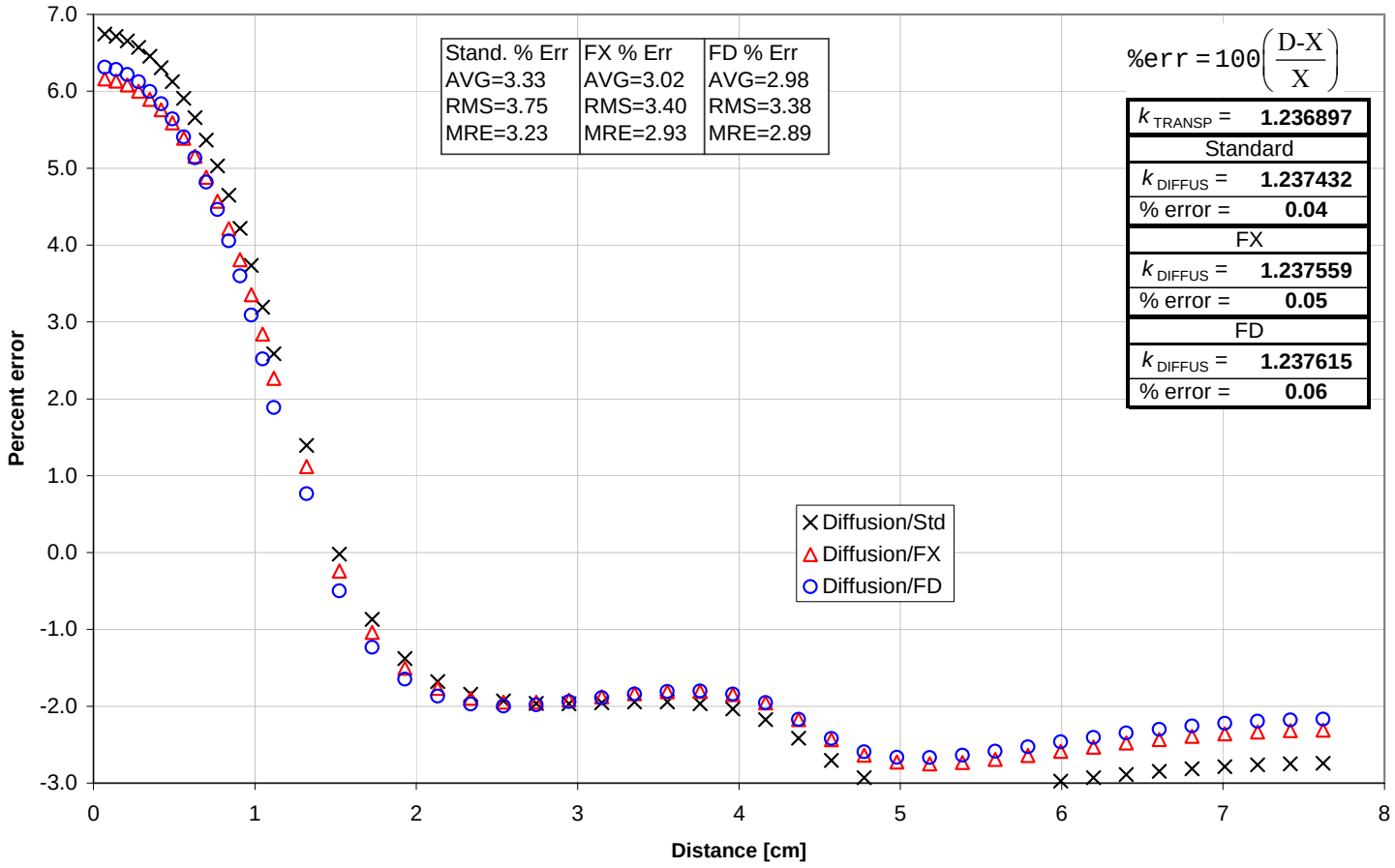

Figure 4.23: Normalized flux percent error, Heterogeneous half-assembly 2, Reflective BCs, group 1 of 4, Diffusion Thy. w/Std, FX, FD.

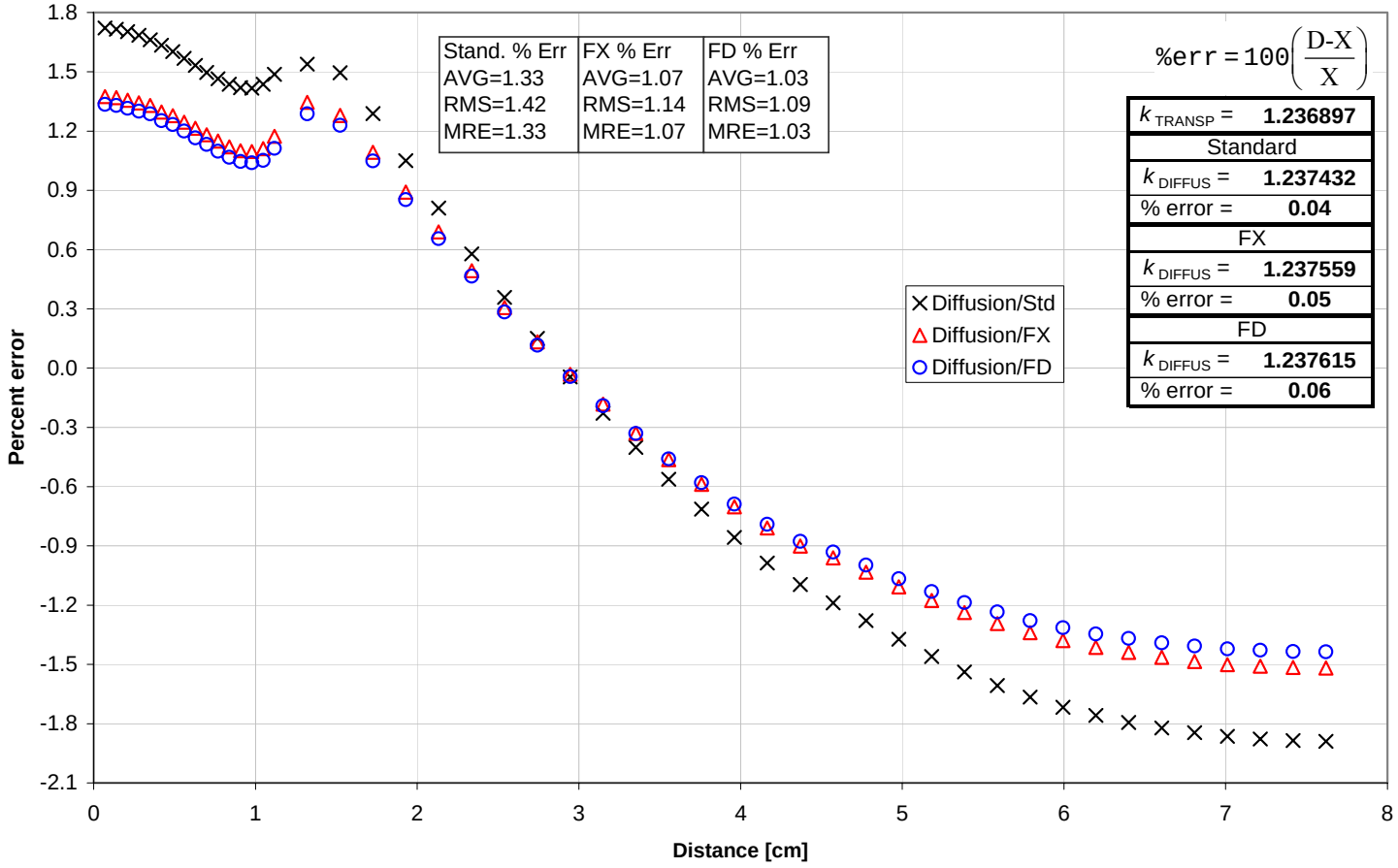

Figure 4.24: Normalized flux percent error, Heterogeneous half-assembly 2, Reflective BCs, group 2 of 4, Diffusion Thy. w/Std, FX, FD.

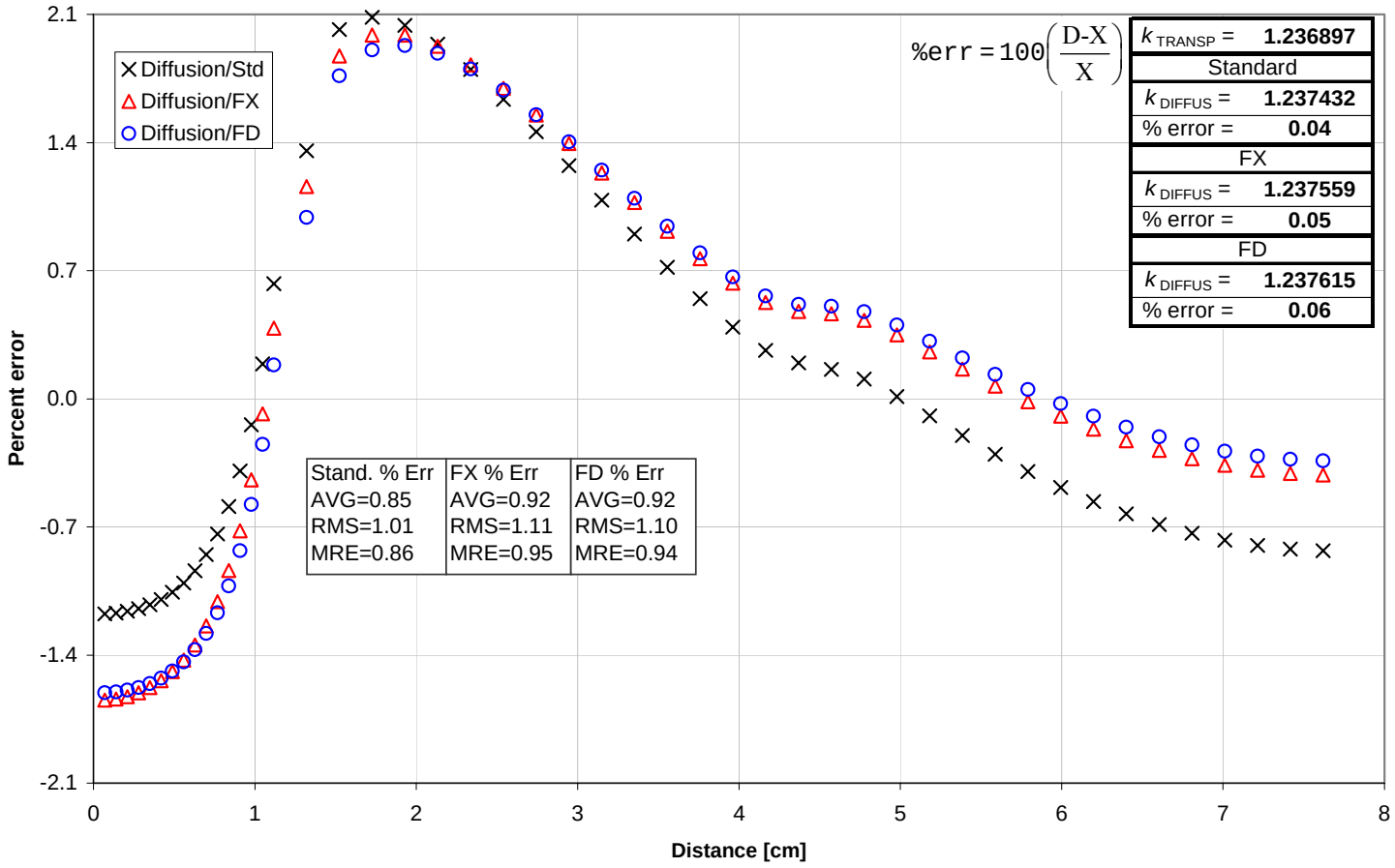

Figure 4.25: Normalized flux percent error, Heterogeneous half-assembly 2, Reflective BCs, group 3 of 4, Diffusion Thy. w/Std, FX, FD.

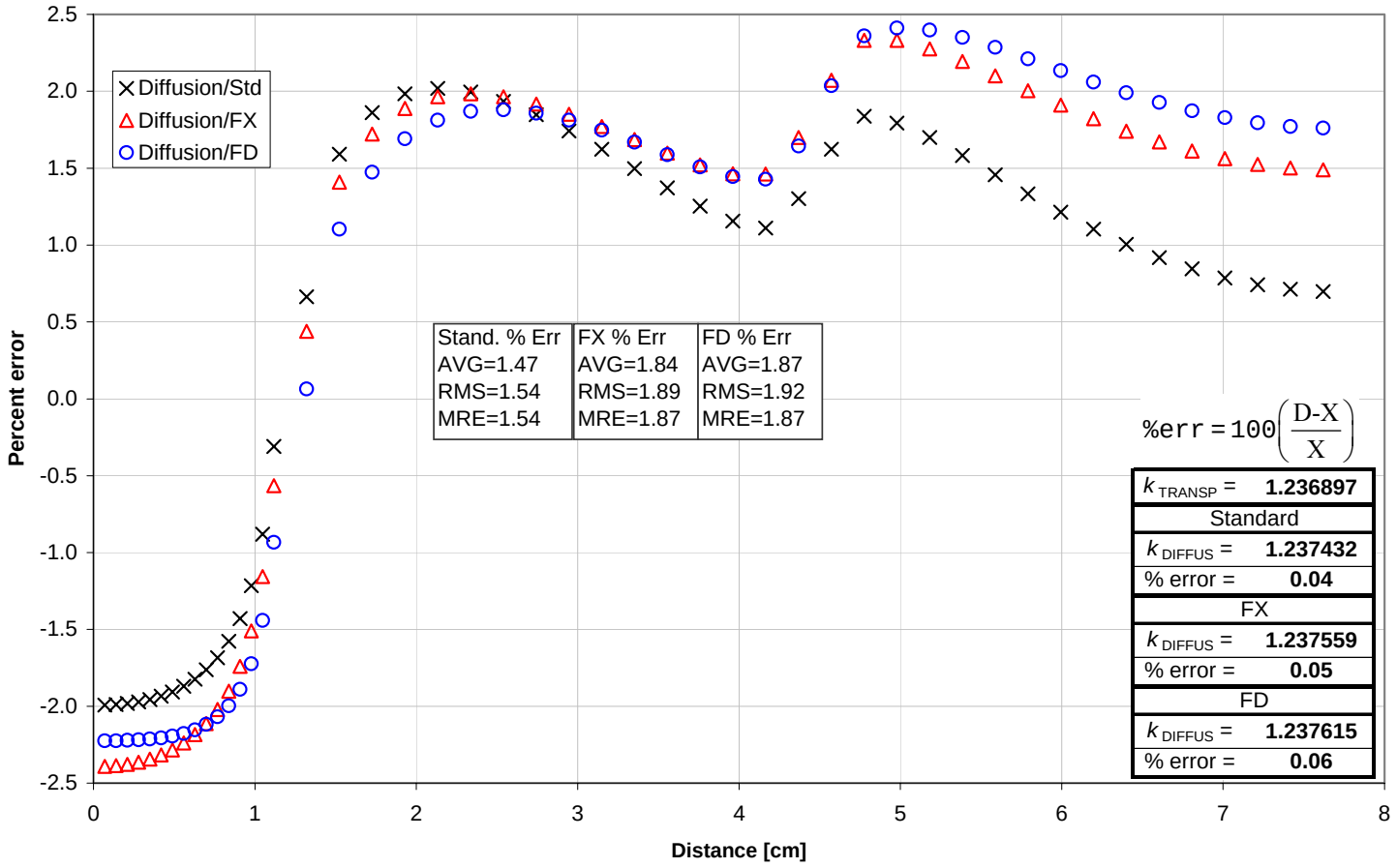

Figure 4.26: Normalized flux percent error, Heterogeneous half-assembly 2, Reflective BCs, group 4 of 4, Diffusion Thy. w/Std, FX, FD.

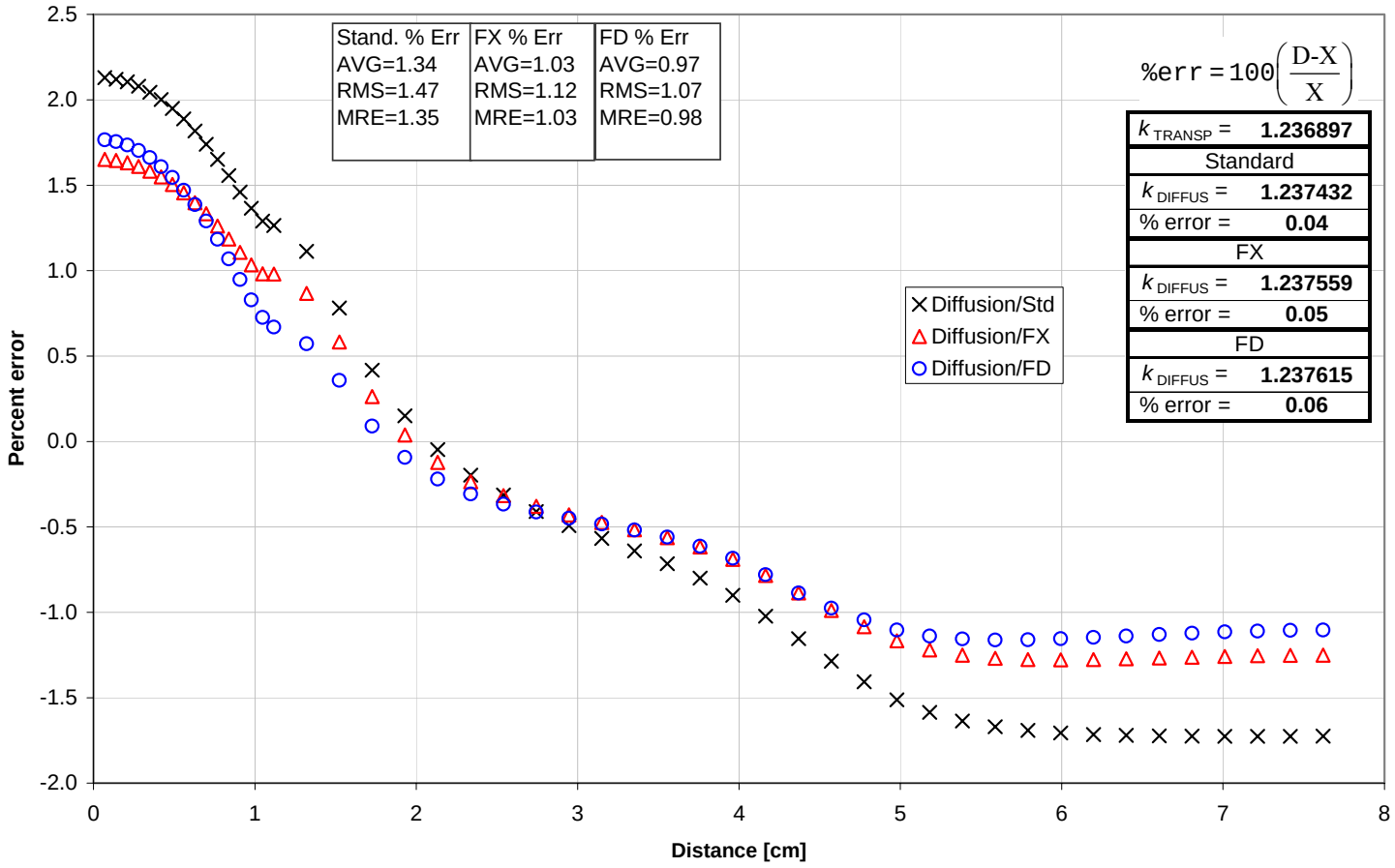

Figure 4.27: Normalized flux percent error, Heterogeneous half-assembly 2, Reflective BCs, 4 groups, Diffusion Thy. w/Std, FX, FD.

Table 4.13: Eigenvalues, Two groups, Heterogeneous half-assemblies, Reflective BCs, Diffusion Thy. w/Std, FX, FD.

Assy 1				Assy 2			
Transport	Std	FX	FD	Transport	Std	FX	FD
1.182357	1.184616	1.184689	1.184688	1.236606	1.238704	1.238901	1.238966
Assy 3				Assy 4			
Transport	Std	FX	FD	Transport	Std	FX	FD
0.608448	0.605303	0.602343	0.598567	0.323357	0.327861	0.328012	0.328567

Table 4.14: Errors, Two Individual groups, Heterogeneous half-assemblies, Reflective BCs, Diffusion Thy. w/Std, FX, FD.

	Assy 1			Assy 2		
Egy Grp	Std	FX	FD	Std	FX	FD
1	1.58	1.53	1.51	1.71	1.65	1.63
2	0.86	1.05	1.09	0.83	1.04	1.06
$error_k$	0.19	0.20	0.20	0.17	0.19	0.19
	Assy 3			Assy 4		
Egy Grp	Std	FX	FD	Std	FX	FD
1	1.75	1.74	1.78	1.56	1.52	1.51
2	1.98	2.67	4.07	5.31	7.08	10.06
$error_k$	-0.52	-1.00	-1.62	1.39	1.44	1.61

current/flux ratios. These error reductions also occur in these same mesh points and energy groups using reflective boundary conditions, but to a smaller extent. The corresponding results for the reflective cases for assembly 1 group 1 have flux in Figure 4.32 (Figure 4.1 is with vacuum), flux-errors in Figure 4.33 (Figure 4.2 vacuum), and current/flux ratios in Figure 4.34 (Figure 4.3 vacuum). Figure 4.33 shows that the FD reduces errors at points greater than 2 cm, completely inside the fuel region, where according to Figure 4.34, the current/flux ratios are lower than with the vacuum case in Figure 4.3, and where Figure 4.32 shows that the gradients are relatively low, ranging from about 0.89 to 1.06, while in the vacuum case in Figure 4.1 the flux ranges from

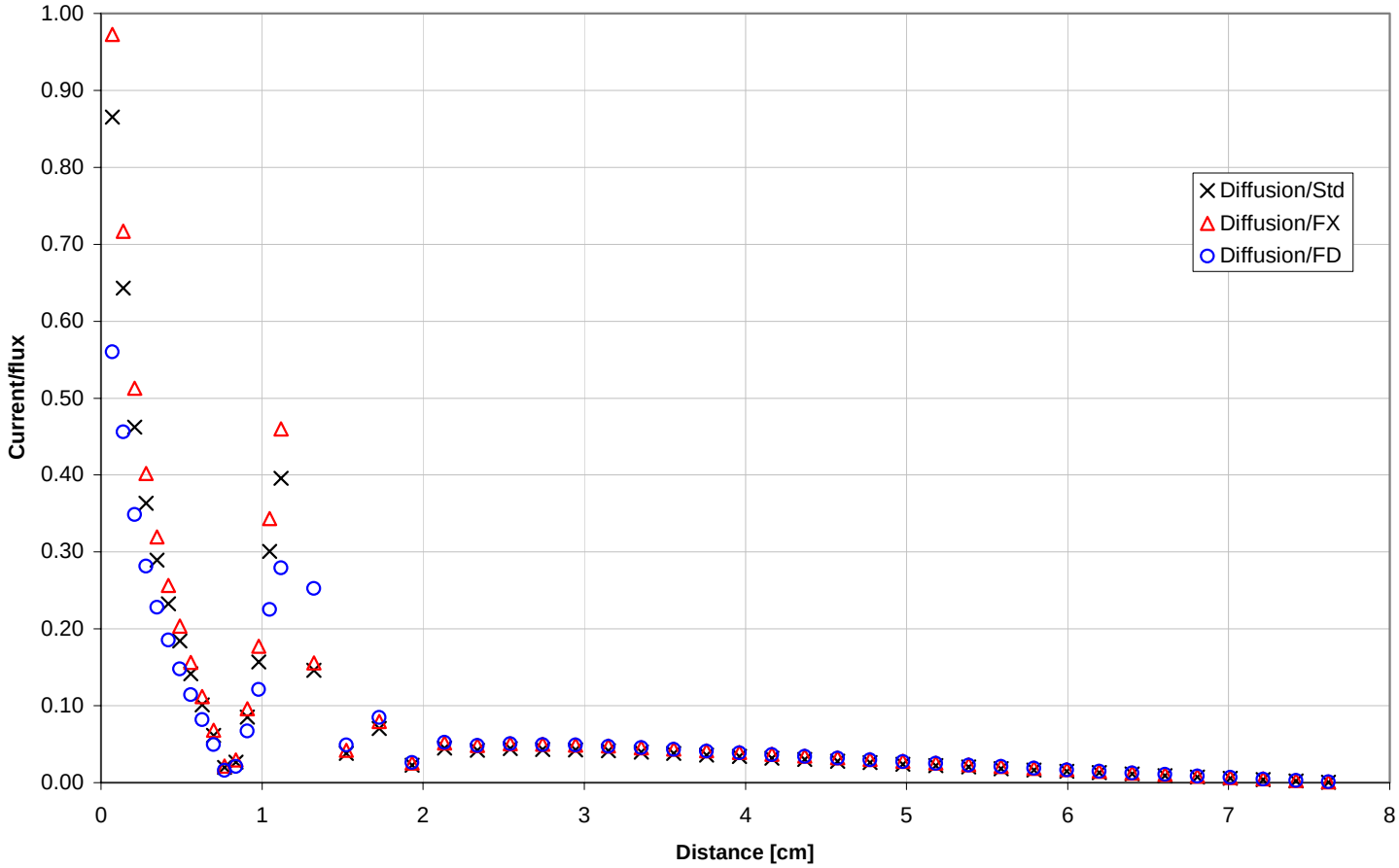

Figure 4.28: Current to flux ratio, Heterogeneous half-assembly 4, Vacuum BCs, group 4 of 4, Diffusion Thy. w/Std, FX, FD.

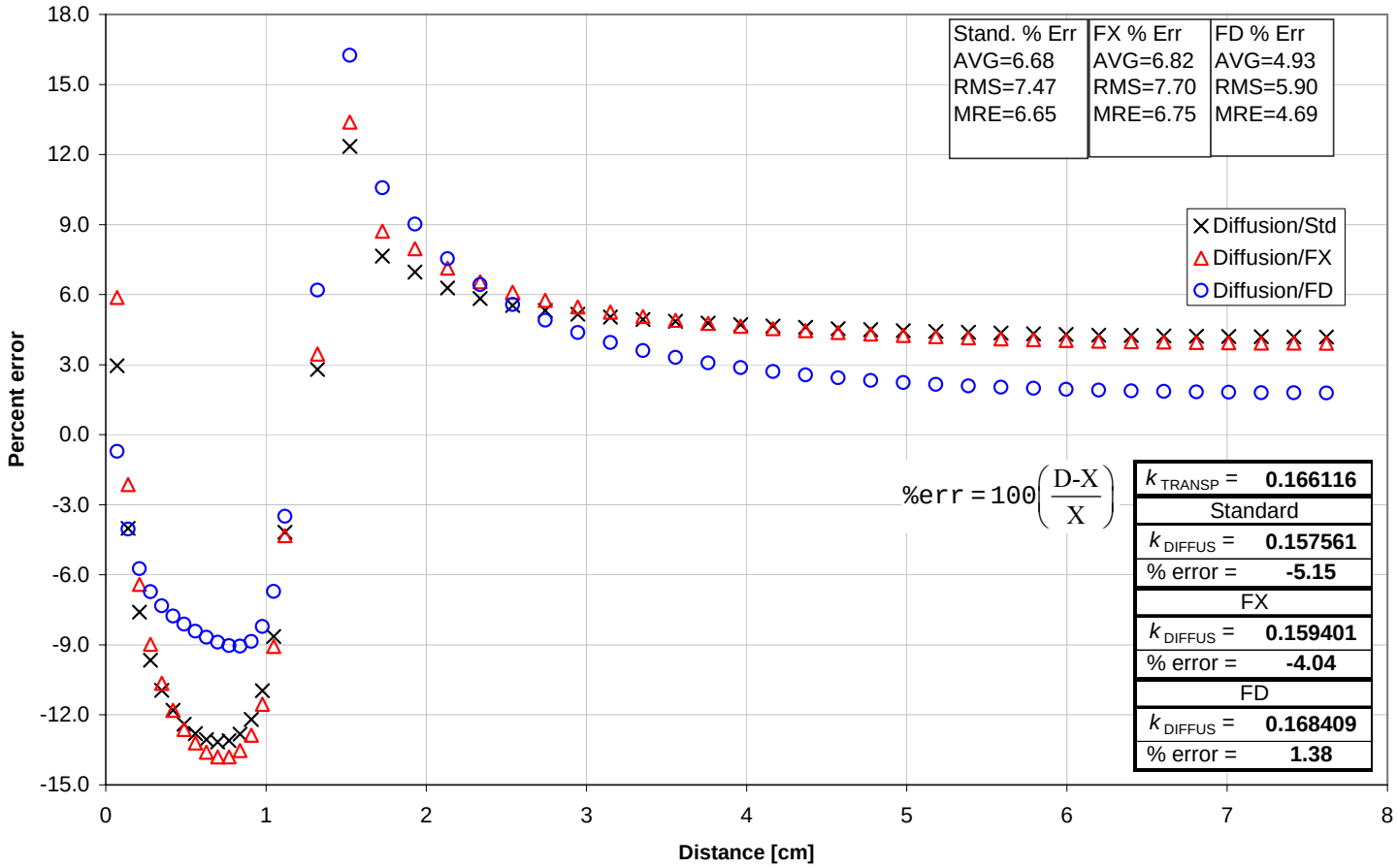

Figure 4.29: Normalized flux percent error, Heterogeneous half-assembly 4, Vacuum BCs, group 4 of 4, Diffusion Thy. w/Std, FX, FD.

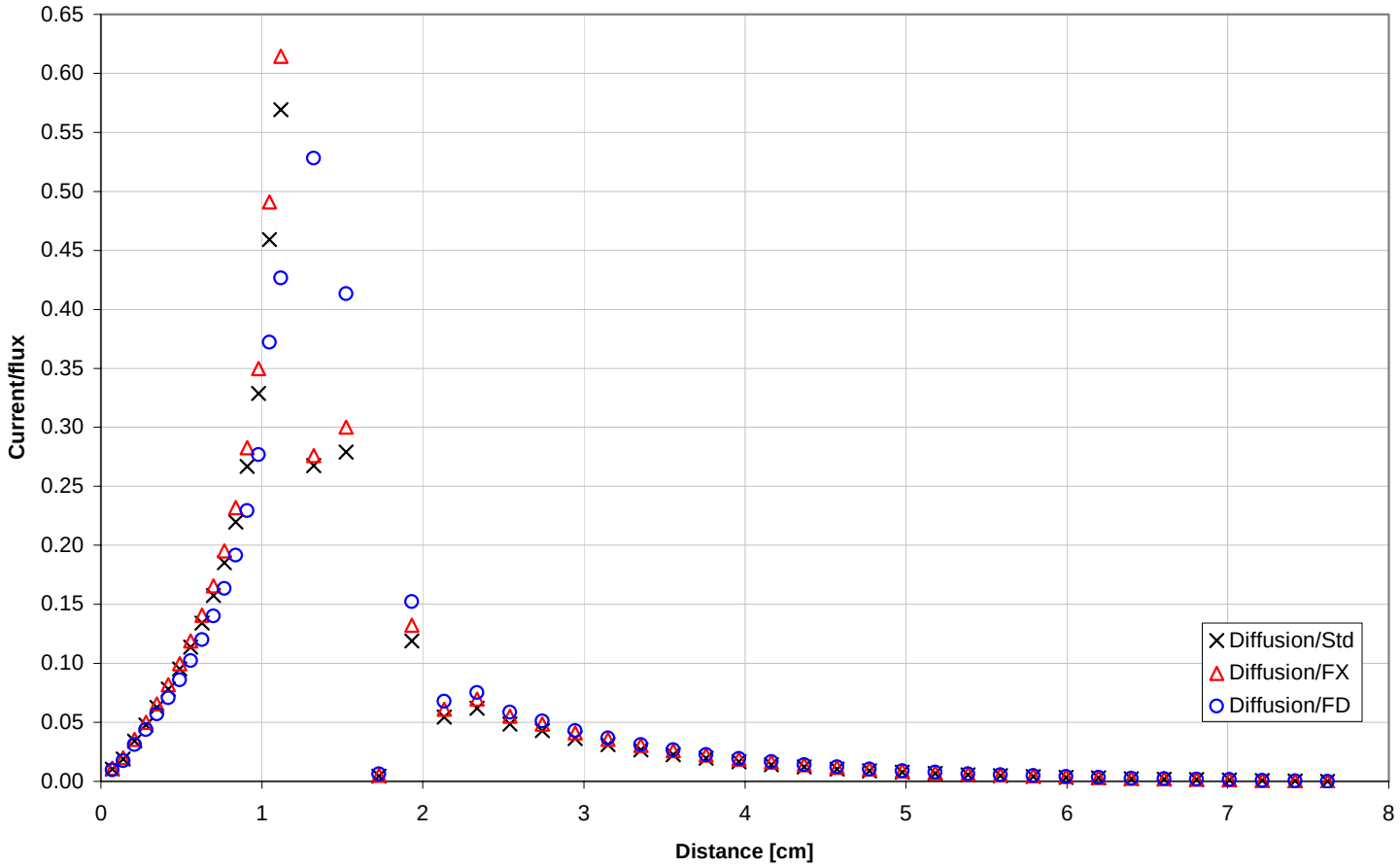

Figure 4.30: Current to flux ratio, Heterogeneous half-assembly 4, Reflective BCs, group 4 of 4, Diffusion Thy. w/Std, FX, FD.

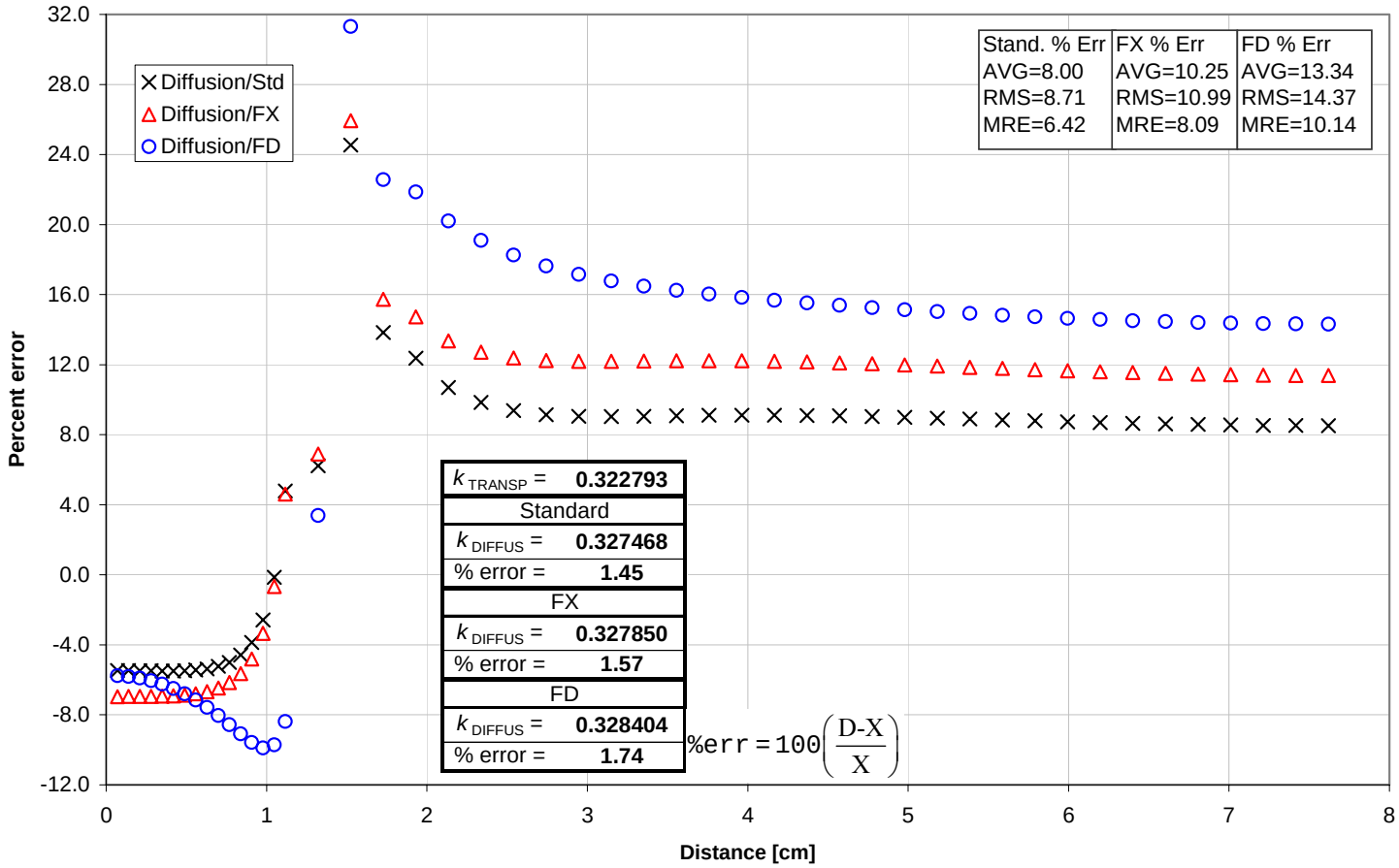

Figure 4.31: Normalized flux percent error, Heterogeneous half-assembly 4, Reflective BCs, group 4 of 4, Diffusion Thy. w/Std, FX, FD.

about 0.4 to 1.5. The assembly 2 group 2 fluxes are in Figure 4.35, flux-errors in Figure 4.36, and the current/flux ratios in Figure 4.37, and can be compared against Figure 4.12, Figure 4.13, and Figure 4.14. All of these plots further indicate that even in the absence of large gradients the FD method sometimes reduces flux-errors, resulting from a characteristic other than flux-limiting.

As a verification of the validity of the results, we see that for both the 2- and 4-group energy structures, the flux-error profiles with their accompanying collective error measures, and eigenvalue errors, show that the errors based on each of the three diffusion coefficients are smaller using the reflective boundary conditions than they are with vacuum boundary conditions because of diminished transport effects. The errors near the assembly boundary also don't peak as high as in the vacuum boundary conditions.

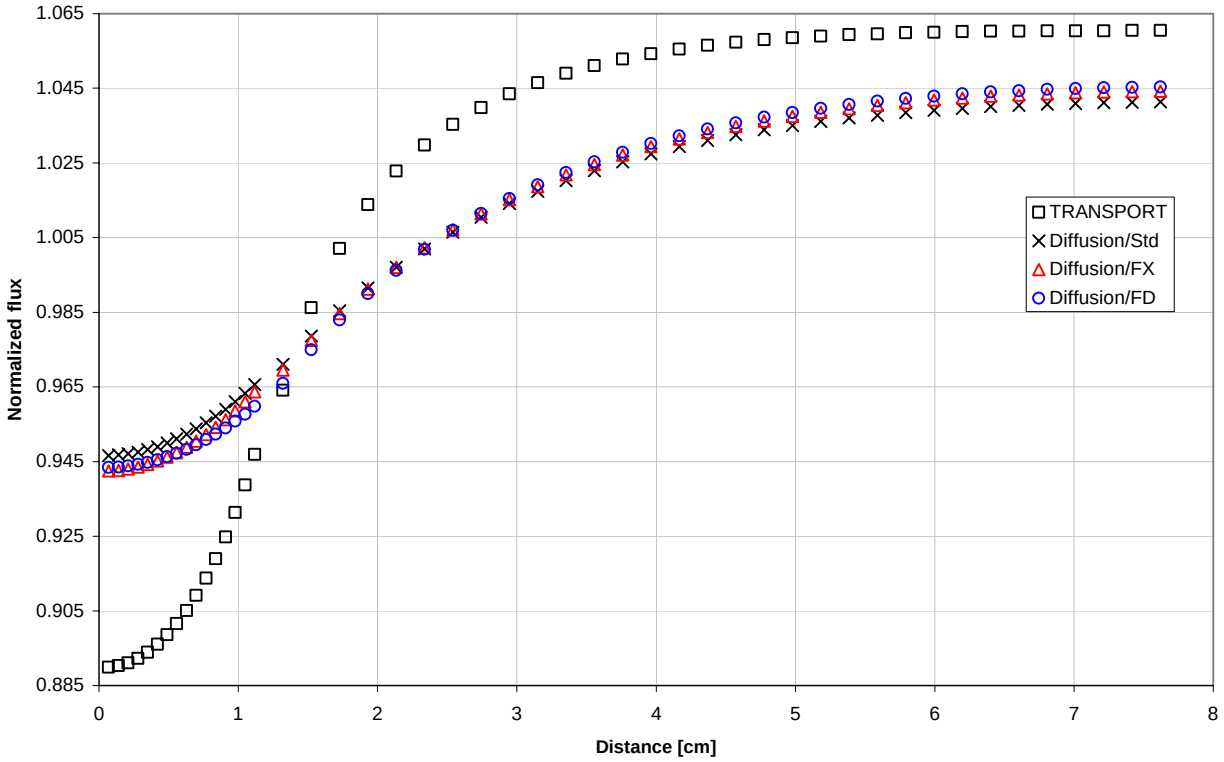

Figure 4.32: Normalized flux, Heterogeneous half-assembly 1, Reflective BCs, group 1 of 4, Transport and Diffusion Thy. w/Std, FX, FD.

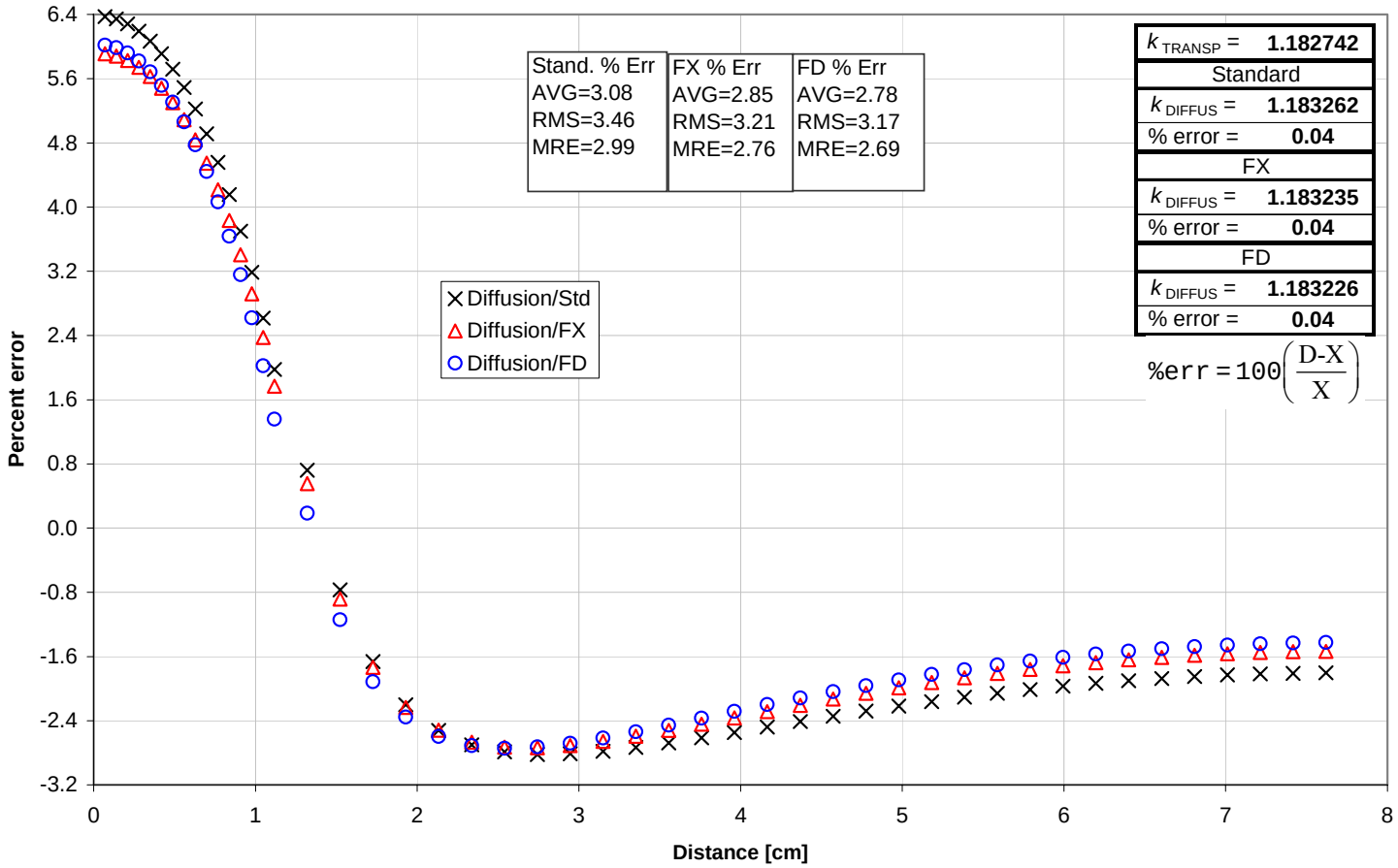

Figure 4.33: Normalized flux percent error, Heterogeneous half-assembly 1, Reflective BCs, group 1 of 4, Diffusion Thy. w/Std, FX, FD.

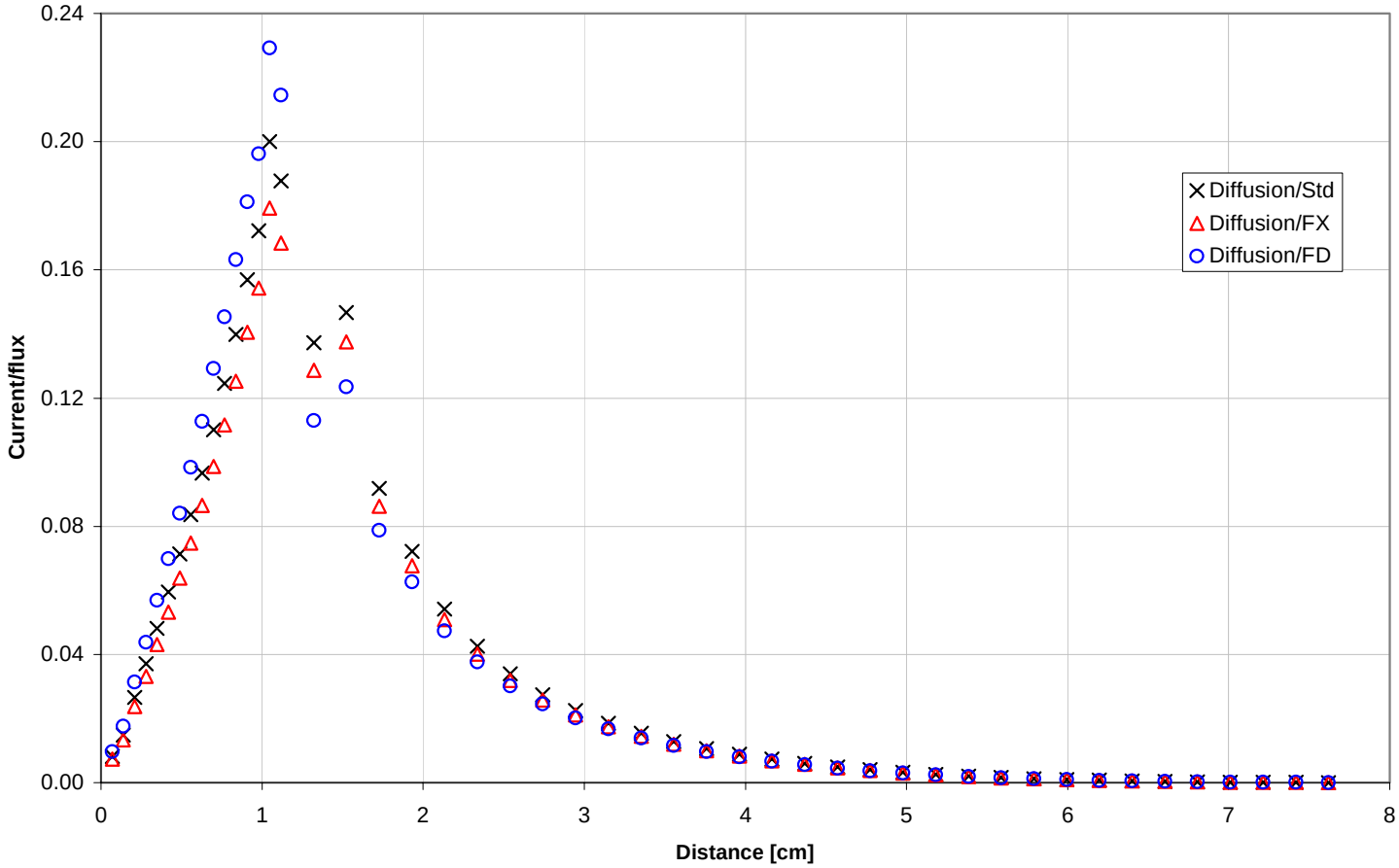

Figure 4.34: Current to flux ratio, Heterogeneous half-assembly 1, Reflective BCs, group 1 of 4, Diffusion Thy. w/Std, FX, FD.

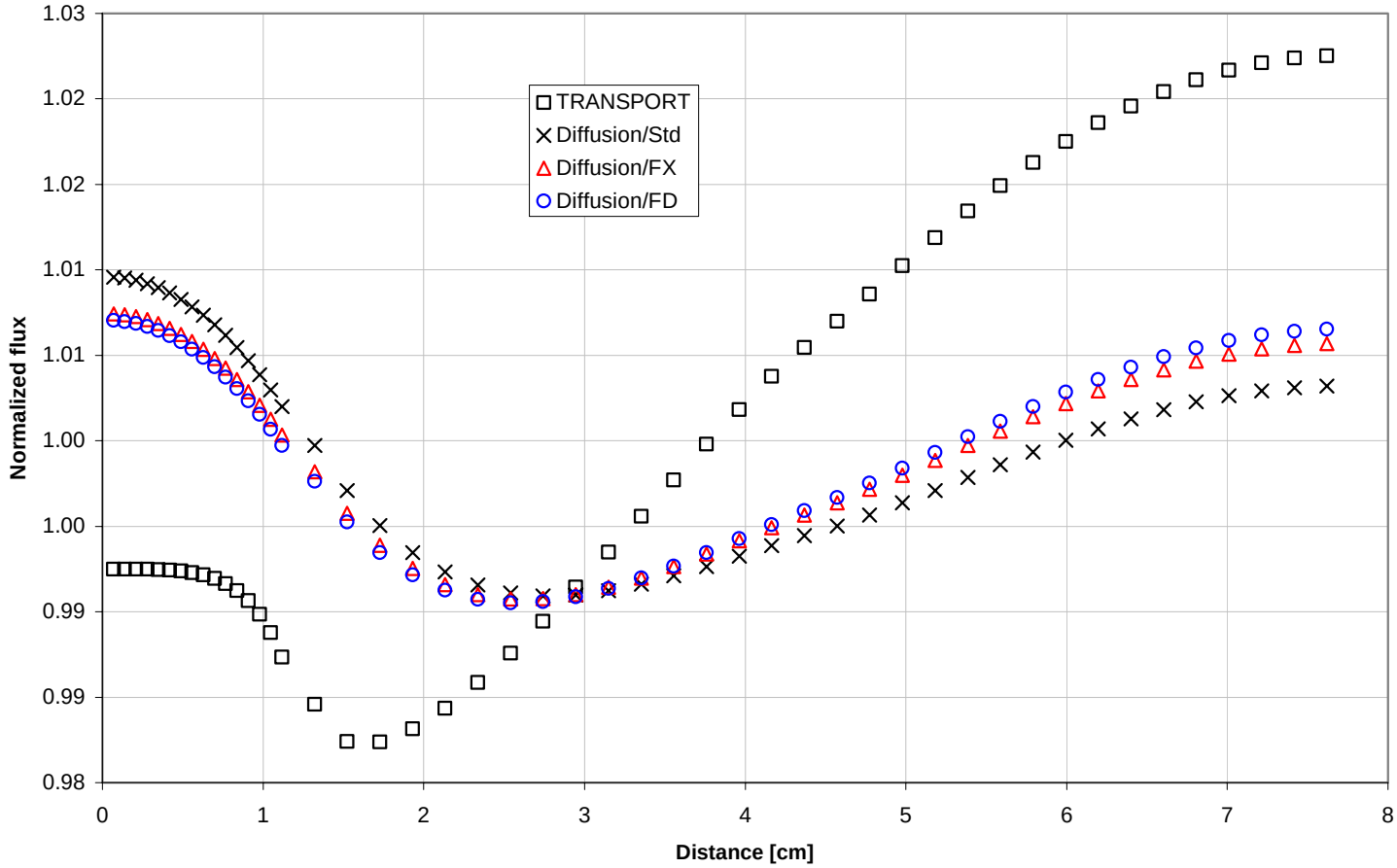

Figure 4.35: Normalized flux, Heterogeneous half-assembly 2, Reflective BCs, group 2 of 4, Transport and Diffusion Thy. w/Std, FX, FD.

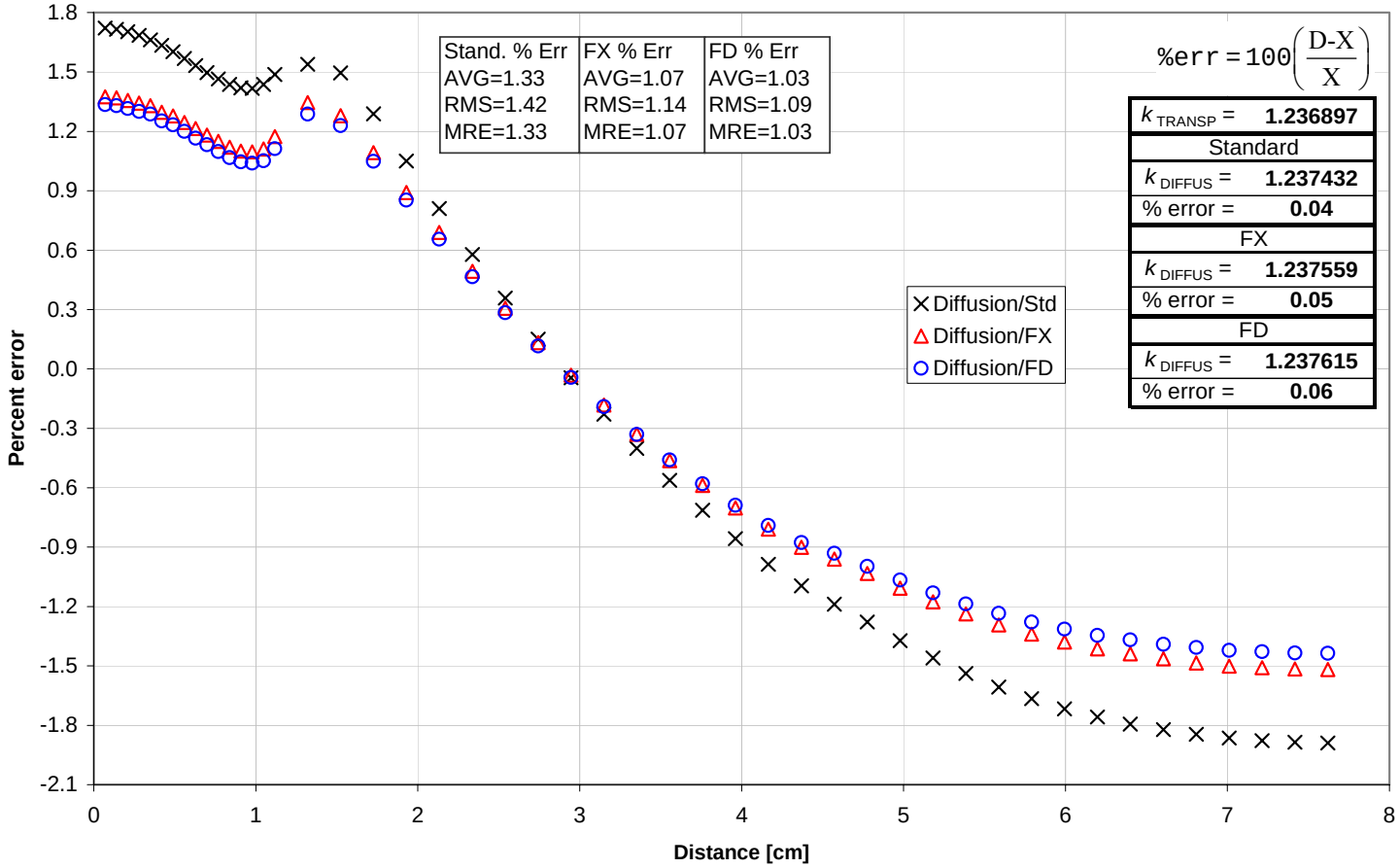

Figure 4.36: Normalized flux percent error, Heterogeneous half-assembly 2, Reflective BCs, group 2 of 4, Diffusion Thy. w/Std, FX, FD.

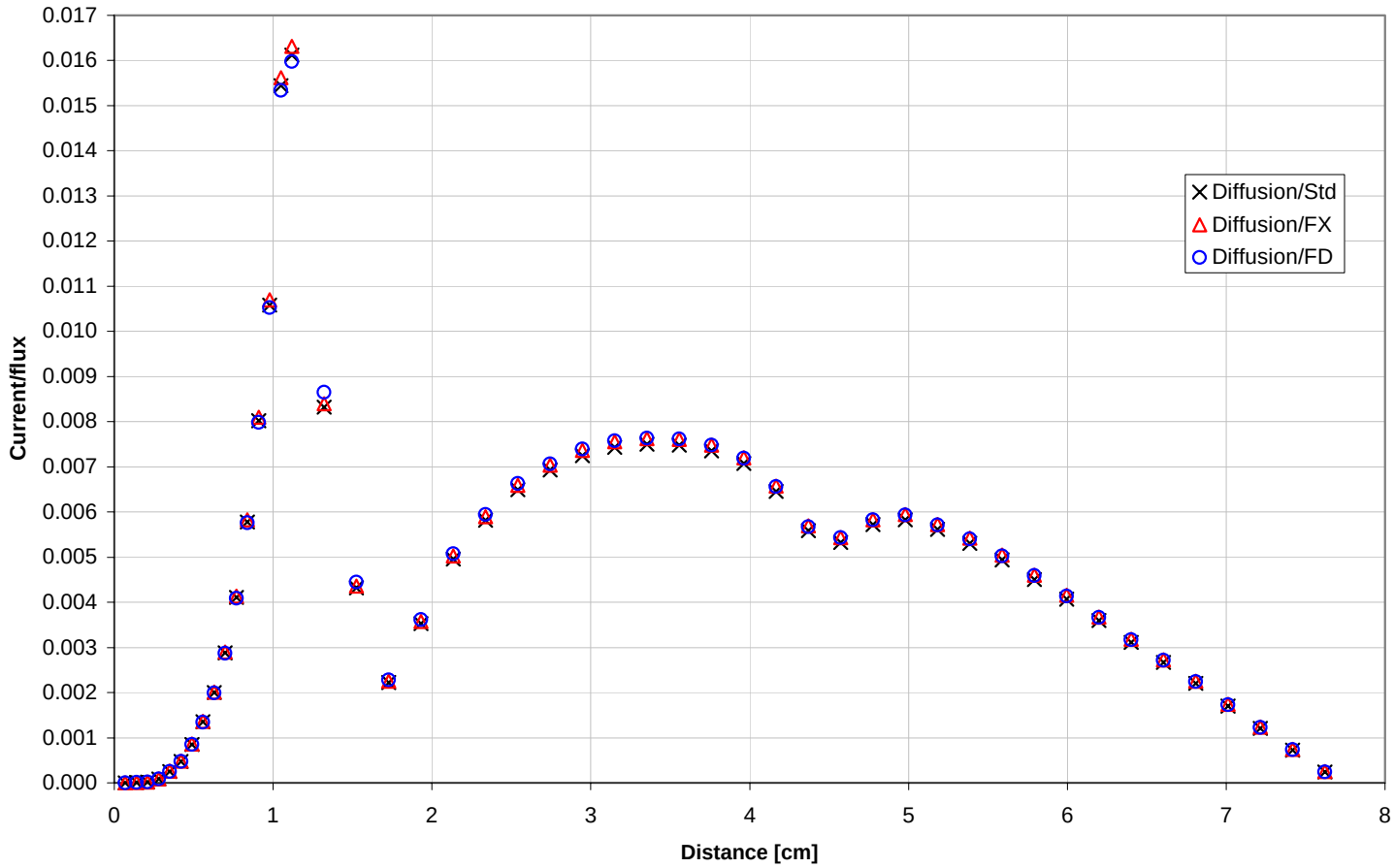

Figure 4.37: Current to flux ratio, Heterogeneous half-assembly 2, Reflective BCs, group 2 of 4, Diffusion Thy. w/Std, FX, FD.

4.2 WHOLE CORES

For the whole-core fine-mesh diffusion calculations (no discontinuity factors), the eigenvalue and error summaries in Table 4.15 and Table 4.16 show that, compared to the Std, the FD reduces the errors in group 1 but worsens them in group 2, and the eigenvalues rank worse for cores 1 and 2 and best for core 3.

Table 4.15: Eigenvalues, Two groups, Heterogeneous cores, Diffusion Theory w/Std, FX, FD.

Core 1			
Transport	Std	FX	FD
1.166131	1.168036	1.168600	1.169037
Core 2			
Transport	Std	FX	FD
0.929130	0.925152	0.925173	0.923461
Core 3			
Transport	Std	FX	FD
0.760879	0.751909	0.752677	0.754904

Table 4.16: Errors, Two Individual groups, Heterogeneous cores, Diffusion Theory w/Std, FX, FD.

	Core 1			Core 2			Core 3		
Egy Grp	Std	FX	FD	Std	FX	FD	Std	FX	FD
1	2.00	1.95	1.82	2.57	2.47	2.13	3.58	3.38	3.35
2	1.08	1.26	1.15	1.62	2.13	2.92	3.02	3.72	5.53
$error_k$	0.16	0.21	0.25	-0.43	-0.43	-0.61	-1.18	-1.08	-0.79

Figure 4.38 through Figure 4.46 show the flux-errors and current/flux ratios for group 1 for all three cores, with each half-core error-plot followed by an error-plot and a ratio-plot in assembly region 1 of that particular core. To see if there are any flux-

limiting benefits, we first look near the core boundary, where the FD method is expected to yield the greatest flux-error reductions compared to the Std diffusion coefficient. However, in group 1, in all 3 full-cores, the flux-error reductions in the water region (data points 1 through 16, 0-1.1176 cm in Figure 4.39, Figure 4.42, and Figure 4.45) is not present, with the FD errors being either equal to or larger than those of the Std and FX, with the exception of about the first three data points in the water region for core 1. We then turn to the graphs of current/flux ratios, shown in Figure 4.40, Figure 4.43, and Figure 4.46, to help explain the flux-error results, and compare it to the single assembly result using vacuum boundary conditions in section 4.1.1. The single assembly in this location of the core is assembly type 2, and we examine the current/flux ratio from two-group results, with vacuum boundary conditions, shown in Figure 4.19 on page 66. One can see that in the water region, near the assembly boundary, the Std and FX current/flux ratios are closer to those of the FD in the whole-core calculations than they are in the single assembly result. Because the FD current/flux ratio is guaranteed not to be non-physically large, other current/flux ratios that are close to it are also less likely to be non-physically large than current/flux ratios that are farther away from it, and this might be causing the Std and FX flux-errors to compare more favorably against the FD in the whole-core than in the single-assembly/vacuum calculation.

Just like Figure 4.38 through Figure 4.46 did for group 1, Figure 4.47 through Figure 4.55 show the flux-errors and current/flux ratios for group 2 for all three cores, with each half-core flux plot followed by a flux-error plot and a current/flux ratio plot in assembly region 1 of that particular core. Contrary to the results in group 1, in group 2

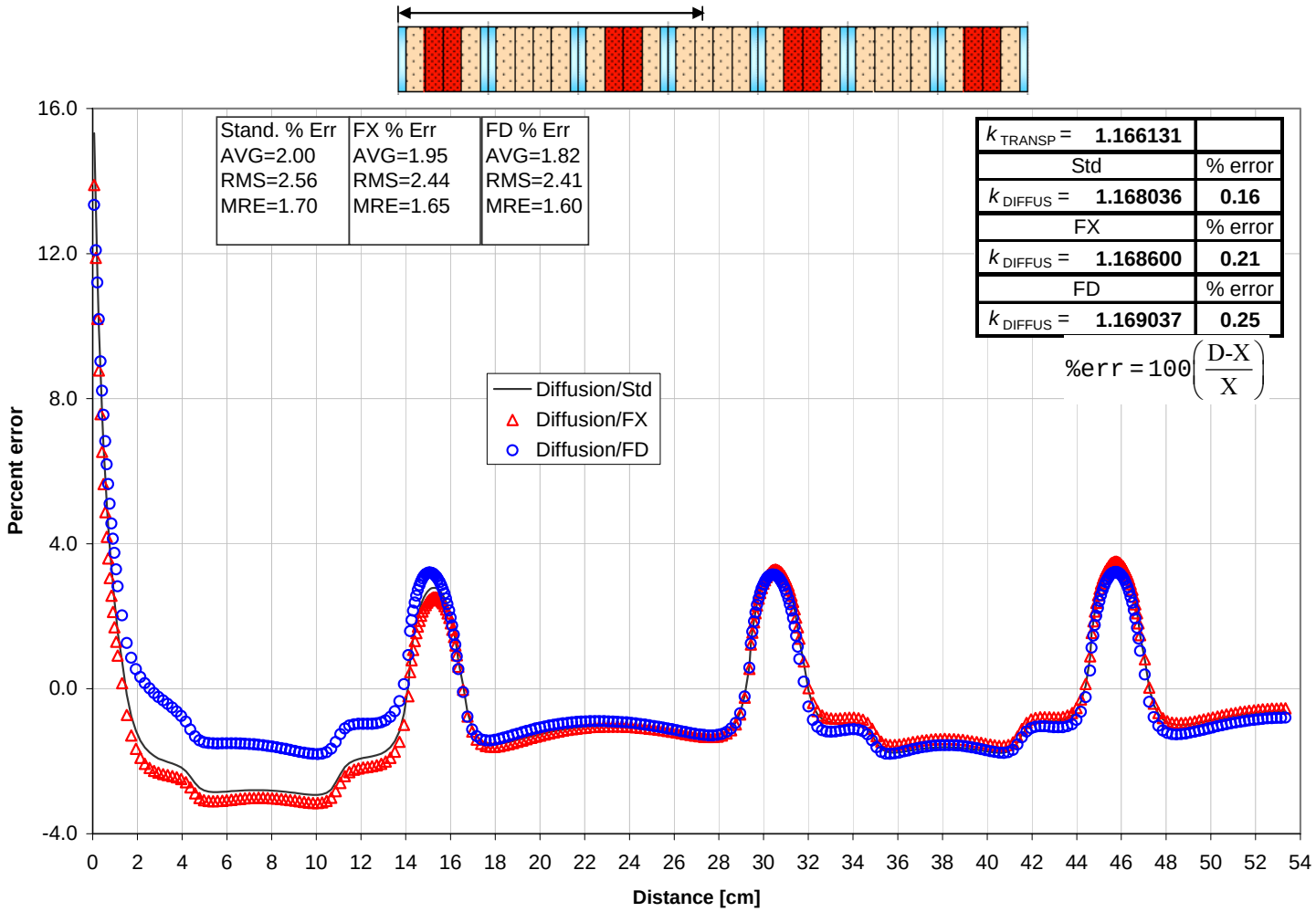

Figure 4.38: Norm'ed flux percent error, heterogen. half-core 1, Group 1 of 2, Diffusion Thy. w/Std, FX, FD.

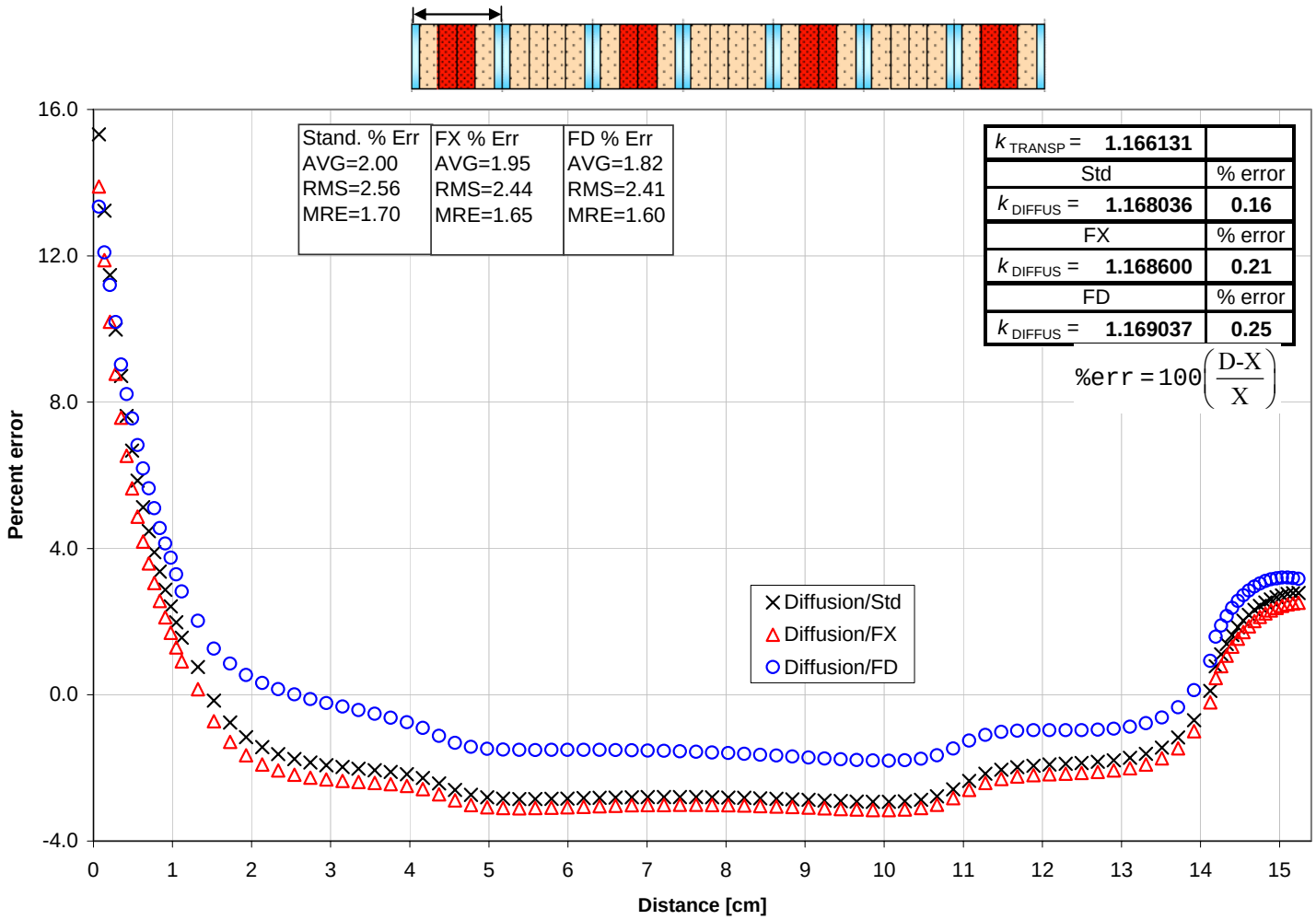

Figure 4.39: Normed flux Perc Err, group 1 of 2, Hetero Assy region 1 (Assy type 2) in-core 1, Diffusion Thy. w/Std, FX, FD.

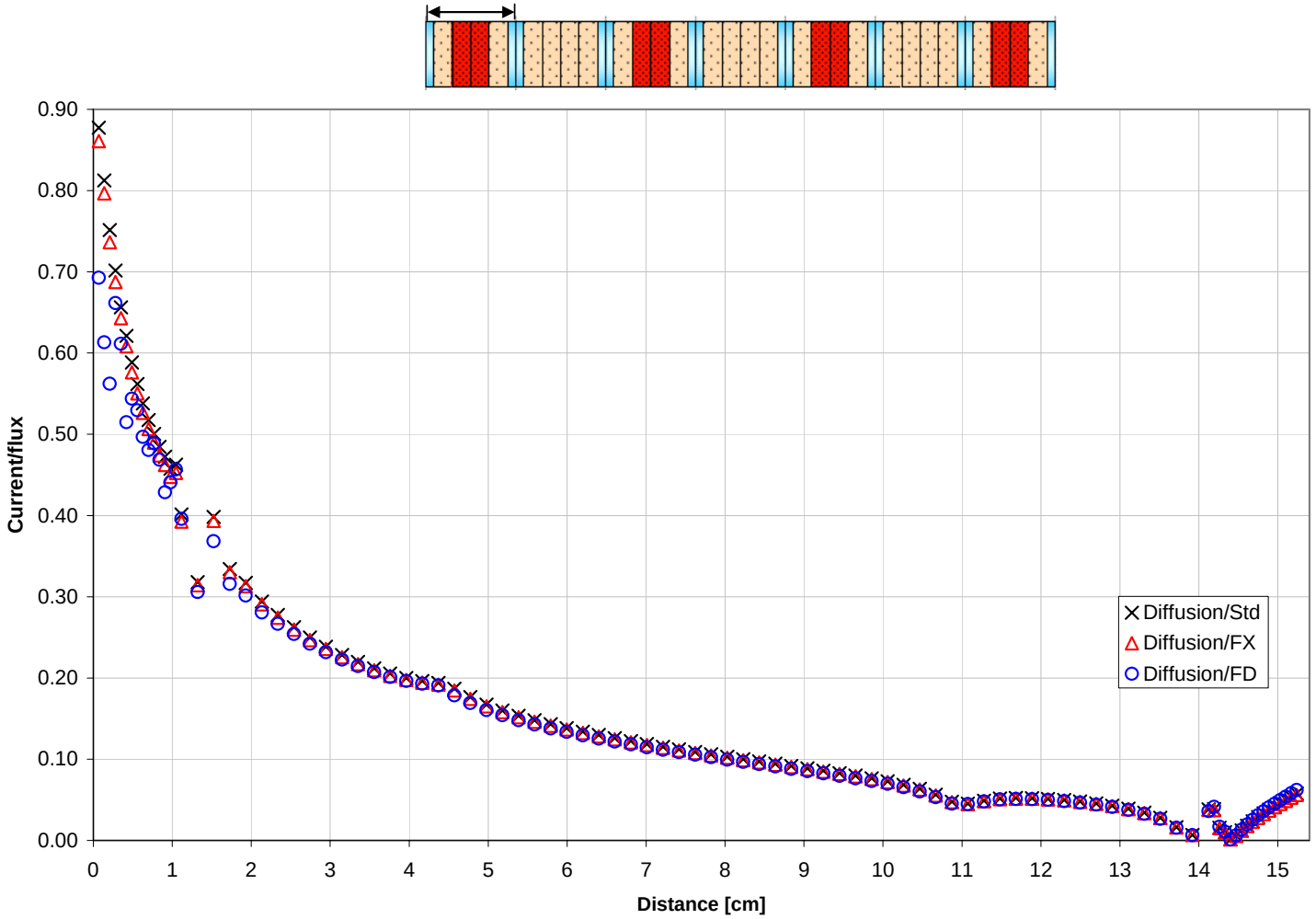

Figure 4.40: Current to flux ratio, group 1 of 2, Hetero Assy region 1 (Assy type 2) in-core 1, Diffusion Thy. w/Std, FX, FD.

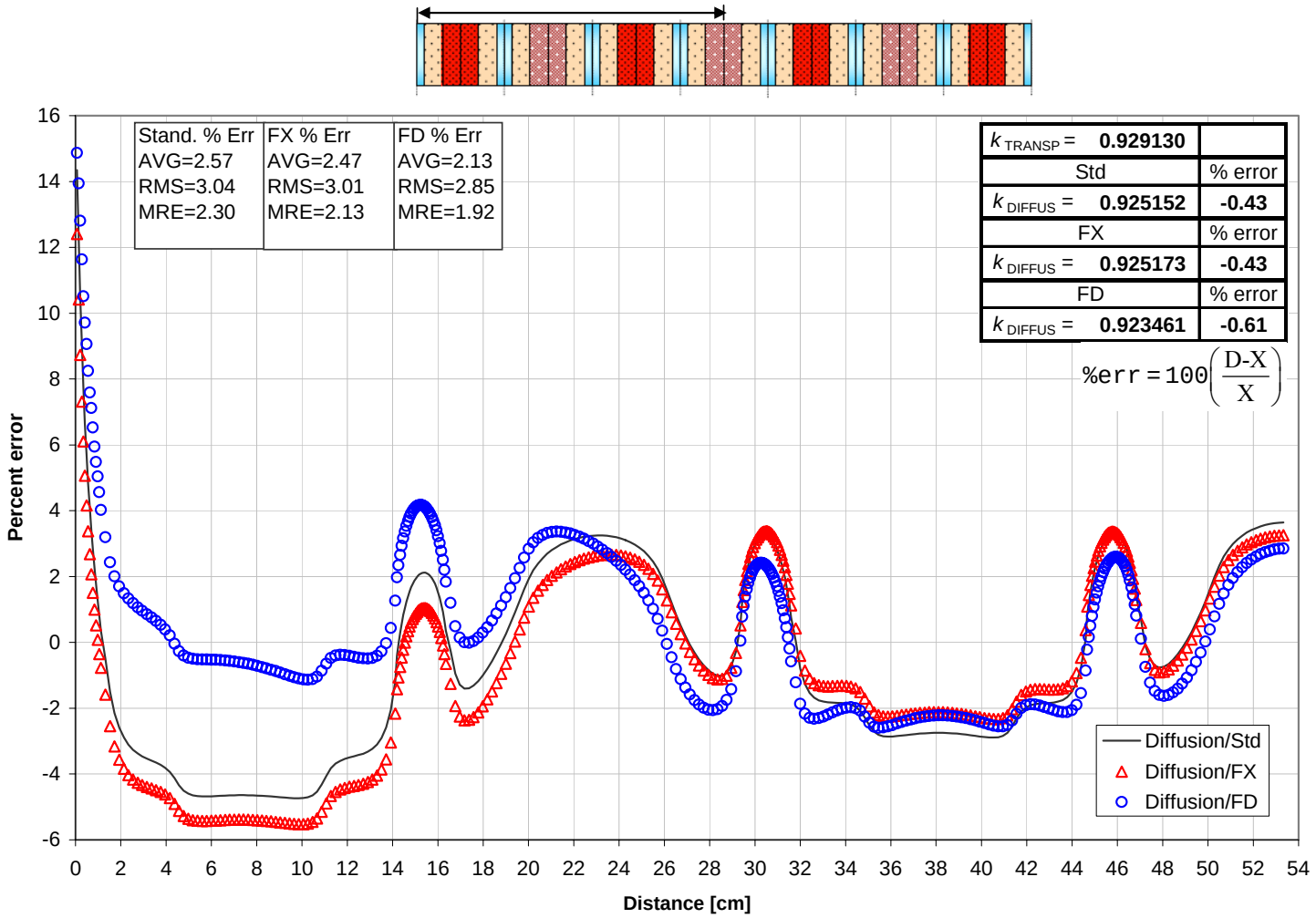

Figure 4.41: Norm'ed flux percent error, heterogen. half-core 2, Group 1 of 2, Diffusion Thy. w/Std, FX, FD.

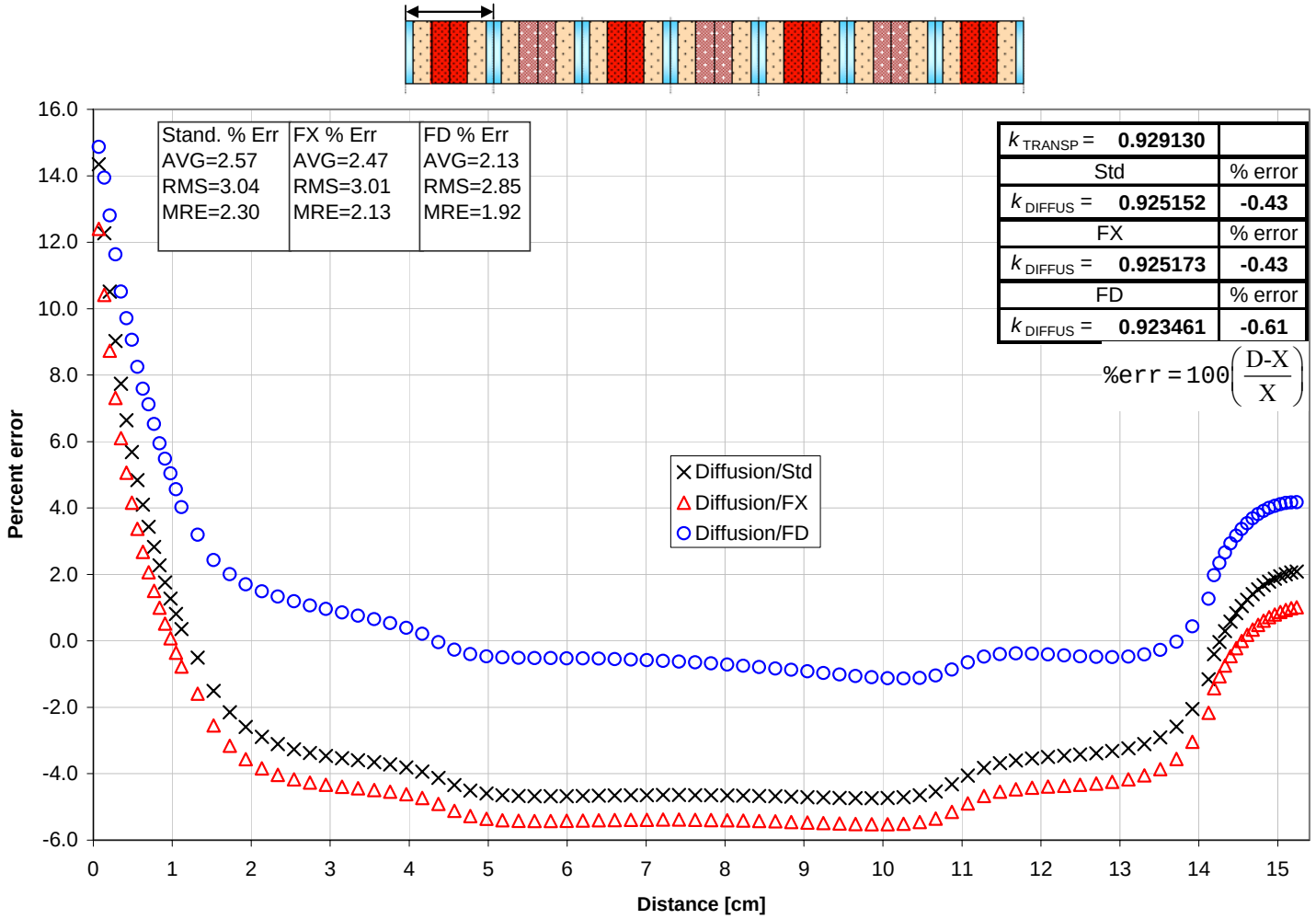

Figure 4.42: Normed flux Perc Err, group 1 of 2, Hetero Assy region 1 (Assy type 2) in-core 2, Diffusion Thy. w/Std, FX, FD.

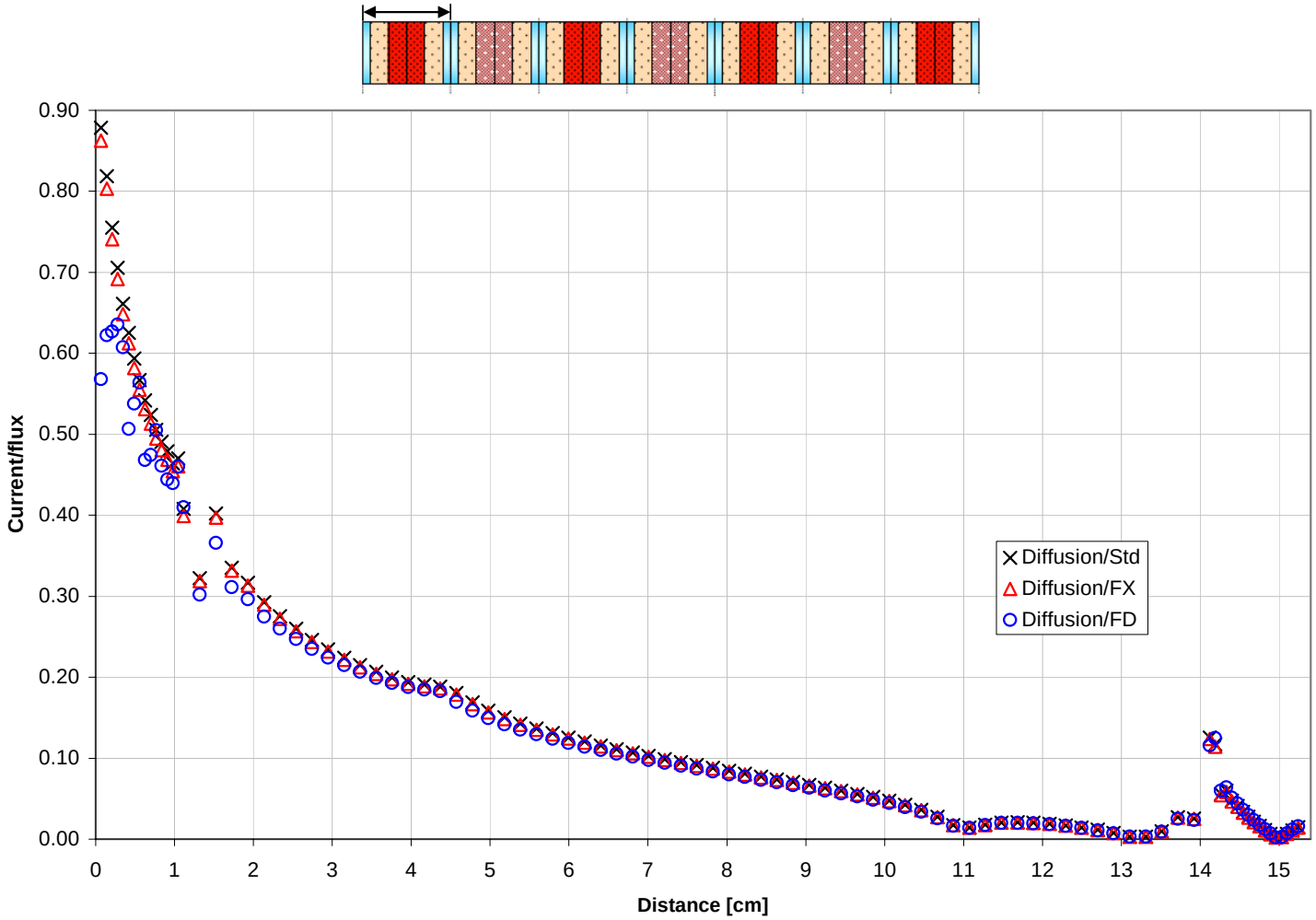

Figure 4.43: Current to flux ratio, group 1 of 2, Hetero Assy region 1 (Assy type 2) in-core 2, Diffusion Thy. w/Std, FX, FD.

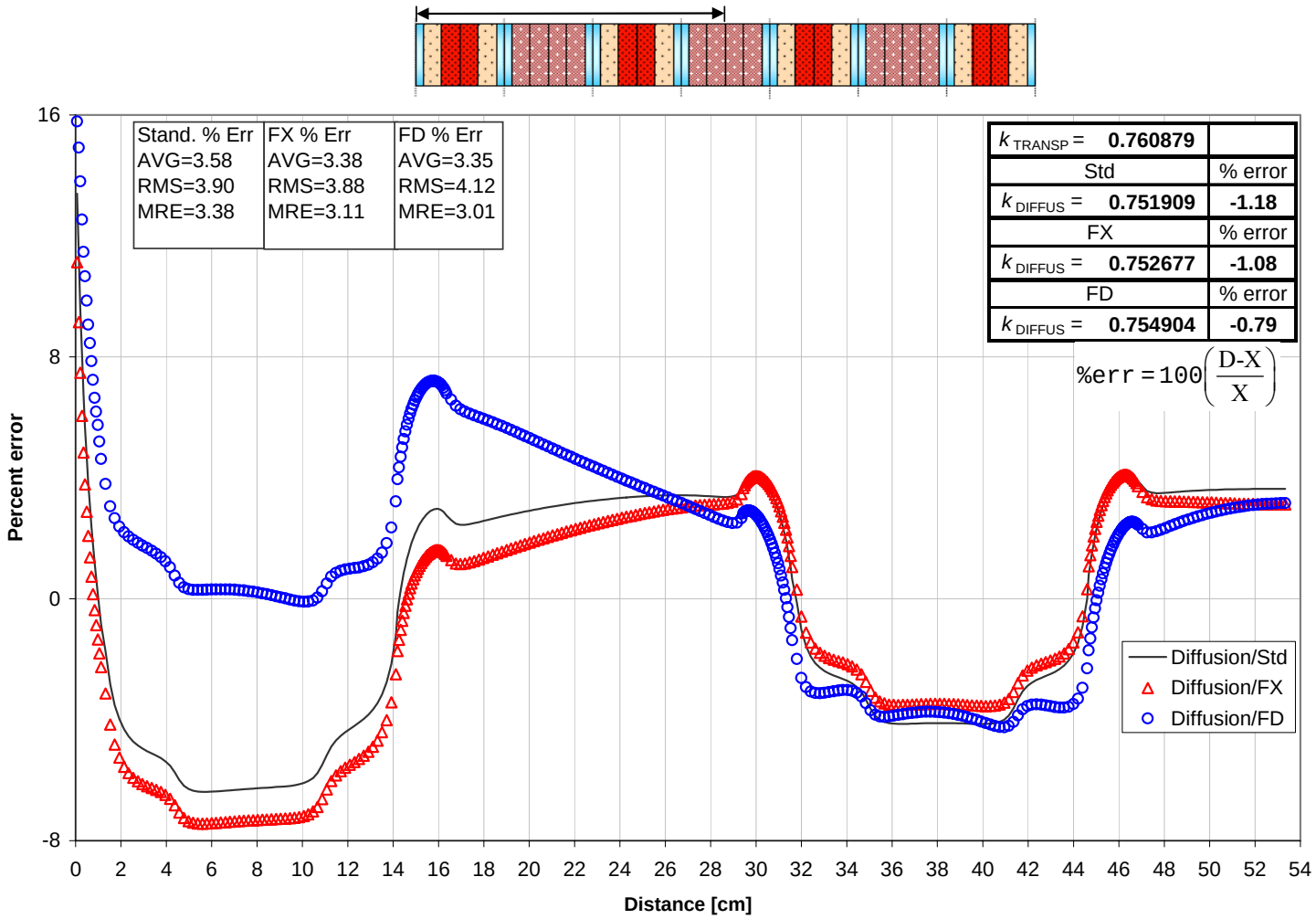

Figure 4.44: Norm'ed flux percent error, heterogen. half-core 3, Group 1 of 2, Diffusion Thy. w/Std, FX, FD.

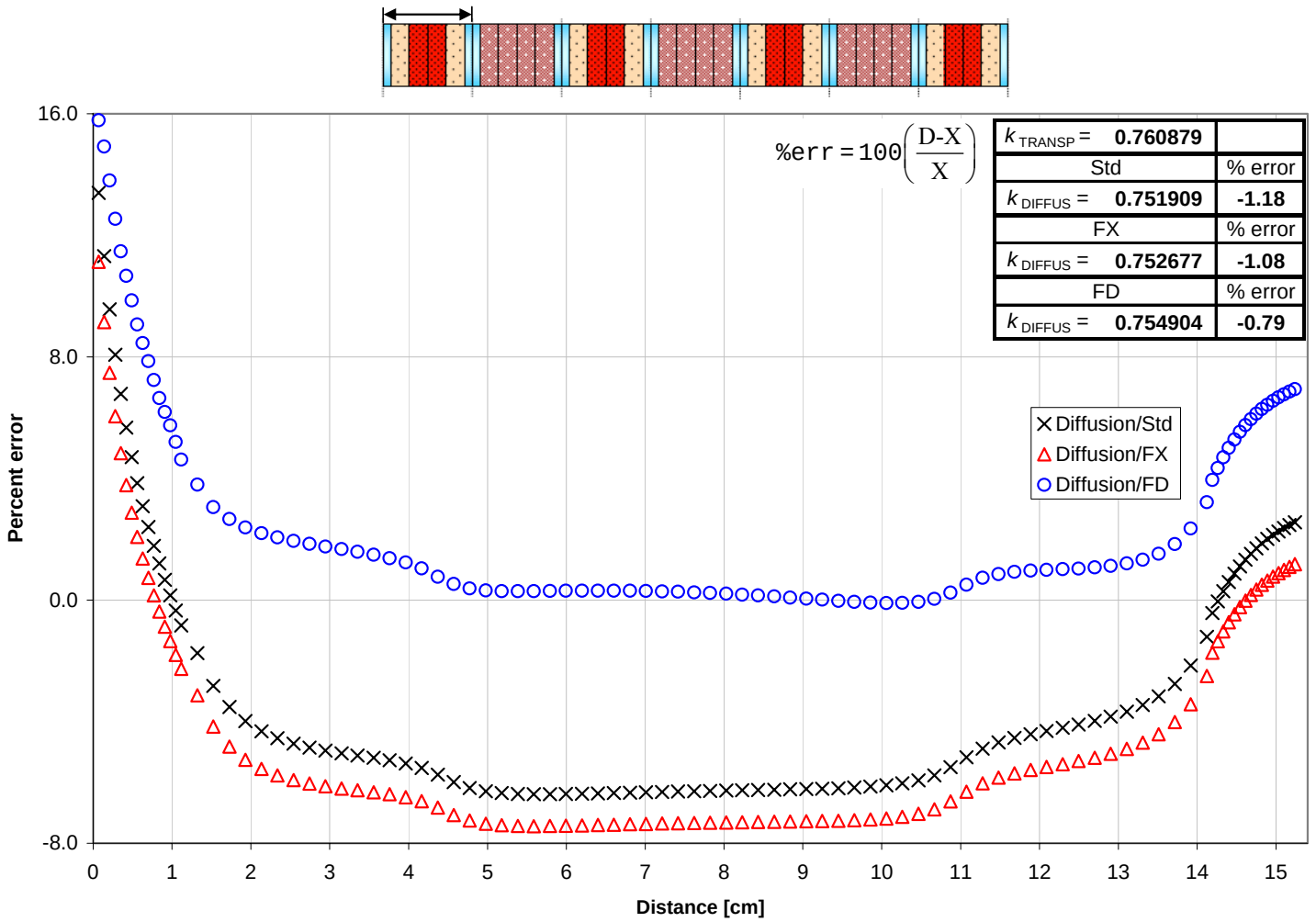

Figure 4.45: Normed flux Perc Err, group 1 of 2, Hetero Assy region 1 (Assy type 2) in-core 3, Diffusion Thy. w/Std, FX, FD.

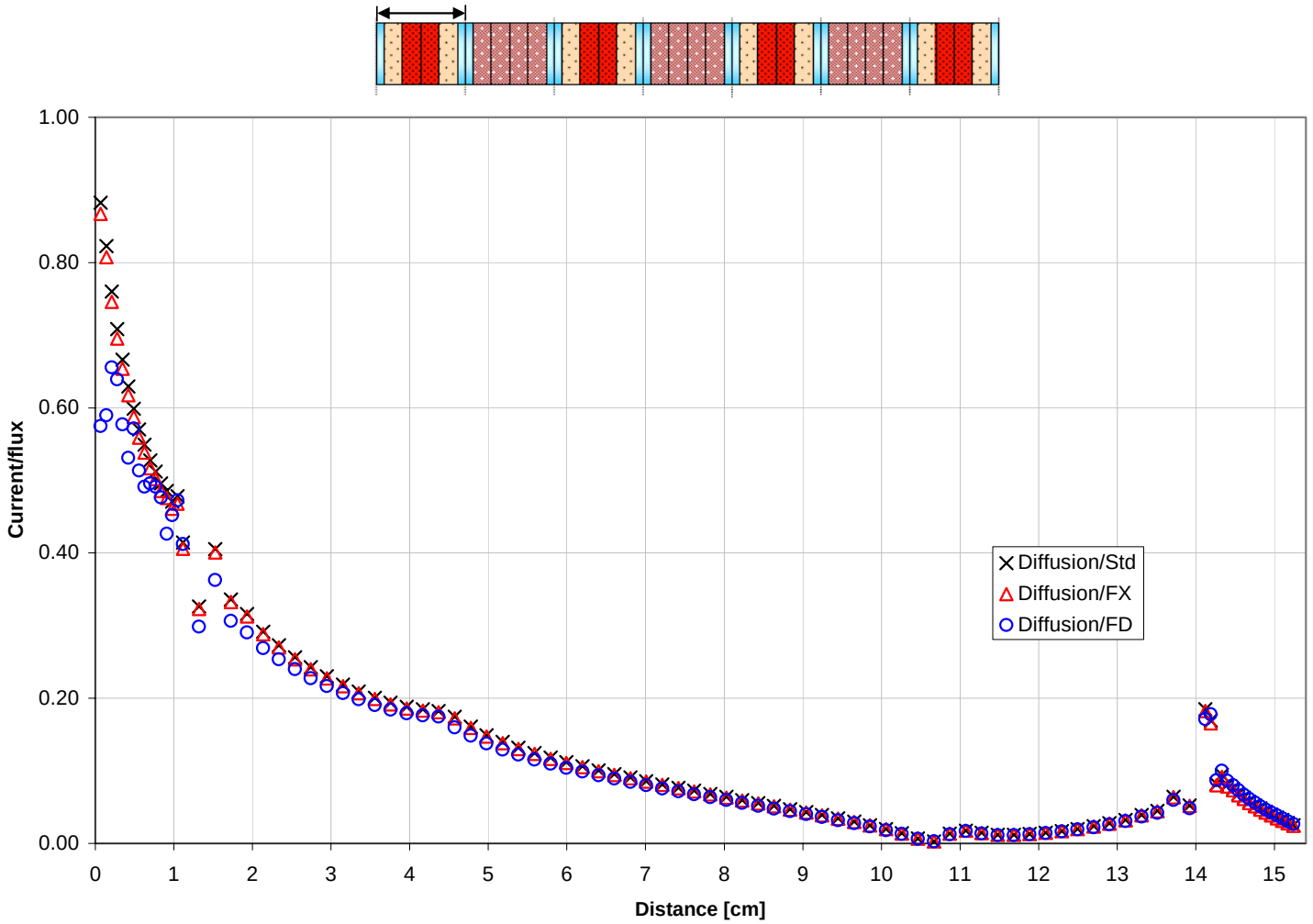

Figure 4.46: Current to flux ratio, group 1 of 2, Hetero Assy region 1 (Assy type 2) in-core 3, Diffusion Thy. w/Std, FX, FD.

the spread between the Std and FD current/flux ratios are about equally large at the boundary of the whole-core as they are at the boundary of the single-assembly/vacuum. Therefore, one might expect the FD method to improve the flux errors in the full-core as they do in the single-assembly, but the flux-error results in Figure 4.48, Figure 4.51, and Figure 4.54 show that they do not. A possible explanation for the lack of improvement using the FD in both energy groups is that even though the Std and FX current/flux ratios are high, caused by a large exiting neutron current, this is not necessarily wrong or non-physical. The definition of the neutron current in Eq. (1.6) states that the magnitude of the current can not be greater than the scalar flux, but it can approach or be equal to it, as would be the case when a large number of neutrons are traveling in one direction. Because the whole-core produces a greater number of neutrons than a single assembly does, the large current/flux ratios produced by the Std and FX diffusion coefficients in the water region of the fine mesh whole-cores are not necessarily too large for this specific problem, and the lower current/flux ratios of the FD might be an indication that the FD diffusion coefficients are too small. Also, even when flux-limiting is a benefit, the other characteristics of FD alluded to in previous subsections also contribute to improving or worsening (in this region worsening) the flux errors.

Despite all of this, the FD diffusion coefficients do slightly reduce flux errors in group 1 outside of regions of large flux gradients, but they slightly increase the errors in group 2. This is consistent with the calculations using single-assemblies with reflective, and to a lesser extent vacuum boundary conditions, in that FD improves results in faster groups more than in thermal. However, the spatial regions in the full-core where FD improves flux-errors do not usually occur in the region of the core where error reductions

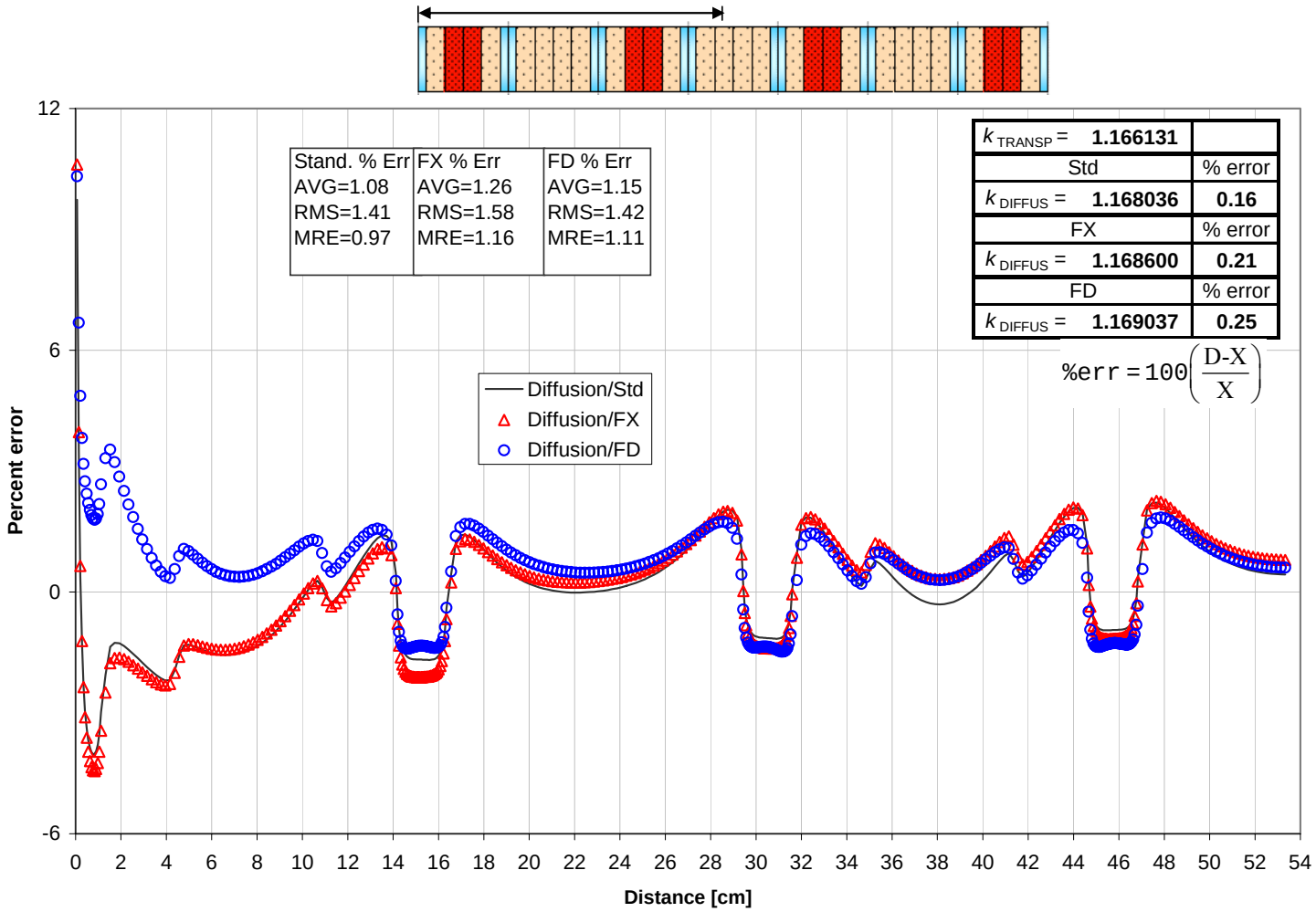

Figure 4.47: Norm'ed flux percent error, heterogen. half-core 1, Group 2 of 2, Diffusion Thy. w/Std, FX, FD.

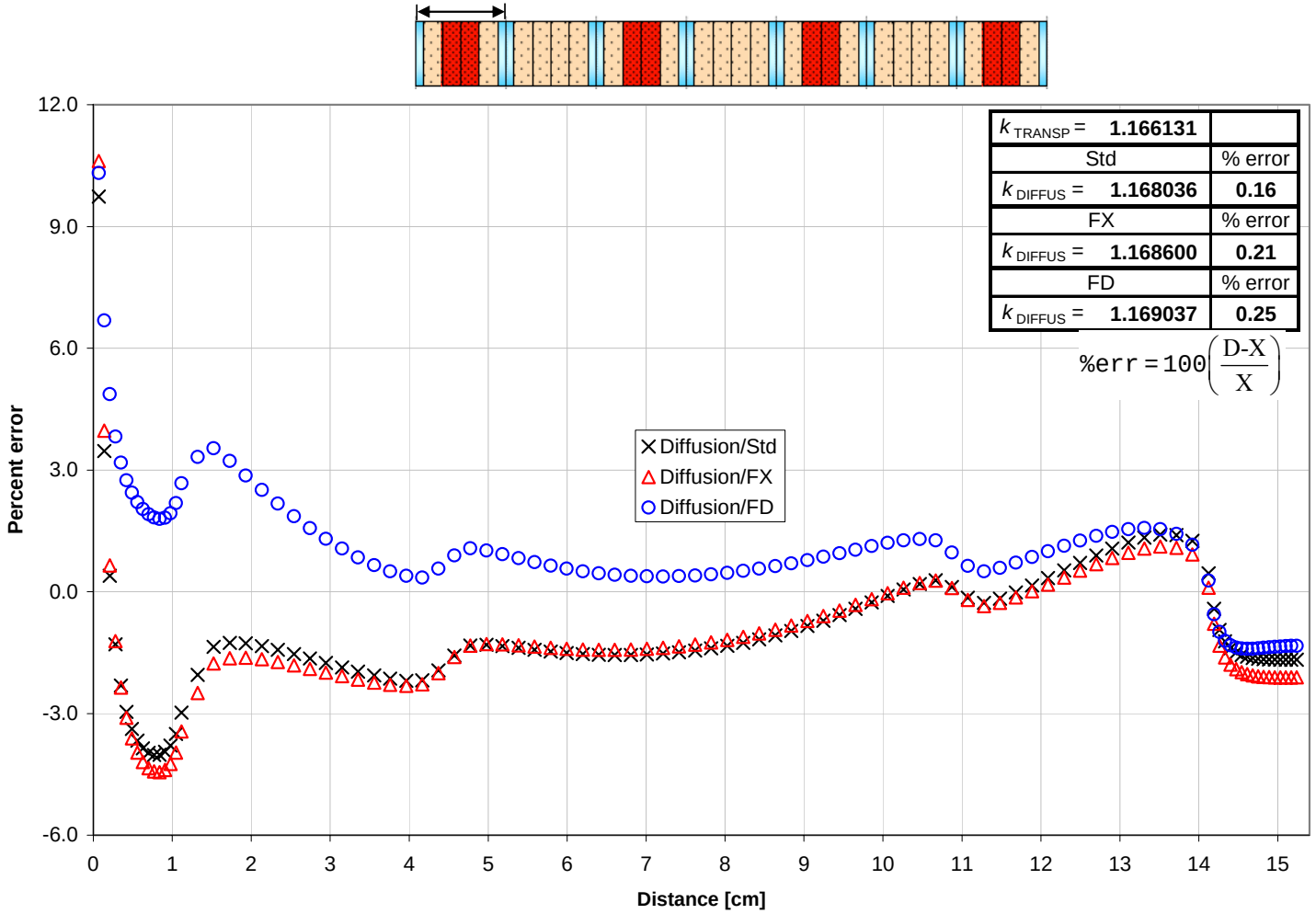

Figure 4.48: Normed flux Perc Err, group 2 of 2, Hetero Assy region 1 (Assy type 2) in-core 1, Diffusion Thy. w/Std, FX, FD.

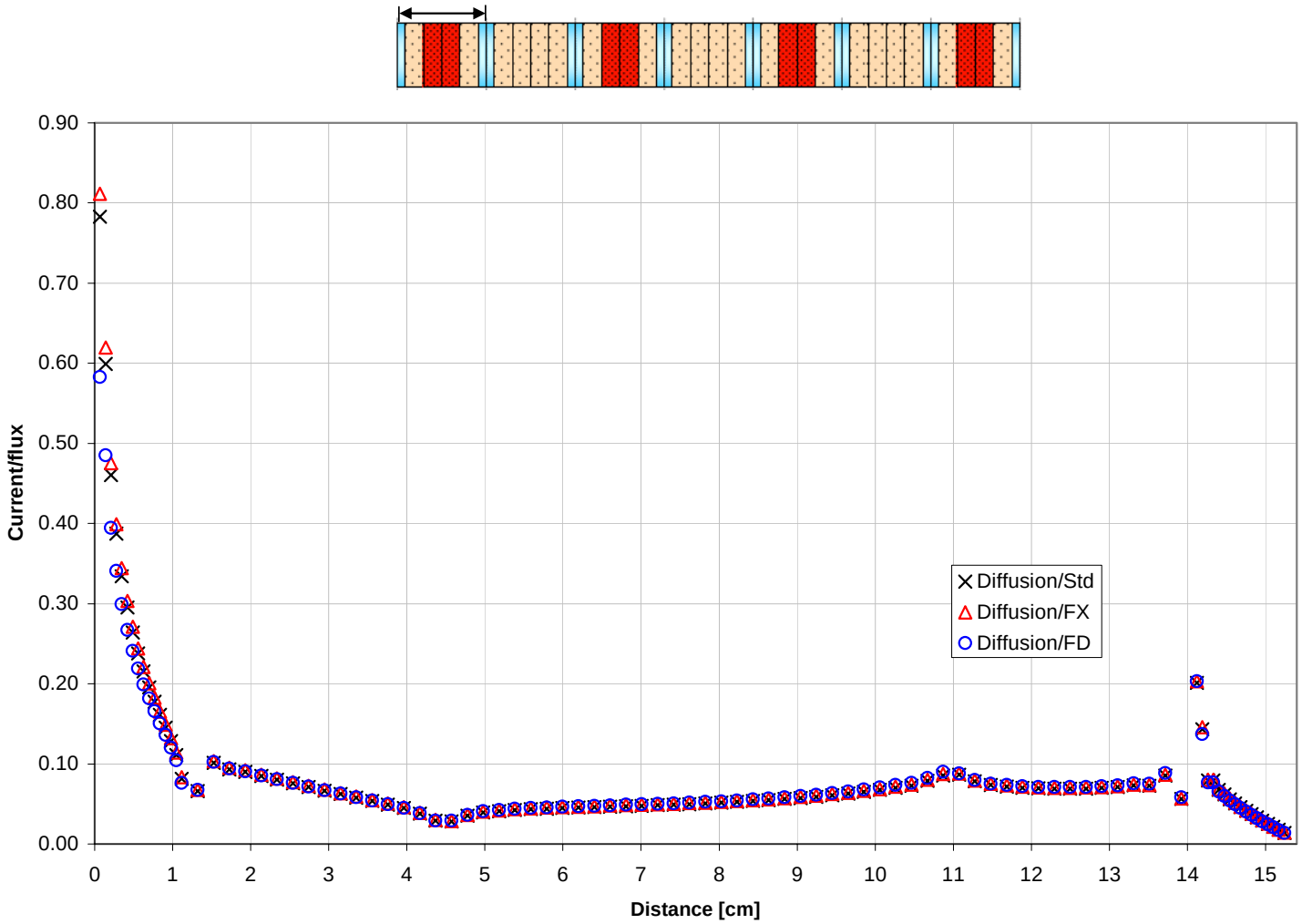

Figure 4.49: Current to flux ratio, group 2 of 2, Hetero Assy region 1 (Assy type 2) in-core 1, Diffusion Thy. w/Std, FX, FD.

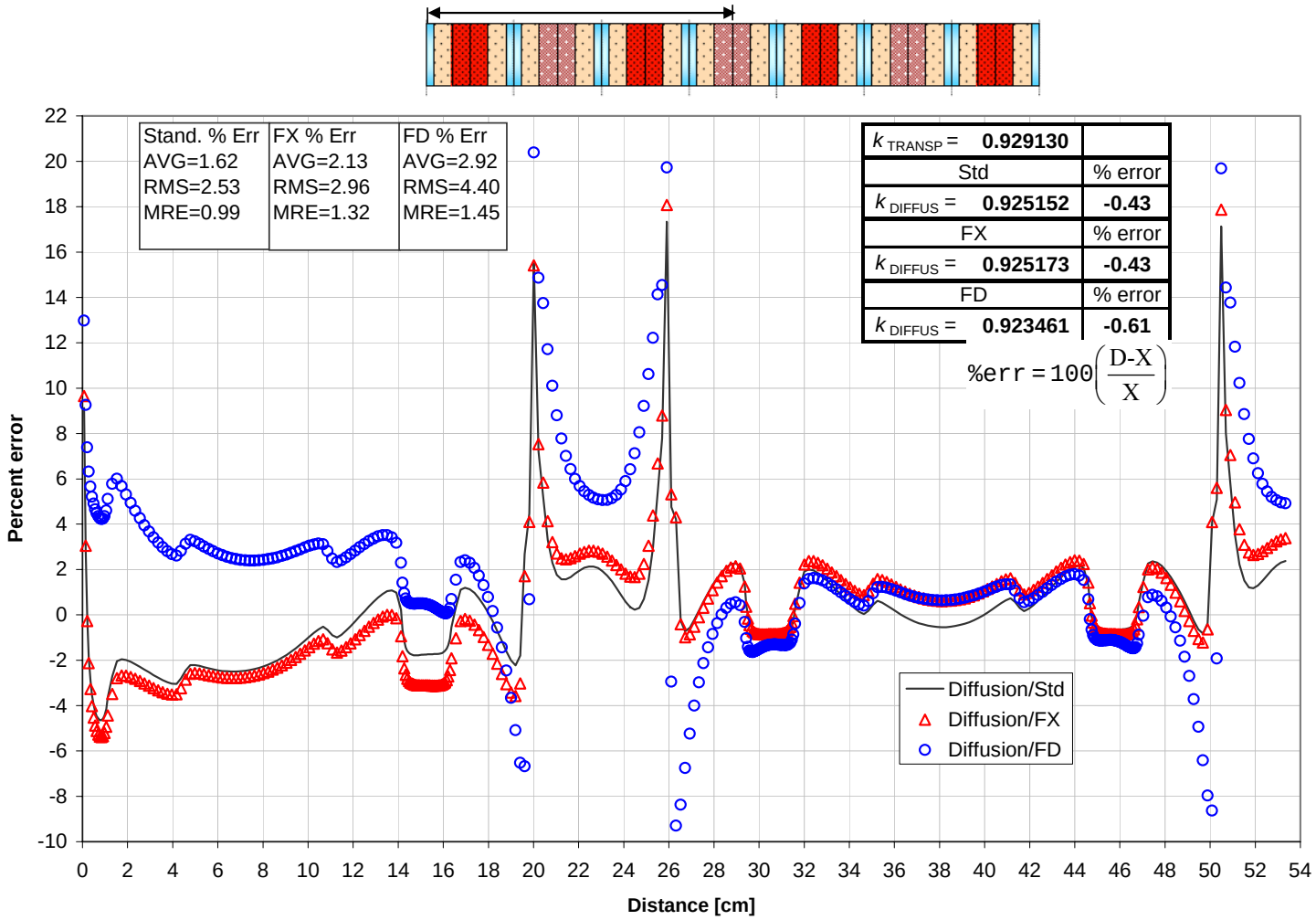

Figure 4.50: Norm'ed flux percent error, heterogen. half-core 2, Group 2 of 2, Diffusion Thy. w/Std, FX, FD.

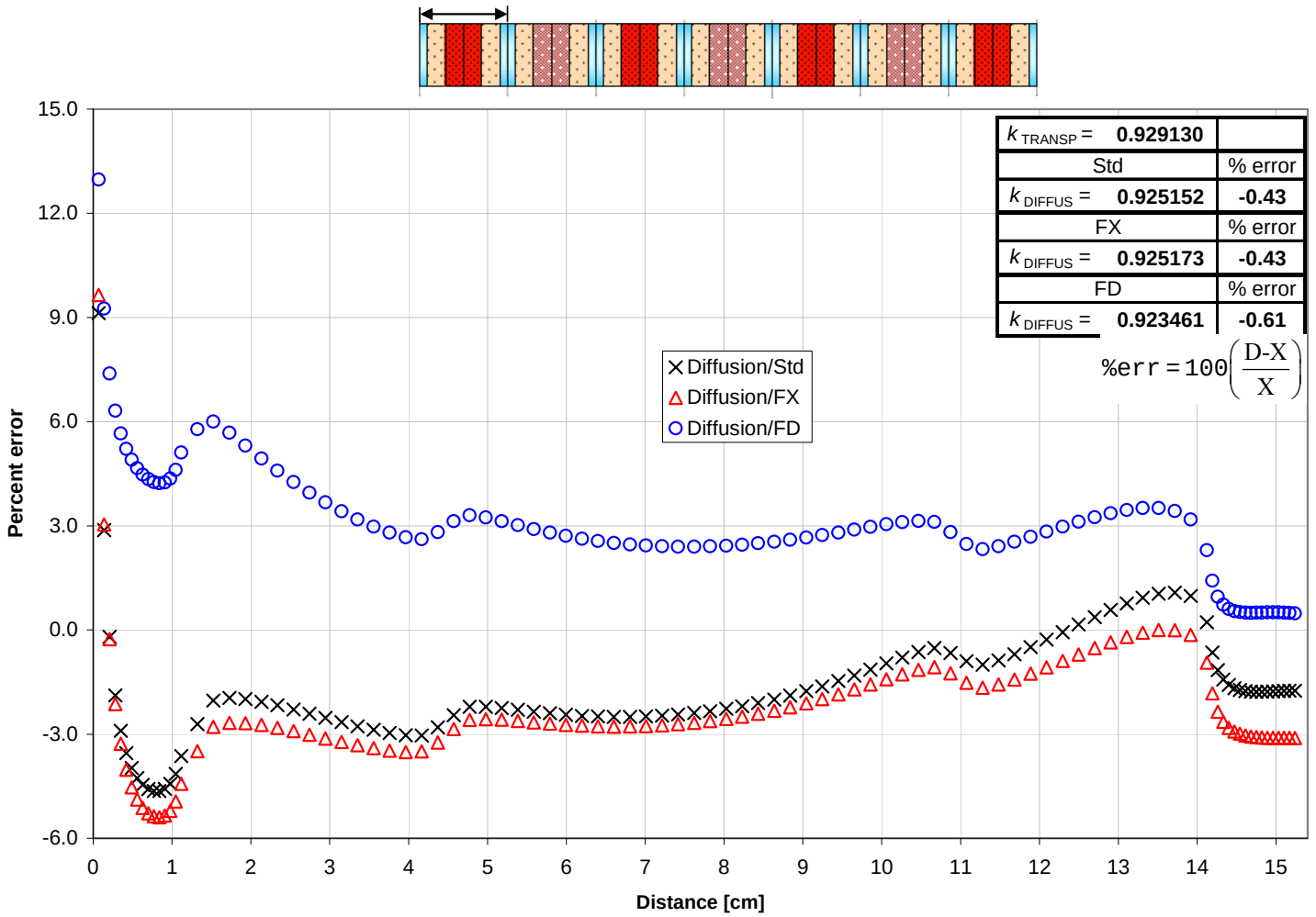

Figure 4.51: Normed flux Perc Err, group 2 of 2, Hetero Assy region 1 (Assy type 2) in-core 2, Diffusion Thy. w/Std, FX, FD.

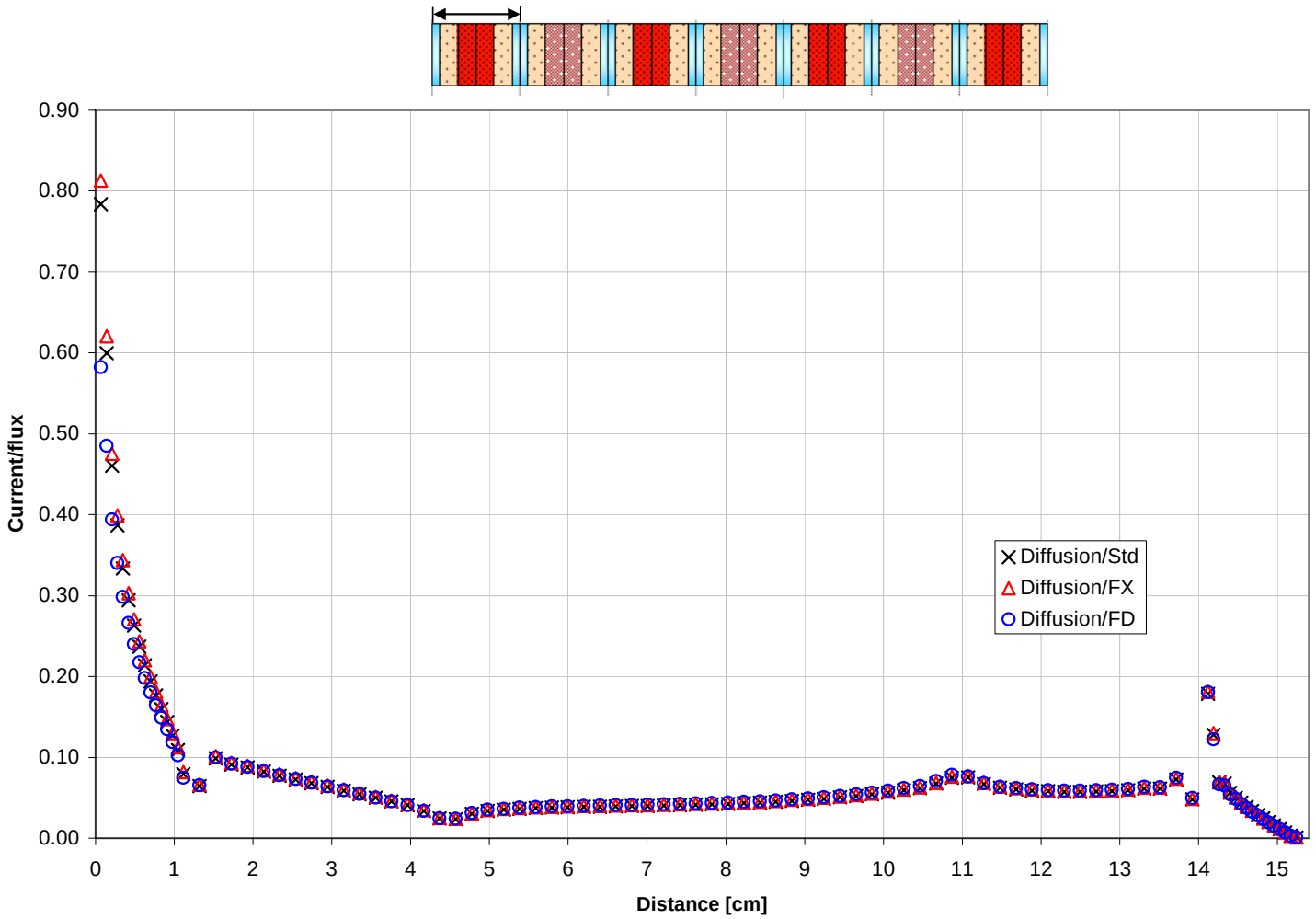

Figure 4.52: Current to flux ratio, group 2 of 2, Hetero Assy region 1 (Assy type 2) in-core 2, Diffusion Thy. w/Std, FX, FD.

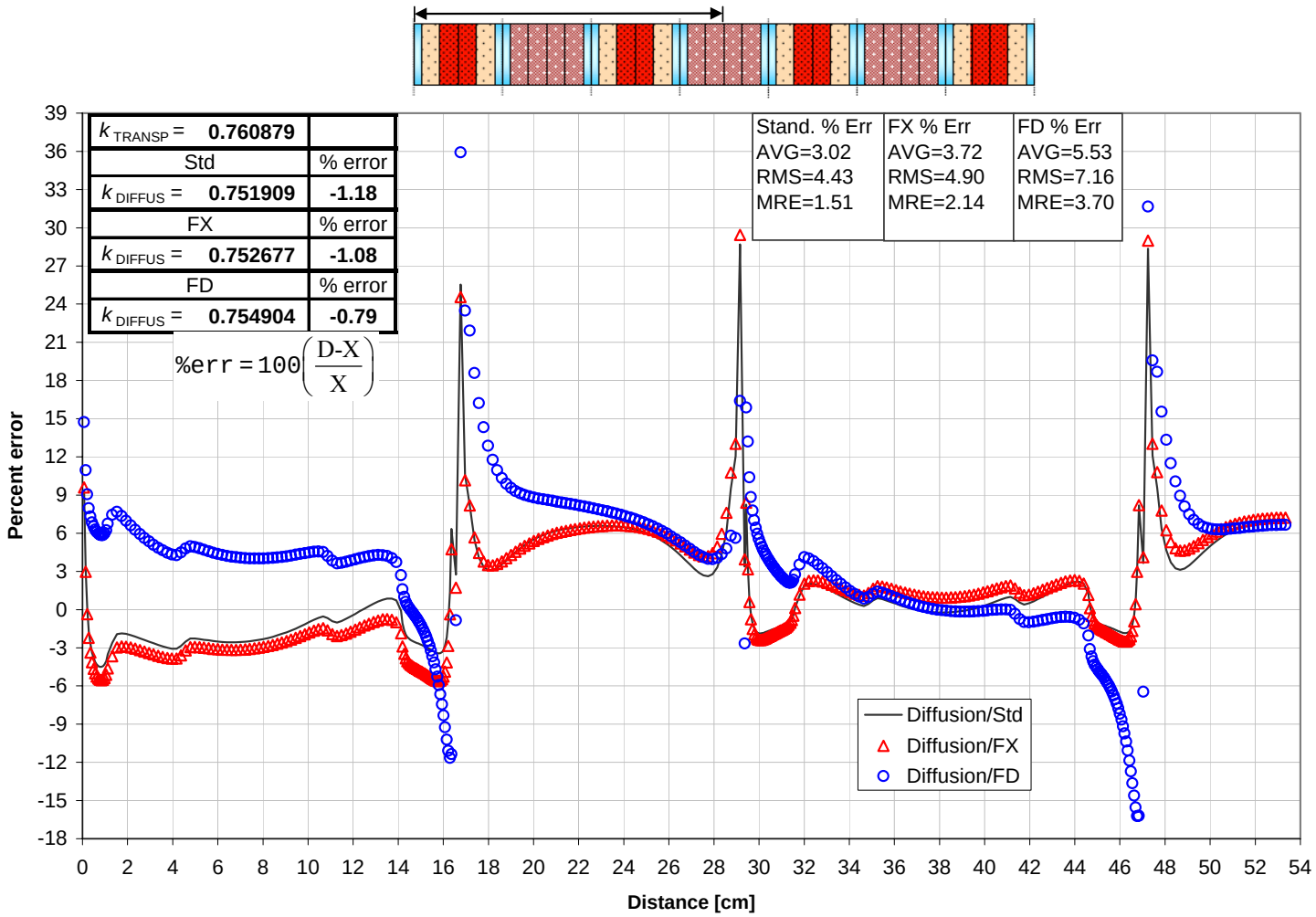

Figure 4.53: Norm'ed flux percent error, heterogen half-core 3, Group 2 of 2, Diffusion Thy. w/Std, FX, FD.

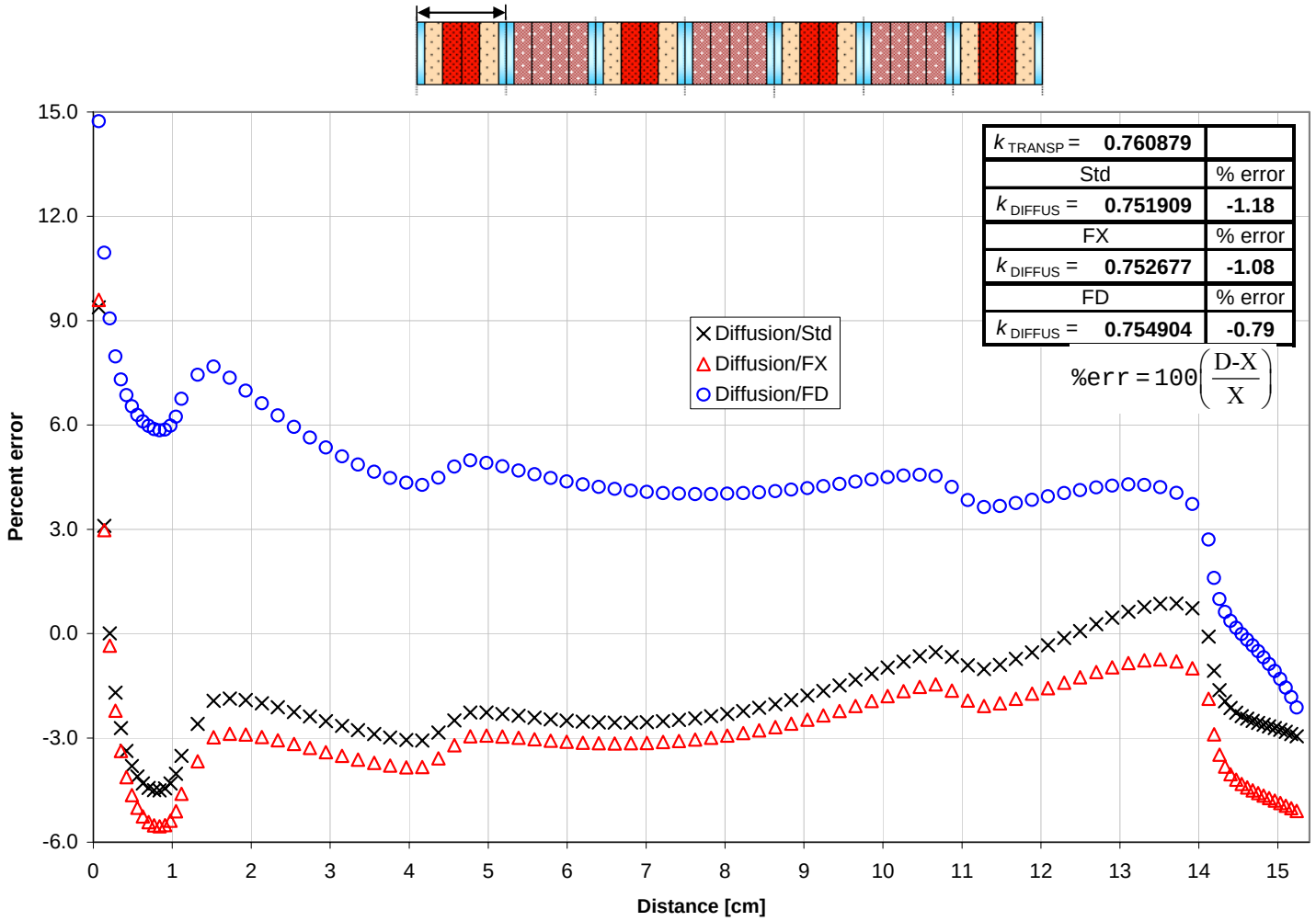

Figure 4.54: Normed flux Perc Err, group 2 of 2, Hetero Assy region 1 (Assy type 2) in-core 3, Diffusion Thy. w/Std, FX, FD.

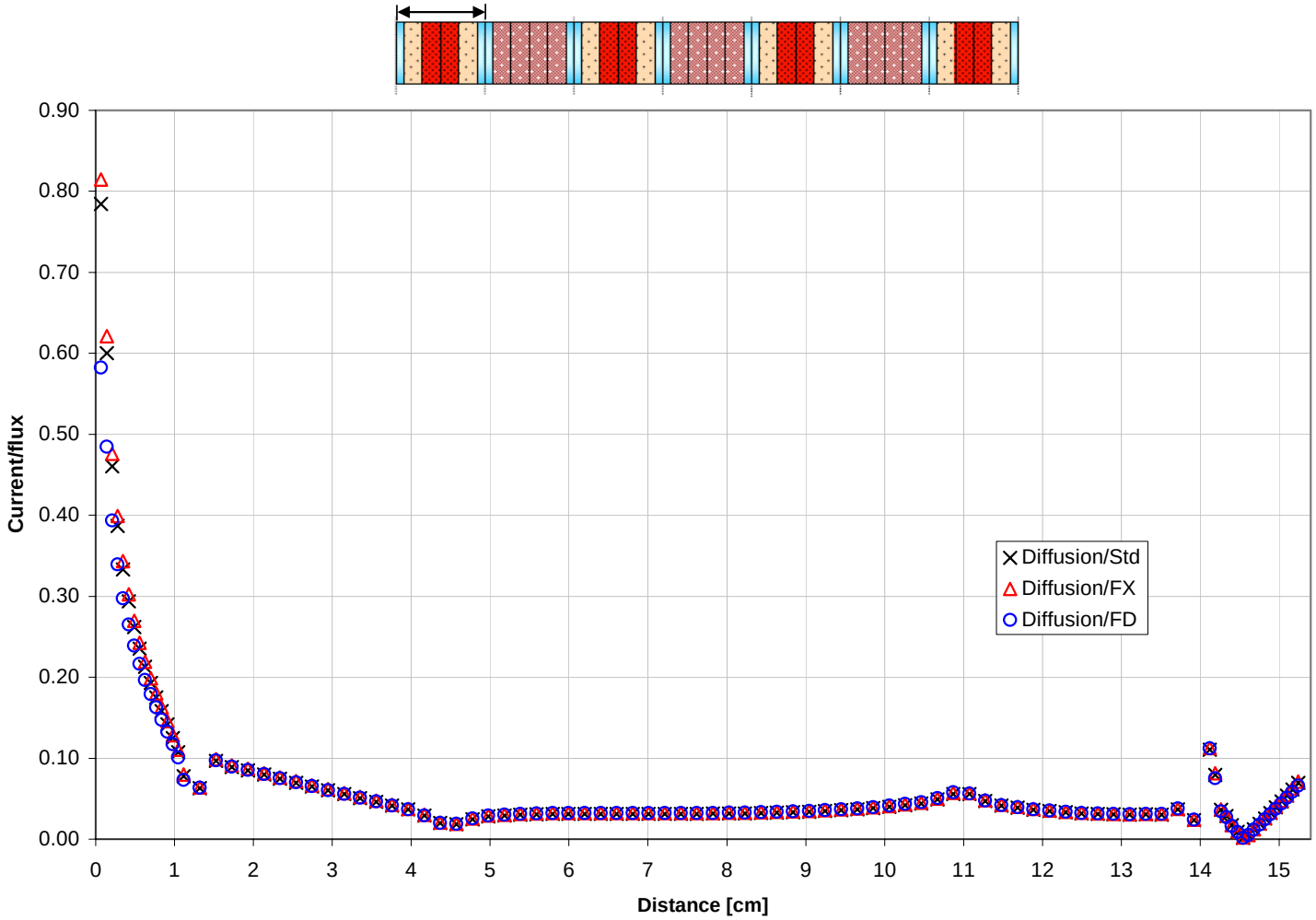

Figure 4.55: Current to flux ratio, group 2 of 2, Hetero Assy region 1 (Assy type 2) in-core 3, Diffusion Thy. w/Std, FX, FD.

are present in the corresponding single-assembly calculation with either reflective or vacuum boundary conditions. For example, in fine-mesh full-core 1, in assembly region 4, which is located near the center of the core and made up of assembly type 1 and shown in detail in Figure 4.56, there is an improvement in flux errors with the FD in the water region which extends slightly into the fuel region (45.7 through 47 cm) and an increase in errors everywhere else. On the other hand, in the single-assembly type 1 calculation with reflective boundary conditions, group 1 of 2, shown in Figure 4.57, the improvement in the water region extending slightly into the fuel region (0.07 through 1.5 cm in the half-assembly calculation) using the FD is barely noticeable, and the FD slightly improves the errors towards the center of the assembly instead of worsening them as in the full-core.

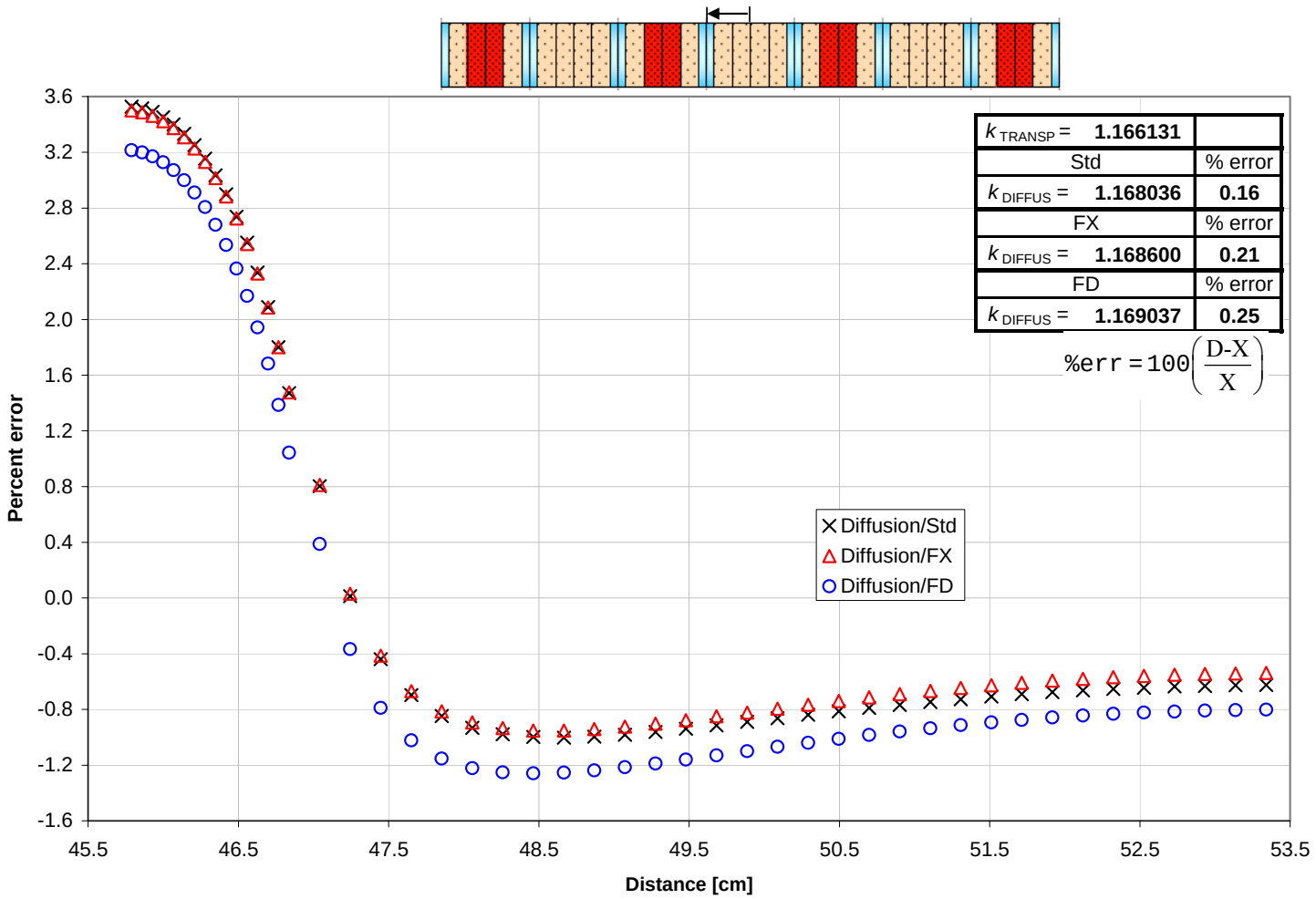

Figure 4.56: Normed flux Perc Err, group 1 of 2, Hetero Assy region 4 (Assy type 1) in-core 1, Diffusion Thy. w/Std, FX, FD.

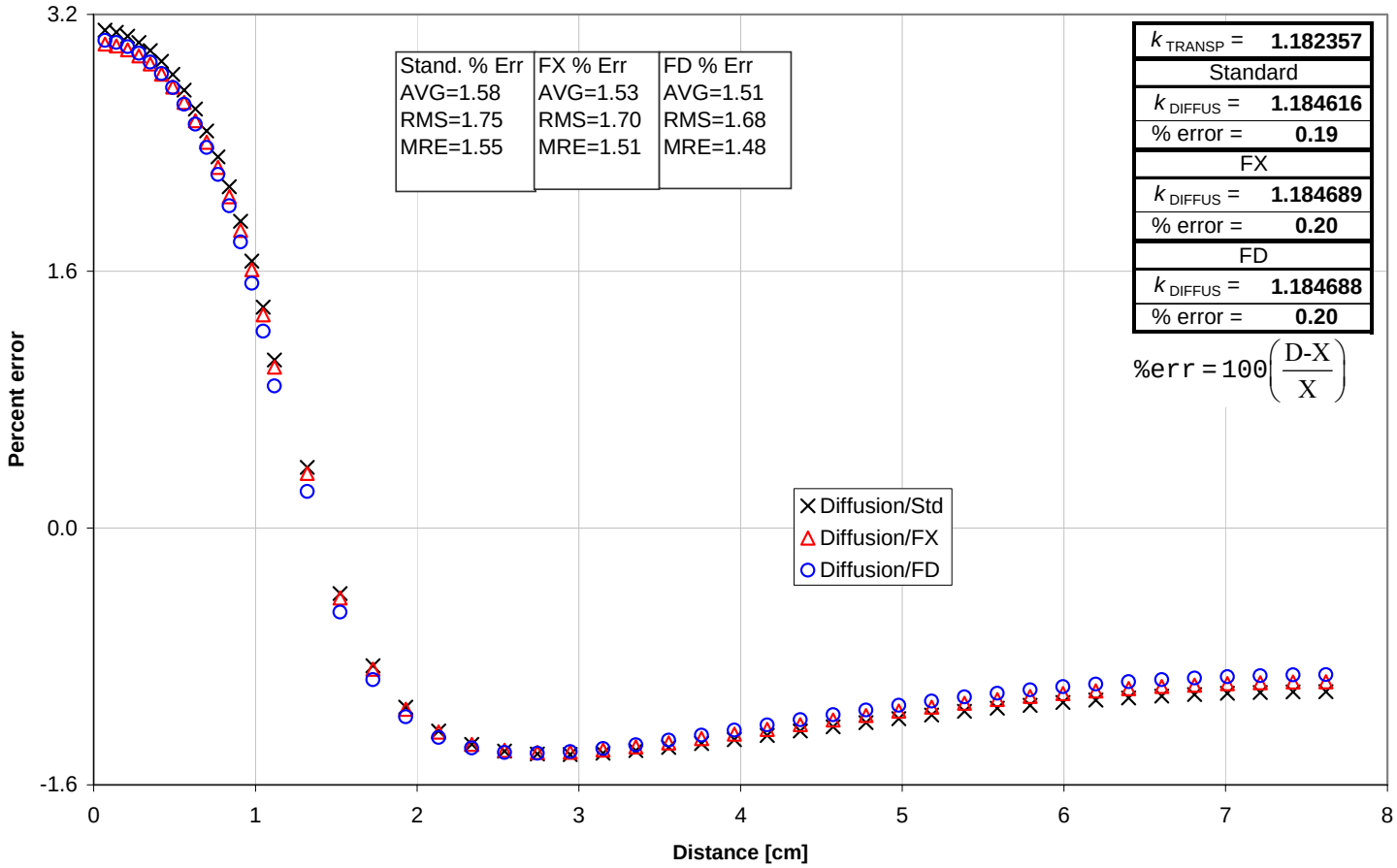

Figure 4.57: Normalized flux percent error, Heterogeneous half-assembly 1, Reflective BCs, group 1 of 2, Diffusion Thy. w/Std, FX, FD.

4.3 COMBINATION OF THE STANDARD AND FLUX-LIMITED DIFFUSION COEFFICIENTS

Based on the results above the FD diffusion coefficients tend to reduce flux-errors in the faster groups and worsen them in the thermal groups. This trend is not as apparent in single assemblies with vacuum boundaries as with reflective boundaries, and the whole-cores. Therefore, it is the latter two types of calculations that have the most to gain by using a combination of the FD in the faster groups and the Std in the thermal groups. The results of these types of calculations are presented in this section. In four-group calculations the FD was used for groups 1 and 2, and the Std was used for groups 3 and 4, and in two-group calculations the FD was used for group 1 and the Std was used for group 2. In the results below, the method that uses these combinations of diffusion coefficients is noted as FDSt.

The four-group single assembly/reflective boundary eigenvalue results are shown in Table 4.17, and the flux-error results in Table 4.18. When a result under the FDSt column in Table 4.18 is bold that result is the lowest error, but compared only against the Std method. The results in Table 4.18 indicate that the combination FDSt method has lower errors than the Std method in the two fast groups for all assembly types, and in groups 3 and 4 improves the errors in some assembly types and worsens them in others. Overall, the FDSt method is the most accurate because the amount of improvement in the fast groups is greater than the amount of worsening in the thermal groups. For example, in assembly type 1, the FDSt reduces the flux-errors by 0.28 percentage points in group 1 and 0.14 percentage points in group 2, but increases them only less than 0.01 points in

group 3 and 0.03 points in group 4. The results in the FD column, based on results using the FD for all energy groups, reduce errors slightly more than the FDSt does in the fast groups, but in the thermal groups worsen the errors more than the FDSt does. Overall, the combination of diffusion coefficients in the FDSt method is the most accurate.

Table 4.17: Eigenvalues, Four groups, Heterogeneous half-assemblies, Reflective BCs, Diffusion Thy. w/Std, FD, FDSt.

Assy 1				Assy 2			
Transport	Std	FD	FDSt	Transport	Std	FD	FDSt
1.182742	1.183262	1.183226	1.183212	1.236897	1.237432	1.237615	1.237400
Assy 3				Assy 4			
Transport	Std	FD	FDSt	Transport	Std	FD	FDSt
0.608375	0.604507	0.596936	0.604540	0.322793	0.327468	0.328404	0.327620

Table 4.18: Errors, Four Individual groups, Heterogeneous half-assemblies, Reflective BCs, Diffusion Thy. w/Std, FD, FDSt.

	Assy 1			Assy 2		
Egy Grp	Std	FD	FDSt	Std	FD	FDSt
1	3.08	2.78	**2.80**	3.33	2.98	**3.02**
2	0.99	0.83	**0.85**	1.33	1.03	**1.05**
3	0.84	0.95	0.84	0.85	0.92	**0.84**
4	1.47	1.78	1.50	1.47	1.87	1.52
$error_k$	0.04	0.04	**0.04**	0.04	0.06	**0.04**
	Assy 3			Assy 4		
Egy Grp	Std	FD	FDSt	Std	FD	FDSt
1	2.86	2.80	**2.75**	3.30	2.97	**2.99**
2	0.72	0.76	**0.70**	1.17	0.98	**0.99**
3	1.62	1.98	**1.62**	1.48	1.85	1.49
4	2.36	4.55	**2.36**	8.00	13.34	8.11
$error_k$	-0.64	-1.88	**-0.63**	1.45	1.74	1.50

Similar conclusions can be drawn from the results of the two-group single-assembly calculations shown in Table 4.19 and Table 4.20. The FDSt combination method reduces the flux-errors in the fast group for all assembly types, while it slightly worsens them in the thermal group. The margin of improvement is slightly larger than the margin of worsening, although not by much. There are fewer energy groups in the two-group calculations for the linearly anisotropic scattering characteristic of the FDSt to take advantage of. The FD reduces flux-errors slightly more than the FDSt does in the fast group, but worsens them more in the thermal group, especially in assembly types three and four.

Table 4.19: Eigenvalues, Two groups, Heterogeneous half-assemblies, Reflective BCs, Diffusion Thy. w/Std, FD, FDSt.

Assy 1				Assy 2			
Transport	Std	FD	FDSt	Transport	Std	FD	FDSt
1.182357	1.184616	1.184688	1.184588	1.236606	1.238704	1.238966	1.238697
Assy 3				Assy 4			
Transport	Std	FD	FDSt	Transport	Std	FD	FDSt
0.608448	0.605303	0.598567	0.605401	0.323357	0.327861	0.328567	0.327896

Table 4.20: Errors, Two Individual groups, half-assemblies, Reflective BCs, Diffusion Thy. w/Std, FX, FD, and FDSt.

	Assy 1			Assy 2		
Egy Grp	Std	FD	FDSt	Std	FD	FDSt
1	1.58	1.51	**1.53**	1.71	1.63	**1.66**
2	0.86	1.09	0.88	0.83	1.06	0.84
$error_k$	0.19	0.20	**0.19**	0.17	0.19	**0.17**
	Assy 3			Assy 4		
Egy Grp	Std	FD	FDSt	Std	FD	FDSt
1	1.75	1.78	**1.73**	1.56	1.51	**1.51**
2	1.98	4.07	**1.96**	5.31	10.06	5.35
$error_k$	-0.52	-1.62	**-0.50**	1.39	1.61	1.40

According to the full-core results in Table 4.21 and Table 4.22 the FDSt improves flux-errors in group 1, and also in group 2, and the FD by itself provides a slightly larger error reduction than the FDSt in the fast group, but increases errors in the thermal group. The single anomalous result in the full-core calculations, and the entire set of results using combinations of diffusion coefficients, is the result from core-type three in Table 4.22, where the FDSt doesn't improve over the Std in either group 1 or 2. This core configuration, containing the all-gadolinium assembly-type four, is the most difficult for any type of diffusion theory to manage, and might invalidate one method's assumptions more than another's.

Table 4.21: Eigenvalues, Two groups, Heterogeneous cores, Diffusion Theory w/Std, FD, FDSt.

Core 1			
Transport	Std	FD	FDSt
1.166131	1.168036	1.169037	1.168924
Core 2			
Transport	Std	FD	FDSt
0.929130	0.925152	0.923461	0.926255
Core 3			
Transport	Std	FD	FDSt
0.760879	0.751909	0.754904	0.752900

Table 4.22: Errors, Two Individual groups, Heterogeneous cores, Diffusion Theory w/Std, FD, FDSt.

	Core 1			Core 2			Core 3		
Egy Grp	Std	FD	FDSt	Std	FD	FDSt	Std	FD	FDSt
1	2.00	1.82	**1.84**	2.57	2.13	**2.22**	3.58	3.35	3.70
2	1.08	1.15	**0.95**	1.62	2.92	**1.56**	3.02	5.53	4.25
$error_k$	0.16	0.25	0.24	-0.43	-0.61	**-0.31**	-1.18	-0.79	-1.05

4.4 CALCULATION OF THE DERIVATIVE OF THE FLUX

In the final section the calculation and accuracy of the derivative of the flux, which is a term of the FD diffusion coefficient, is examined. Two methods of calculating the derivative were considered. One used *n*th order least squares polynomials and the other used cubic splines. Each method uses a polynomial to approximate the spatial shape of the flux, and the first derivative of the polynomial is analytically determined to calculate the flux gradient.

Figure 4.58 shows the normalized flux in group 2 of a two-group calculation in assemblies 3 and 4, both having highly absorbing regions. Because of the strong spatial variation of the flux in these two assemblies a single least squares polynomial, of order as high as 7, would not fit all of the flux data points with adequate accuracy, and the domain would have to be divided into two separate regions with a separate polynomial for each region. However, the point at which this division is made varies with energy group and assembly type. When performing calculations in 2, 4, and 47 energy groups, with four different assembly types, and also three different fine-mesh full-cores, this process would require excessive user input and become prohibitively tedious and time-consuming.

The cubic spline method does not have these drawbacks and was eventually used for all of the gradient calculations. There are also limitations of the cubic spline method, but the only one of major concern that was analyzed in depth is the adequate smoothness of the flux output by the transport calculation that was used to calculate the cubic spline polynomials. The fluxes in Figure 4.58 present some of the most significant spatial

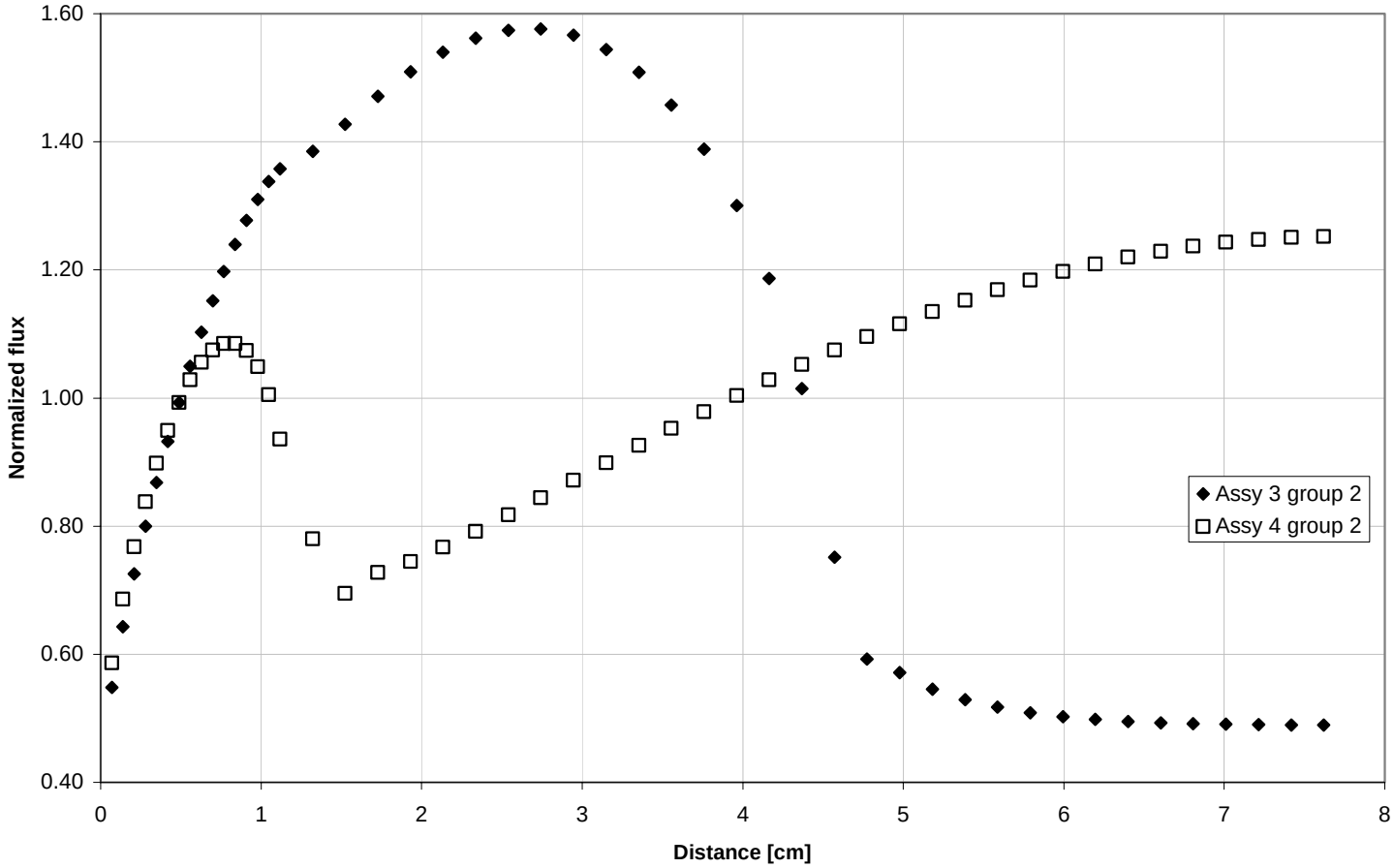

Figure 4.58: Normalized flux, Heterogeneous half-assemblies 3 and 4, Transport Theory Results, Vacuum BCs, group 2 of 2.

variations encountered in this thesis, but the gradients in Figure 4.59 calculated based on them using cubic splines are smooth.

A problem that presents a greater challenge to the splines method is the fine-mesh full core case for energy group 1, mainly in the water region near the problem boundary. The plot in Figure 4.60 shows the transport theory scalar flux output in the water region and the first fuel region, with slightly noticeable instabilities in the water region and to a lesser degree in the beginning of the fuel region, which all comprise about the first two dozen points inside the assembly. The lines connecting the data points have been added to make the trends more apparent. Also shown in Figure 4.60 is the gradient calculated based on cubic splines using these flux data points. The more noticeable instabilities in the gradient are caused by the instabilities in the flux. The important consideration is the effect these oscillations in the gradient have on the diffusion coefficient that uses these gradients in Eq. (2.16) on page 20. The FD diffusion coefficients calculated using these gradients are shown in Figure 4.61, along with the Std diffusion coefficients for comparison. The flux-errors obtained from using these FD and Std diffusion coefficients in a fine-mesh diffusion theory model of the full-core are shown in Figure 4.62, and indicate that the oscillations in the flux gradient and the FD diffusion coefficients have not significantly affected the flux calculated using the FD diffusion coefficient.

Only group 1 of the fine-mesh full-core calculations exhibit instabilities in the gradient as severe as in Figure 4.61, which occur because of insufficient convergence. The single-assembly calculations were all much more converged. Because the group 1 fine-mesh full-core cases represent the worst case scenarios as far as flux-gradient stability is concerned, and its final flux result was not significantly affected by these

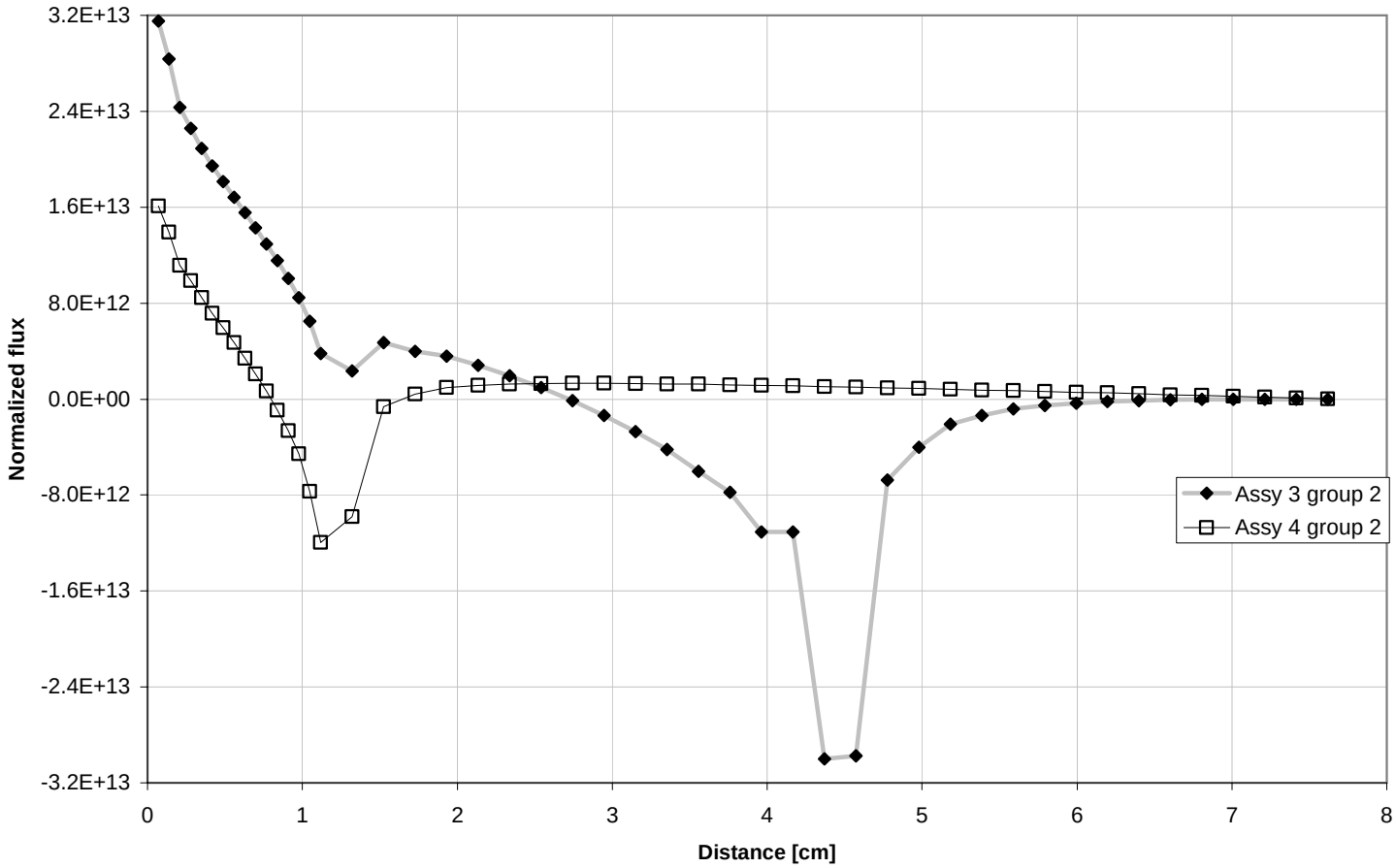

Figure 4.59: Gradient, calculated using cubic splines, in heterogeneous half-assemblies 3 and 4 with vacuum BCs, group 2 of 2.

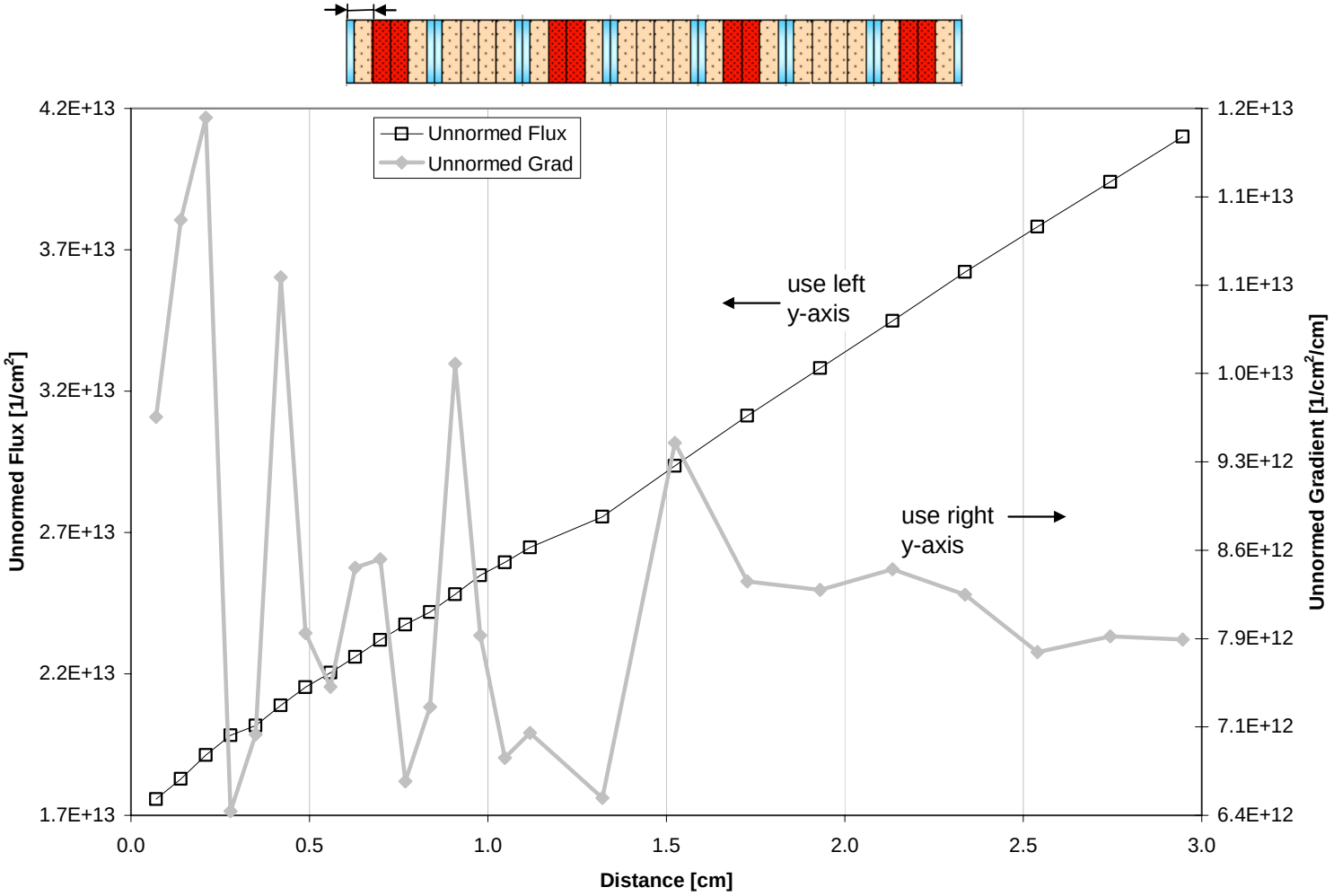

Figure 4.60: Unnormalized transport flux and its cubic splines gradient, Group 1 of 2, Heterogeneous assembly region 1 (Assy type 2) in core 1.

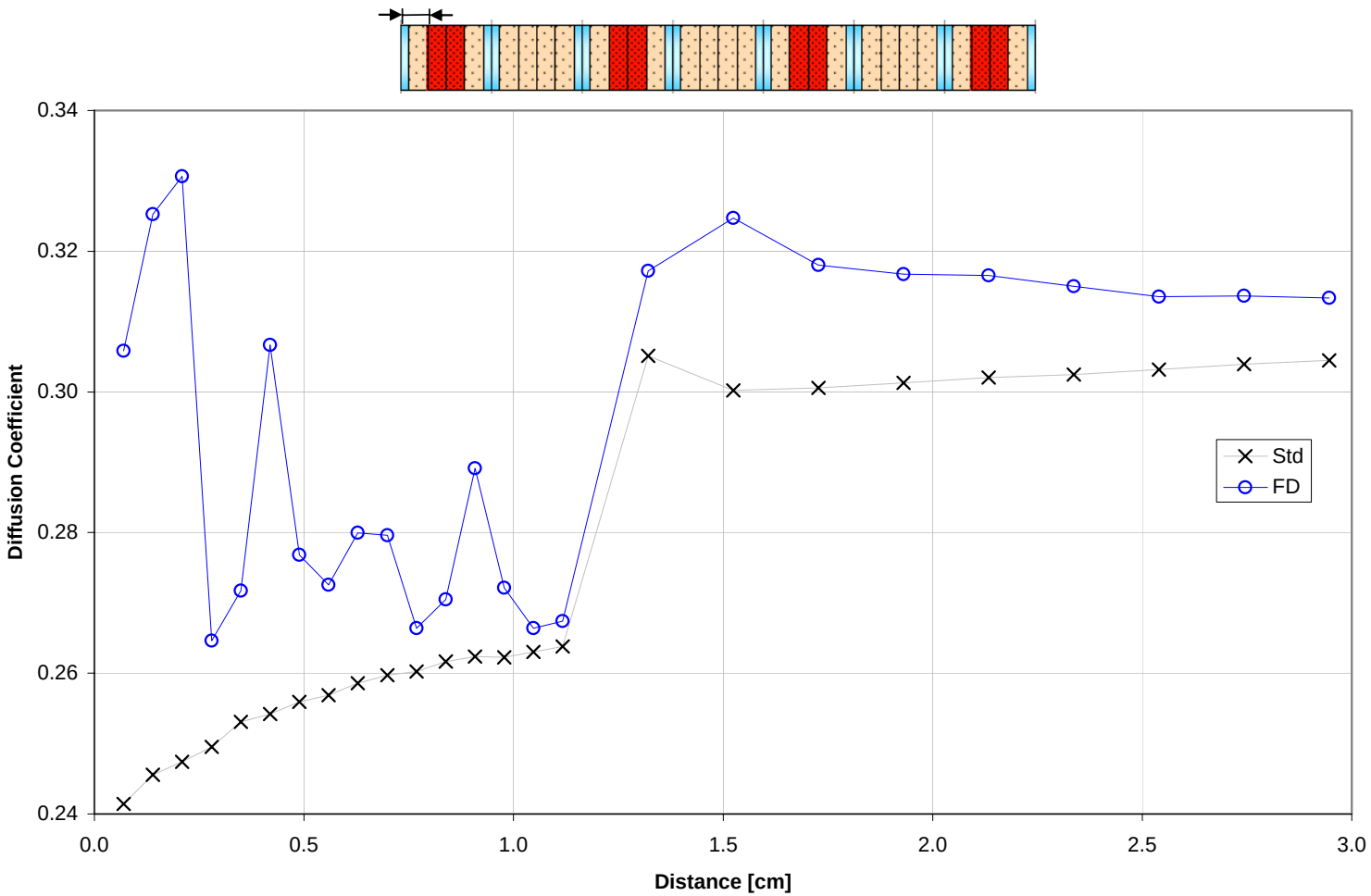

Figure 4.61: Diffusion Coefficients, Group 1 of 2, Hetero Half-assy region 1 (Assy type 2) in core 1.

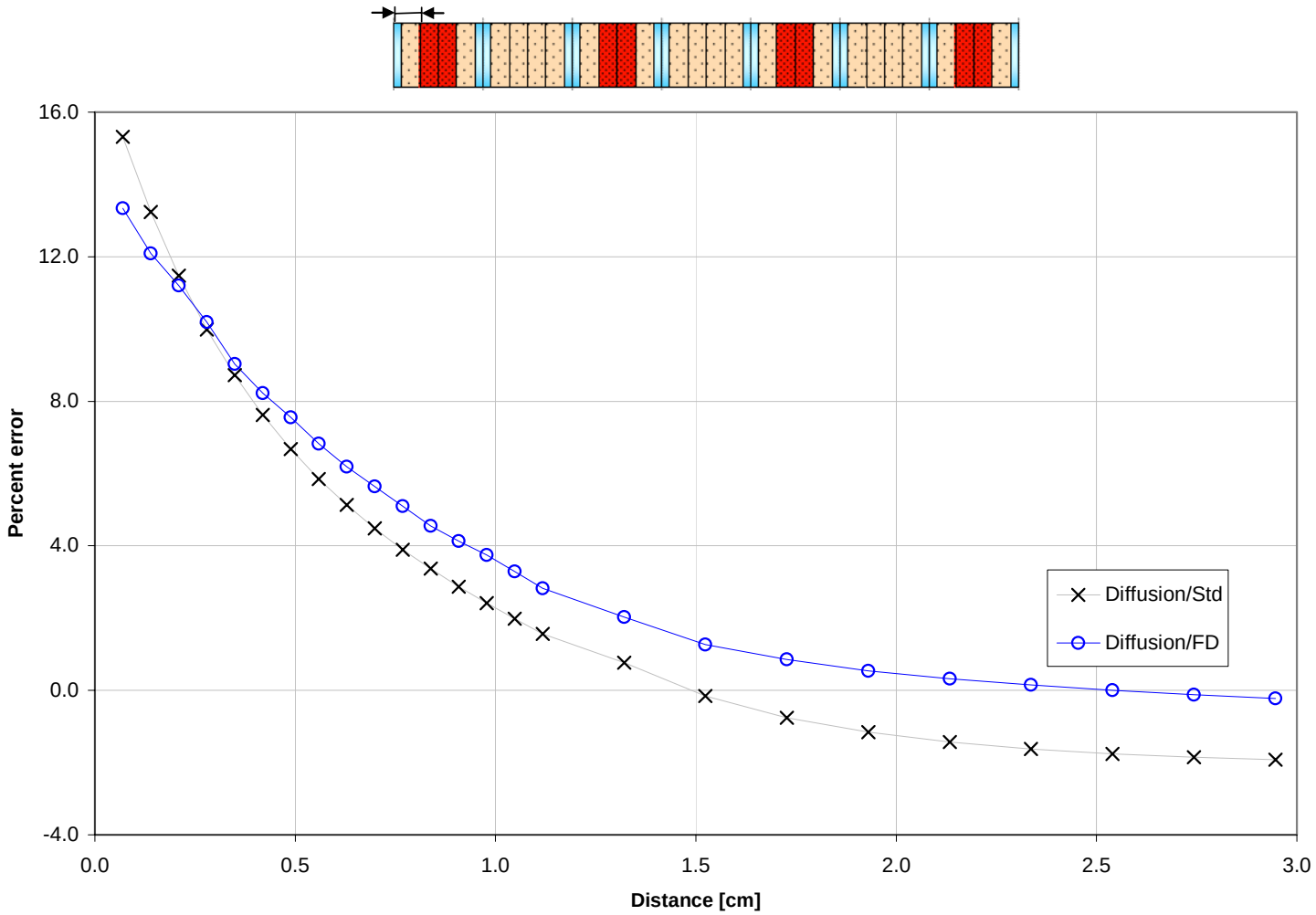

Figure 4.62: Normed flux Perc Err, group 1 of 2, Hetero Half-assy region 1 (Assy type 2) in core 1, Diffusion Thy. w/Std, FD.

instabilities, the other calculations in this thesis are affected to an even lesser extent and the accuracy of the gradient calculation is not a concern.

5 CONCLUSIONS

A new diffusion coefficient based on flux-limited diffusion theory (FDT) was evaluated for use in reactor physics calculations. The new diffusion coefficient, referred to as FD, has the advantage over the standard transport cross section, referred to as Std, of having greater accuracy in regions of large spatial gradients, and accounting for linearly anisotropic scattering across all energy groups. Another transport cross section more loosely based on FDT was also evaluated, and is referred to as FX. The evaluations were performed in one spatial dimension using models of single assemblies with vacuum and reflective boundary conditions, and full-cores consisting of combinations of the assemblies. The diffusion results were compared against transport benchmarks, and the energy structures consisted of 47, 4, and 2 groups.

The most significant finding is that in models of single assemblies with vacuum boundary conditions, the FD method produced the smallest pointwise flux-errors in almost all energy groups, and the smallest eigenvalue-errors, when compared against the Std and FX diffusion coefficients. The most significant improvements were flux-error reductions by about half and eigenvalue-error reductions by more than an order of magnitude when compared against the Std. These improvements took place in all energy structures tested, and resulted from the FD's advantage over the Std in the large gradients present using vacuum boundary conditions.

With single-assembly reflective boundary conditions the improvements using FD are more mixed. There are some reductions in flux-errors, but there is a strong tendency for the FD to reduce flux-errors in the fast groups while worsening them in the thermal

groups, and most of the time the eigenvalue errors increase using the FD because the systems modeled were thermally dominated light water assemblies. It was not practical to perform analyses in 47 individual energy groups, so the energy-integrated 47-group flux-errors that indicate improvements in all but assembly type 3 are suspect, and the eigenvalues worsened for all four assembly types.

In the 2-group full-core fine-mesh calculations, the FD improved flux-errors in the fast group and worsened them in the thermal group for all three core types. The eigenvalue errors were improved in only one of the core-types.

Because the single assemblies with reflective boundaries and full-cores do not have the strong flux-gradients inherent in single assemblies with vacuum boundaries, the only significant advantage of the FD compared to the Std is its accounting of linearly anisotropic scattering across all energy-groups. Because this effect is most significant in faster energy ranges, a set of calculations using the FD in fast and resonance groups (1 and 2 of 4, or 1 of 2 group calculations) and Std in epithermal and thermal groups was performed. These results show that this combination type of calculation yields the smallest flux-errors compared to any single type of diffusion coefficient used by itself.

One important result from the fine-mesh diffusion calculations is that they are consistent with previous results in the field of radiative transfer, from which FDT was derived. Levermore and Pomraning (1981) compared FDT to two other diffusion theories in a purely absorbing slab of varying thickness, and found that FDT yielded the greatest improvements over the other two with the thinnest slab, and their accuracies approached each other with the greatest slab thickness. The results in this thesis show that FD yielded the greatest improvement using single assemblies with vacuum

boundaries, and smaller improvements using single assemblies with reflective boundaries. The latter can be considered to be slabs of greater thickness, because they're infinite.

The results using FX are less impressive. In the models of single assemblies with vacuum boundary conditions, in both 4 and 2 individual groups, where the FD yielded the most significant improvements, the FX reduces flux-errors in about half as many energy groups as the FD, and the amount of error reductions are not as large. It also slightly reduces eigenvalue errors, to a much smaller extent than the FD does. In the single assembly reflective cases, as in the vacuum cases, the FX also reduces flux-errors in fewer groups than FD does, and their error reductions are not as great. The FX never reduces eigenvalue errors in these cases. In the full-core cases, it reduces flux-errors in every core type in group 1, but once again with a smaller reduction than the FD, and it reduces the eigenvalue errors in two of the three cores. The FX has been shown to be *not* flux-limited, so the term "flux-limited" should not be applied to it.

There is a strong tendency for both FD and FX to yield flux-error improvements in the higher energy groups, that is groups 1 and 2 in 4-group calculations, or group 1 in 2-group calculations. Considering both the vacuum and reflective single assembly cases, in groups 1 and 2 of the 4-group results, the FD produced the lowest flux-error 14 of 16 times, while in groups 3 and 4 it produced the lowest error only 4 of 16 times. In the 2-group results, including the 2-group fine-mesh whole-core results, the FD produced the lowest flux-error 10 out of 11 times in group 1, and only 1 out of 11 times in group 2.

Some of the improvement, or lack of it, using the FD method can be traced to its assumptions. The validity of these assumptions depend, in part, on energy group and

boundary conditions. The first assumption is the separability of the angular flux, $I_g(\boldsymbol{r},\boldsymbol{\Omega})$, into two components as

$$I_g(\boldsymbol{r},\boldsymbol{\Omega}) = \phi_g(\boldsymbol{r})\psi_g(\boldsymbol{r},\boldsymbol{\Omega}) \quad . \tag{4.6}$$

The scalar flux is assumed to carry most of the spatial and energy dependence, which allows for the approximations

$$\boldsymbol{\Omega}\cdot\nabla\psi_g = 0 \tag{4.7}$$

and

$$\psi_g = \psi_{g'} \tag{4.8}$$

to be used in the derivation of the FD. These assumptions are necessary to derive the FD. There is also the assumption that ψ_g can be approximated by the function

$$\psi_g(x,\mu) = \frac{1-\hat{\mu}_g}{2\left[1+\lambda_g R_g^2 - \mu R_g - \hat{\mu}_g\right]} \quad . \tag{4.9}$$

which avoids solving a transcendental equation.

The assumptions used to derive the FX include that in Eqs. (4.6) and (4.8), and also those inherent in the second of the P1 equations' approximation to the transport equation,

$$\frac{1}{3}\nabla\phi_g(r) + \sigma_g(r)J_g(r) = \sum_{g'=1}^{G}\sigma_{1,g'\to g}(r)J_{g'}(r) \quad , \tag{4.10}$$

which include linearly anisotropic scalar flux and no fission source.

6 POSSIBLE IMPROVEMENTS AND RECOMMENDATIONS FOR FUTURE WORK

Because linearly anisotropic scattering is most significant in faster energy ranges, the FD method is potentially very useful in fast reactors applications.

Something that would help improve the accuracy of the results using the FD method, but increase the computational expense, is the use of the transcendental formula to find a solution for the normalized angular flux $\psi(x,\mu)$, namely

$$R = \tanh^{-1}\left[\frac{R}{1+\lambda R^2}\right] + \sum_{n=1}^{N}(2n+1)K_n\psi_n Q_n\left[\left(1+\lambda R^2\right)/R\right] \tag{6.1}$$

instead of the approximation in Eq. (4.9).

Because reactor physics calculations are frequently performed in two or three spatial dimensions, it would also be useful to evaluate the FD method in more than one dimension. This would also increase the computational expense because possibly in two dimensions (depending on the coordinate system used), and definitely in three dimensions, one of the axes in the coordinate system has to be aligned in the direction of the gradient of the flux in order to derive the FD, and the gradient might point in different directions for each energy group.

It is also suggested to examine one of the *ad hoc* FDT theories. One *ad hoc* method might work well in a certain application, while in other situations another *ad hoc* method would work well.

It is also suggested to examine the application of the flux-limited diffusion coefficient in a framework using homogenization theory using discontinuity factors.

APPENDIX

A.1 FLUX-LIMITED DIFFUSION COEFFICIENT

The following is a re-derivation of the flux-limited diffusion coefficient adapted from the work by Pomraning (1984), modified for one spatial dimension and with the external source replaced by a fission source.

Start with time-independent multigroup transport equation with fission and no external source

$$\begin{aligned}\boldsymbol{\Omega}\cdot\nabla I_g\left(\boldsymbol{r},\boldsymbol{\Omega}\right)+\sigma_g I_g\left(\boldsymbol{r},\boldsymbol{\Omega}\right)=\sum_{g'=1}^{G}\int_{4\pi}d\boldsymbol{\Omega}'\sigma_{s,g'\to g}\left(\boldsymbol{\Omega}'\cdot\boldsymbol{\Omega}\right)I_{g'}\left(\boldsymbol{r},\boldsymbol{\Omega}'\right)+\\ \frac{1}{k}\frac{X_g\left(r\right)}{4\pi}\sum_{g'=1}^{G}\nu_{g'}\left(r\right)\sigma_{f,g'}\left(r\right)\int_{4\pi}d\boldsymbol{\Omega}'I_{g'}\left(\boldsymbol{r},\boldsymbol{\Omega}'\right)\end{aligned} \tag{A.1}$$

and its angle-integrated result, the multigroup conservation equation

$$\nabla\cdot\boldsymbol{J}_g+\sigma_g\phi_g\left(\boldsymbol{r}\right)=\sum_{g'=1}^{G}\sigma_{0,g'\to g}\phi_{g'}\left(\boldsymbol{r}\right)+\frac{1}{k}X_g\left(r\right)\sum_{g'=1}^{G}\nu_{g'}\left(r\right)\sigma_{f,g'}\left(r\right)\phi_{g'}\quad . \tag{A.2}$$

Separate the angular flux into two components as

$$I_g(\boldsymbol{r},\boldsymbol{\Omega})=\phi_g(\boldsymbol{r})\psi_g(\boldsymbol{r},\boldsymbol{\Omega}) \tag{A.3}$$

where $\phi_g(\boldsymbol{r})$ is the scalar flux with

$$\phi_g=\int_{4\pi}d\boldsymbol{\Omega}I_g(\boldsymbol{\Omega})\quad , \tag{A.4}$$

$\psi_g(\boldsymbol{r},\boldsymbol{\Omega})$ is the normalized angular flux, with

$$\int_{4\pi}d\Omega\,\psi_g(\boldsymbol{r},\boldsymbol{\Omega})=1\quad , \tag{A.5}$$

the current is defined as

$$\boldsymbol{J}_g = \int_{4\pi} d\boldsymbol{\Omega}\boldsymbol{\Omega} I_g(\boldsymbol{\Omega}) \quad , \tag{A.6}$$

and the normalized current defined as

$$\boldsymbol{j}_g = \frac{\boldsymbol{J}_g}{\phi_g} \quad , \tag{A.7}$$

or equivalently as

$$\boldsymbol{j}_g(\boldsymbol{r}) = \int_{4\pi} d\boldsymbol{\Omega}\boldsymbol{\Omega}\psi_g(\boldsymbol{r},\boldsymbol{\Omega}) \quad . \tag{A.8}$$

Put Eq. (A.3) into Eqs. (A.1) and (A.2) to get

$$\begin{aligned} \phi_g \boldsymbol{\Omega}\cdot\nabla\psi_g + \psi_g \boldsymbol{\Omega}\cdot\nabla\phi_g + \sigma_g\phi_g\psi_g &= \sum_{g'=1}^{G}\phi_{g'}\int_{4\pi} d\boldsymbol{\Omega}'\sigma_{s,g'\to g}(\boldsymbol{\Omega}'\cdot\boldsymbol{\Omega})\psi_{g'}(\boldsymbol{\Omega}') \\ &+\frac{1}{k}\frac{X_g(r)}{4\pi}\sum_{g'=1}^{G}\phi_{g'}\nu_{g'}\sigma_{fg'}\int d\boldsymbol{\Omega}'\psi_{g'}(\boldsymbol{\Omega}') \end{aligned} \tag{A.9}$$

and

$$\phi_g\nabla\cdot\boldsymbol{j}_g + \boldsymbol{j}_g\cdot\nabla\phi_g + \sigma_g\phi_g = \sum_{g'=1}^{G}\sigma_{0,g'\to g}\phi_{g'} + \frac{1}{k}X_g\sum_{g'=1}^{G}\nu_{g'}\sigma_{f,g'}\phi_{g'} \quad . \tag{A.10}$$

Multiply Eq. (A.10) by $\psi_g(\boldsymbol{\Omega})$ and subtract from Eq. (A.9) to get

$$\begin{aligned} &-\psi_g\phi_g\nabla\cdot\boldsymbol{j}_g - \psi_g\boldsymbol{j}_g\cdot\nabla\phi_g - \psi_g\sigma_g\phi_g + \psi_g\sum_{g'=1}^{G}\sigma_{0,g'\to g}\phi_g \\ &+\psi_g\frac{1}{k}X_g\sum_{g'=1}^{G}\nu_{g'}\sigma_{f,g'}\phi_{g'} + \phi_g\boldsymbol{\Omega}\cdot\nabla\psi_g + \psi_g\boldsymbol{\Omega}\cdot\nabla\phi_g + \sigma_g\phi_g\psi_g \\ &= \sum_{g'=1}^{G}\phi_{g'}\int d\boldsymbol{\Omega}'\sigma_{s,g'\to g}\psi_g + \frac{1}{k}\frac{X_g}{4\pi}\sum_{g'=1}^{G}\phi_{g'}\nu_{g'}\sigma_{f,g'}\int_{4\pi} d\boldsymbol{\Omega}'\psi_{g'} \end{aligned} \tag{A.11}$$

or

$$
\begin{aligned}
&\left(\boldsymbol{\Omega}\cdot\nabla\psi_g\right)\phi_g + \\
&\psi_g\left(-\phi_g\nabla\cdot\boldsymbol{j}_g - \boldsymbol{j}_g\cdot\nabla\phi_g + \sum_{g'=1}^{G}\sigma_{0,g'\to g}\phi_{g'} + \frac{1}{k}X_g\sum_{g'=1}^{G}\nu_{g'}\sigma_{f,g'}\phi_{g'} + \boldsymbol{\Omega}\cdot\nabla\phi_g\right) \\
&= \sum_{g'=1}^{G}\phi_{g'}\int_{4\pi}d\boldsymbol{\Omega}'\sigma_{s,g'\to g}\psi_{g'} + \frac{1}{k}\frac{X_g}{4\pi}\sum_{g'=1}^{G}\phi_{g'}\int_{4\pi}d\boldsymbol{\Omega}'\nu_{g'}\sigma_{f,g'}\psi_{g'} \quad .
\end{aligned}
\tag{A.12}
$$

From the assumption of Pomraning (1984), that the spatial and energy dependences are primarily carried by the scalar flux $\phi_g(\boldsymbol{r})$ and not by the normalized angular flux $\psi_g(\boldsymbol{r})$,

$$
\boldsymbol{\Omega}\cdot\nabla\psi_g = 0 \tag{A.13}
$$

and

$$
\psi_g = \psi_{g'} \quad , \tag{A.14}
$$

which implies that

$$
\nabla\cdot\boldsymbol{j} = 0 \quad . \tag{A.15}
$$

With the assumptions of Eqs. (A.13) and (A.15), Eq. (A.12) can be rewritten as

$$
\begin{aligned}
&\left(1 + \boldsymbol{j}_g\cdot\boldsymbol{R}_g - \boldsymbol{\Omega}\cdot\boldsymbol{R}_g\right)\psi_g(\boldsymbol{\Omega}) = \\
&\frac{1}{\sigma_g\omega_g\phi_g}\left[\sum_{g'=1}^{G}\phi_{g'}\int_{4\pi}d\boldsymbol{\Omega}'\sigma_{s,g'\to g}(\boldsymbol{\Omega}'\cdot\boldsymbol{\Omega})\psi_{g'}(\boldsymbol{\Omega}')\right. \\
&\left. + \frac{1}{k}\frac{X_g}{4\pi}\sum_{g'=1}^{G}\phi_{g'}\nu_{g'}\sigma_{f,g'}\int_{4\pi}d\boldsymbol{\Omega}'\psi_{g'}(\boldsymbol{\Omega}')\right]
\end{aligned}
\tag{A.16}
$$

where

$$\omega_g(\boldsymbol{r}) = \frac{1}{\sigma_g(\boldsymbol{r})\phi_g(\boldsymbol{r})}\left(\sum_{g'=1}^{G}\sigma_{0,g'\to g}(\boldsymbol{r})\phi_{g'}(\boldsymbol{r}) + \frac{1}{k}X_g(\boldsymbol{r})\sum_{g'=1}^{G}\nu_{g'}(\boldsymbol{r})\sigma_{f,g'}(\boldsymbol{r})\phi_{g'}(\boldsymbol{r})\right), \quad \text{(A.17)}$$

and $\boldsymbol{R}_g$, the dimensionless gradient of the scalar flux, is

$$\boldsymbol{R}_g(\boldsymbol{r}) = \frac{-\nabla\phi_g(\boldsymbol{r})}{\sigma_g(\boldsymbol{r})\omega_g(\boldsymbol{r})\phi_g(\boldsymbol{r})} \quad . \quad \text{(A.18)}$$

In one dimension the functions $j_g(x)$ and $R_g(x)$ are now a function of only one spatial dimension, and $j_g(x)$ is proportional to $R_g(x)$, thus

$$j_g(x) = \lambda_g R_g(x) \quad , \quad \text{(A.19)}$$

which can replace $\boldsymbol{j}_g \cdot \boldsymbol{R}_g$ in Eq. (A.16). The constant of proportionality λ_g will be determined later. Also in one dimension, μR_g replaces $\boldsymbol{\Omega}\cdot\boldsymbol{R}_g$, where μ is the cosine of the polar angle ϕ, (note that this ϕ is not the same as the scalar flux ϕ, and $\mu = \cos[\phi]$ (cosine of the polar angle) is used from here forward), the normalized angular flux becomes

$$\psi_g(\boldsymbol{\Omega}) = \frac{\psi_g(\mu)}{2\pi} \quad \text{(A.20)}$$

with the normalization

$$\int_0^{2\pi} d\theta \int_{-1}^{1} d\mu \psi_g(\boldsymbol{\Omega}) = 2\pi \int_{-1}^{1} d\mu \frac{\psi_g(\mu)}{2\pi} = \int_{-1}^{1} d\mu \psi_g(\mu) = 1 \quad , \quad \text{(A.21)}$$

and the differential scattering cross section becomes

$$\sigma_{s,g'\to g}\left(\boldsymbol{r},\boldsymbol{\Omega}'\cdot\boldsymbol{\Omega}\right)=\frac{1}{2\pi}\sigma_{s,g'\to g}\left(\mathrm{x},\mu'\cdot\mu\right)\quad , \tag{A.22}$$

with

$$\sigma_{n,g'\to g}\left(x\right)=2\pi\int_{-1}^{1}d\xi P_n\left(\xi\right)\sigma_g\left(x,\xi\right)\quad . \tag{A.23}$$

Using the one dimensional assumptions the scattering and fission terms are rewritten as

$$\begin{aligned}\int_{4\pi}d\boldsymbol{\Omega}'\sigma_{s,g'\to g}\left(\boldsymbol{\Omega}'\cdot\boldsymbol{\Omega}\right)\psi_{g'}\left(\boldsymbol{\Omega}'\right)&=\int_{0}^{2\pi}d\theta\int_{-1}^{+1}d\mu'\frac{\sigma_{s,g'\to g}\left(\mu'\cdot\mu\right)}{2\pi}\psi_{g'}\left(\mu'\right)\\&=\int_{-1}^{+1}d\mu'\sigma_{s,g'\to g}\left(\mu'\cdot\mu\right)\psi_{g'}\left(\mu'\right)\end{aligned} \tag{A.24}$$

and

$$\begin{aligned}&\frac{1}{k}\frac{X_g}{4\pi}\sum_{g'=1}^{G}\phi_{g'}\nu_{g'}\sigma_{f,g'}\int_{4\pi}d\boldsymbol{\Omega}'\psi_{g'}\left(\boldsymbol{\Omega}'\right)=\\&\frac{1}{k}\frac{X_g}{4\pi}\sum_{g'=1}^{G}\phi_{g'}\nu_{g'}\sigma_{f,g'}2\pi\int_{-1}^{1}d\mu'\frac{\psi_{g'}\left(\mu'\right)=}{2\pi}\\&\frac{1}{k}\frac{X_g}{4\pi}\sum_{g'=1}^{G}\phi_{g'}\nu_{g'}\sigma_{f,g'}\quad .\end{aligned} \tag{A.25}$$

Equation (A.16) can be now be written as

$$\begin{aligned}&\left(1+\lambda R_g^2-\mu R_g\right)\frac{\psi_g\left(x\right)}{2\pi}=\\&\frac{1}{\sigma_g\omega_g\phi_g}\left[\sum_{g'=1}^{G}\phi_{g'}\int_{-1}^{1}d\mu'\sigma_{s,g'\to g}\left(\mu'\cdot\mu\right)\psi_{g'}\left(x,\mu'\right)+\frac{1}{k}\frac{X_g}{4\pi}\sum_{g'=1}^{G}\phi_{g'}\nu_{g'}\sigma_{f,g'}\right],\end{aligned} \tag{A.26}$$

or

$$\left(1+\lambda R_g^2-\mu R_g\right)\psi_g\left(x\right)=$$
$$\frac{2\pi}{\sigma_g\omega_g\phi_g}\left[\sum_{g'=1}^{G}\phi_{g'}\int_{-1}^{1}d\mu'\sigma_{s,g'\to g}\left(\mu'\cdot\mu\right)\psi_{g'}\left(x,\mu'\right)+\frac{1}{k}\frac{X_g}{4\pi}\sum_{g'=1}^{G}\phi_{g'}\nu_{g'}\sigma_{f,g'}\right], \tag{A.27}$$

and Eq. (A.17) can be rewritten as

$$\omega_g\left(x\right)=$$
$$\frac{1}{\sigma_g\left(x\right)\phi_g\left(x\right)}\left(\sum_{g'=1}^{G}\sigma_{0,g'\to g}\left(x\right)\phi_{g'}\left(x\right)+\frac{1}{k}X_g\left(x\right)\sum_{g'=1}^{G}\nu_{g'}\left(x\right)\sigma_{f,g'}\left(x\right)\phi_{g'}\left(x\right)\right), \tag{A.28}$$

and $\boldsymbol{R}_g\left(\boldsymbol{r}\right)$ in Eq. (A.18) becomes

$$R_g\left(x\right)=\frac{-d\phi_g/dx}{\sigma_g\left(x\right)\omega_g\left(x\right)\phi_g\left(x\right)} \quad . \tag{A.29}$$

Using Eqs. (A.7), (A.18), and (A.19), a new form of Fick's Law can be derived as

$$J_g=-\frac{\lambda_g}{\sigma_g\omega_g}\frac{d\phi_g}{dx} \tag{A.30}$$

where the flux-limited diffusion coefficient D_g^{FD} can be defined as

$$D_g^{FD}\left(x\right)=\frac{\lambda_g}{\sigma_g\left(x\right)\omega_g\left(x\right)} \quad . \tag{A.31}$$

where λ_g is still undefined. Once it is found, the expression for the flux-limited diffusion coefficient is complete.

To determine λ_g, we continue by defining an integrand on the RHS of Eq. (A.27) as

$$K_g\left(\mu'\cdot\mu\right)=\frac{2\pi}{\sigma_g\omega_g\phi_g}\left[\sum_{g'=1}^{G}\phi_{g'}\sigma_{s,g'\to g}\left(\mu'\cdot\mu\right)+\frac{1}{k}\frac{X_g}{4\pi}\sum_{g'=1}^{G}\phi_{g'}\nu_{g'}\sigma_{f,g'}\right] \tag{A.32}$$

so that

$$\left(1+\lambda_g R_g^2-\mu R_g\right)\psi_g\left(\mu\right)=\int_{-1}^{1}d\mu' K_g\left(\mu'\cdot\mu\right)\psi_g\left(\mu'\right) \quad . \tag{A.33}$$

Now assume K_g can be expanded in Legendre polynomials as

$$K_g(\mu'\cdot\mu)=\sum_{n=0}^{N}\left(\frac{2n+1}{2}\right)K_{n,g}P_n(\mu'\cdot\mu) \quad , \tag{A.34}$$

where

$$K_{n,g}=\int_{-1}^{1}d\xi P_n(\xi)K_g(\xi) \quad , \tag{A.35}$$

with $K_{0,g}=1$. To prove that $K_{0,g}=1$, simply put the definition of K_g given by Eq. (A.32) into Eq. (A.35) and use the definition of $\omega(x)$ given by Eq. (A.28),

$$\begin{aligned}
K_{0,g}&=\int_{-1}^{1}d\xi P_0(\xi)K_g(\xi)\\
&=\frac{1}{\sigma_g\omega_g\phi_g}\left[\sum_{g'=1}^{G}\phi_{g'}2\pi\int_{-1}^{1}d\xi\sigma_{s,g'\to g}(\xi)+\frac{1}{k}\frac{2\pi X_g}{4\pi}\sum_{g'=1}^{G}\phi_{g'}\nu_{g'}\sigma_{f,g'}\int_{-1}^{1}d\xi\right]\\
&=\frac{1}{\sigma_g\omega_g\phi_g}\left[\sum_{g'=1}^{G}\phi_{g'}\sigma_{0,g'\to g}+\frac{1}{k}X_g\sum_{g'=1}^{G}\phi_{g'}\nu_{g'}\sigma_{f,g'}\right]\\
&=\frac{\sum_{g'=1}^{G}\phi_{g'}\sigma_{0,g'\to g}+\frac{1}{k}X_g\sum_{g'=1}^{G}\phi_{g'}\nu_{g'}\sigma_{f,g'}}{\sum_{g'=1}^{G}\phi_{g'}\sigma_{0,g'\to g}+\frac{1}{k}X_g\sum_{g'=1}^{G}\phi_{g'}\nu_{g'}\sigma_{f,g'}} \quad ,
\end{aligned} \tag{A.36}$$

which implies that

$$K_{0,g}=1 \quad . \tag{A.37}$$

Similarly, one can explicitly prove $K_{1,g} \le 1$ by writing

$$K_{1,g} = \int_{-1}^{1} d\xi \xi K_g(\xi)$$
$$= \frac{1}{\sigma_g \omega_g \phi_g} \left[2\pi \int_{-1}^{1} d\xi \xi \sum_{g'=1}^{G} \phi_{g'} \sigma_{s,g' \to g}(\xi) + \frac{2\pi X_g}{4\pi} \sum_{g'=1}^{G} \phi_{g'} \nu_{g'} \sigma_{f,g'} \int_{-1}^{1} d\xi \xi \right] \qquad \text{(A.38)}$$
$$= \frac{1}{\sigma_g \omega_g \phi_g} \left[\sum_{g'=1}^{G} \phi_{g'} \sigma_{1,g' \to g} + 0 \right] \quad ,$$

and

$$\hat{\mu}_g \equiv K_{1,g} = \frac{\sum_{g'=1}^{G} \phi_{g'} \sigma_{1,g' \to g}}{\sum_{g'=1}^{G} \phi_{g'} \sigma_{0,g' \to g} + \frac{1}{k} X_g \sum_{g'=1}^{G} \phi_{g'} \nu_{g'} \sigma_{f,g'}} \le 1 \quad , \qquad \text{(A.39)}$$

and the $K_{n,g}$ converge.

The results of Eqs. (A.37) and (A.39) will be used later. Note that the expression derived in Eq. (A.39) for $\hat{\mu}_g$ is the same as Pomraning's (1984) expression for $\hat{\mu}_g$ with the external source once again replaced by a fission source, and also that $\hat{\mu}_g$ would equal the standard $\bar{\mu}_g$, the average of the cosine of the neutron scattering angle, with the absence of the fission source, as with Pomraning's $\hat{\mu}_g$ with the absence of an external source.

With the approximation of Eq. (A.34), Eq. (A.33) can be rewritten as

$$\left(1 + \lambda_g R_g^2 - \mu R_g\right) \psi_g(\mu) = \sum_{n=0}^{N} \left(\frac{2n+1}{2} \right) P_n(\mu) K_{n,g} \psi_{n,g} \quad , \qquad \text{(A.40)}$$

or by using Eq. (A.37) as

$$\left(1+\lambda_g R_g^2-\mu R_g\right)\psi_g\left(\mu\right)=\frac{1}{2}+\sum_{n=1}^{N}\left(\frac{2n+1}{2}\right)P_n(\mu)K_{n,g}\psi_{n,g} \quad , \tag{A.41}$$

where

$$\psi_{n,g}=\int_{-1}^{1} d\mu P_n\left(\mu\right)\psi_g\left(\mu\right) \quad . \tag{A.42}$$

and with the normalization in Eq. (A.21) and Eq. (A.42) one has,

$$\psi_{0,g}=1 \quad . \tag{A.43}$$

By integrating Eq. (A.41) over the polar angle μ, using Eq. (A.42) and the orthogonality condition of Legendre polynomials one has

$$1+\lambda_g R_g^2-R_g\underbrace{\int_{-1}^{1} d\mu\mu\psi_g}_{=\psi_{1,g}}=1+\underbrace{\int_{-1}^{1} d\mu\sum_{n=1}^{N}\left(\frac{2n+1}{2}\right)P_n(\mu)K_{n,g}\psi_{n,g}}_{=0} \tag{A.44}$$

and

$$\psi_{1,g}=\lambda_g R_g \quad . \tag{A.45}$$

The results of Eq. (A.45) will also be used later.

To find a solution to Eq. (A.41) the function

$$\psi_g=\frac{1}{2\left[1+C_g R_g\left(\lambda_g R_g-\mu\right)\right]} \tag{A.46}$$

is assumed to adequately represent the solution. Functions similar to this have previously been used for ψ (Levermore and Pomraning 1981, Sanchez and Pomraning 1991). The

constant C_g is determined using a Galerkin type of procedure. Equation (A.41) is multiplied by a weight function W_g, which is chosen to be $1+C_gR_g\left(\lambda_gR_g-\mu\right)$, and integrated over all μ to get

$$\int_{-1}^{1} d\mu\left(1+\lambda_g R_g^2-\mu R_g\right)\frac{\cancel{\left[1+C_gR_g\left(\lambda_gR_g-\mu\right)\right]}}{2\cancel{\left[1+C_gR_g\left(\lambda_gR_g-\mu\right)\right]}}=$$
$$\int_{-1}^{1} d\mu\frac{\left[1+C_gR_g\left(\lambda_gR_g-\mu\right)\right]}{2}+\int_{-1}^{1} d\mu\left[1+C_gR_g\left(\lambda_gR_g-\mu\right)\right]\sum_{n=1}^{N}\left(\frac{2n+1}{2}\right)P_n(\mu)K_{n,g}\psi_{n,g}\ . \tag{A.47}$$

The LHS of Eq. (A.47) is

$$\int_{-1}^{1} d\mu\frac{\left(1+\lambda_gR_g^2-\mu R_g\right)}{2}=\frac{1}{2}\left\{\int_{-1}^{1} d\mu+\int_{-1}^{1} d\mu\lambda_gR_g^2+R_g\int_{-1}^{1} d\mu\mu\right\} \tag{A.48}$$
$$=1+\lambda_gR_g^2+0\ .$$

The first term on the RHS of Eq. (A.47) is

$$\int_{-1}^{1} d\mu\frac{\left[1+C_gR_g\left(\lambda_gR_g-\mu\right)\right]}{2}=\frac{1}{2}\int_{-1}^{1} d\mu+\frac{C_g\lambda_gR_g^2}{2}\int_{-1}^{1} d\mu-\frac{C_gR_g}{2}\int_{-1}^{1} d\mu\mu \tag{A.49}$$
$$=1+C_g\lambda_gR_g^2+0\ .$$

The second term on the RHS of Eq. (A.47) can be rewritten using the orthogonality relation of Legendre polynomials, and Eq. (A.39) and (A.45) is,

$$\begin{aligned}
&\int_{-1}^{1} d\mu\left[1+C_g R_g\left(\lambda_g R_g-\mu\right)\right]\sum_{n=1}^{N}\left(\frac{2n+1}{2}\right)P_n(\mu)K_{n,g}\psi_{n,g}= \\
&\underbrace{\int_{-1}^{1} d\mu\sum_{n=1}^{N}\left(\frac{2n+1}{2}\right)P_n K_{n,g}\psi_{n,g}}_{=0}+C_g\lambda_g R_g^2\underbrace{\int_{-1}^{1} d\mu\sum_{n=1}^{N}\left(\frac{2n+1}{2}\right)P_n(\mu)K_{n,g}\psi_{n,g}}_{=0} \\
&-C_g R_g\underbrace{\int_{-1}^{1} d\mu\mu\sum_{n=1}^{N}\left(\frac{2n+1}{2}\right)P_n(\mu)K_{n,g}\psi_{n,g}}_{=0 \text{ for } n\neq 1} = -C_g R_g\frac{3}{2}\frac{2}{3}\hat{\mu}_g\lambda_g R_g \\
&\qquad\qquad = -C_g R_g^2\hat{\mu}_g\lambda_g \quad .
\end{aligned} \tag{A.50}$$

Adding the above result to Eq. (A.49) to complete the rewritten RHS of Eq. (A.47) and equating it to the rewritten LHS side of Eq. (A.47), which is now Eq. (A.48), yields,

$$1+\lambda_g R_g^2 = 1+C_g\lambda_g R_g^2\left(1-\hat{\mu}_g\right) \tag{A.51}$$

which can be solved to yield an expression for C_g as

$$C_g = \frac{1}{1-\hat{\mu}_g} \quad . \tag{A.52}$$

The solution to Eq. (A.41) now is

$$\psi_g\left(x,\mu\right) = \frac{1}{2\left[1+\dfrac{R_g\left(\lambda_g R_g-\mu_g\right)}{1-\hat{\mu}_g}\right]} \tag{A.53}$$

or

$$\psi_g\left(x,\mu\right) = \frac{1-\hat{\mu}_g}{2\left[1+\lambda_g R_g^2-\mu R_g-\hat{\mu}_g\right]} \tag{A.54}$$

When this expression for ψ_g is used in the normalization condition, Eq. (A.21), one gets

$$1 = \int_{-1}^{1} d\mu \psi_g(\mu) = \frac{1-\hat{\mu}_g}{2} \int_{-1}^{1} \frac{d\mu}{1+\lambda_g R_g^2 - \hat{\mu}_g - \mu R_g} \quad , \tag{A.55}$$

and by solving the integral in Eq. (A.55), which is equal to 1, an explicit expression for λ_g is found as

$$\lambda_g = \frac{1}{R_g} \left\{ \frac{1+\exp\left[-2R_g/\left(1-\hat{\mu}_g\right)\right]}{1-\exp\left[-2R_g/\left(1-\hat{\mu}_g\right)\right]} - \frac{1-\hat{\mu}_g}{R_g} \right\} \tag{A.56}$$

or

$$\lambda_g = \frac{1}{R_g} \left\{ \coth\left[\frac{R_g}{1-\hat{\mu}_g}\right] - \frac{1-\hat{\mu}_g}{R_g} \right\} \quad . \tag{A.57}$$

This value of λ_g can now be used in Eq. (A.31), and an explicit expression for the flux-limited diffusion coefficient is found. By inserting the expression for λ_g in Eq. (A.57) into the expression for the diffusion coefficient in Eq. (A.31), and using the definitions of ω_g in Eq. (A.28), R_g in Eq. (A.29), $\hat{\mu}_g$ in Eq. (A.39), one arrives at a single expression for the spatially dependent flux-limited diffusion coefficient as

$$D_g^{FD}(x) = \frac{-\phi_g(x)}{d\phi_g/dx} \times$$

$$\left\{ \coth\left[\frac{-d\phi_g/dx}{\left(\sum_{g'=1}^{G} \sigma_{0,g'\to g}(x)\phi_{g'}(x) + \frac{1}{k} X_g(x) \sum_{g'=1}^{G} \nu_{g'}(x)\sigma_{f,g'}(x)\phi_{g'}(x) \right)\left(1-\hat{\mu}_g\right)} \right] \right.$$

$$\left. + \frac{\left(\sum_{g'=1}^{G} \sigma_{0,g'\to g}(x)\phi_{g'}(x) + \frac{1}{k} X_g(x) \sum_{g'=1}^{G} \nu_{g'}(x)\sigma_{f,g'}(x)\phi_{g'}(x) \right)\left(1-\hat{\mu}_g\right)}{d\phi_g/dx} \right\}$$

(A.58)

or

$$D_g^{FD}(x) = \frac{-\phi_g(x)}{d\phi_g/dx} \times$$

$$\left\{ \coth\left[\frac{-d\phi_g/dx}{\sum_{g'=1}^{G} \phi_{g'}\sigma_{0,g'\to g} - \sum_{g'=1}^{G} \phi_{g'}\sigma_{1,g'\to g} + \frac{1}{k} X_g \sum_{g'=1}^{G} \phi_{g'}\nu_{g'}\sigma_{f,g'}} \right] \right.$$

$$\left. + \frac{\sum_{g'=1}^{G} \phi_{g'}\sigma_{0,g'\to g} - \sum_{g'=1}^{G} \phi_{g'}\sigma_{1,g'\to g} + \frac{1}{k} X_g \sum_{g'=1}^{G} \phi_{g'}\nu_{g'}\sigma_{f,g'}}{d\phi_g/dx} \right\} . \quad \text{(A.59)}$$

A.2 "FLUX-LIMITED" TRANSPORT CROSS SECTION

The "flux-limited" transport cross section can be derived by separating the angular flux $I_g(r,\Omega)$ into a product of two components as

$$I_g(r,\Omega) = \phi_g(r)\psi_g(r,\Omega) \tag{A.60}$$

where $\phi_g(r)$ is the scalar flux and can be written in terms of the angular flux as

$$\phi_g(r) = \int_{4\pi} d\Omega I_g(r,\Omega) \ , \tag{A.61}$$

and $\psi_g(r,\Omega)$ is the normalized angular flux and is normalized as

$$\int_{4\pi} d\Omega \psi_g(r,\Omega) = 1 \ . \tag{A.62}$$

If it is assumed that the $\psi_g(r,\Omega)$ is independent of energy group, Eq. (A.60) can be written as

$$I_g(r,\Omega) = \phi_g(r)\psi(r,\Omega) \tag{A.63}$$

and we can also write

$$\psi(r,\Omega) = \frac{I_{g'}(r,\Omega)}{\phi_{g'}(r)} = \frac{I_g(r,\Omega)}{\phi_g(r)} \ . \tag{A.64}$$

The linear operator $\int_{4\pi} d\Omega\Omega$ can be applied to Eq. (A.64) to get

$$\frac{\int_{4\pi} d\Omega\Omega I_{g'}(r,\Omega)}{\phi_{g'}(r)} = \frac{\int_{4\pi} d\Omega\Omega I_g(r,\Omega)}{\phi_g(r)} \ , \tag{A.65}$$

and because the neutron current is defined as

$$J_g(r) = \int_{4\pi} d\Omega\Omega I_g(r,\Omega) \ , \tag{A.66}$$

Eq. (A.65) can be rewritten as

$$J_{g'} = J_g\left(\frac{\phi_{g'}}{\phi_g}\right). \tag{A.67}$$

The P1 approximation to the transport equation is

$$\nabla \cdot J_g(r) + \sigma_g(r)\phi_g(r) = \sum_{g'=1}^{G} \sigma_{0,g'\to g}(r)\phi_{g'}(r) \tag{A.68}$$

and

$$\frac{1}{3}\nabla\phi_g(r) + \sigma_g(r)J_g(r) = \sum_{g'=1}^{G} \sigma_{1,g'\to g}(r)J_{g'}(r) \ . \tag{A.69}$$

By substituting the value of $J_{g'}$ in Eq. (A.67) for $J_{g'}$ in the vector P1 equation,

Eq. (A.69), the following equation can be derived,

$$J_g = \frac{1}{3\left(\sigma_g - \sum_{g'=1}^{G} \sigma_{1,g'\to g}\left(\phi_{g'}/\phi_g\right)\right)}\nabla\phi_g \ , \tag{A.70}$$

that yields the spatially dependent "flux-limited" transport cross section

$$\sigma_{tr,g}^{FX} = \sigma_g - \sum_{g'=1}^{G} \sigma_{1,g'\to g}\left(\frac{\phi_{g'}}{\phi_g}\right) \ . \tag{A.71}$$

REFERENCES

Benoist, P. 1959. Formulation générale et Calcul Pratique du Coefficient de Diffusion dans un Réseau Comportan de Cavités, Rep. CEA-1354, Commissariat a L'Energie Atomique, Saclay.

Benoist, P. 1959. Formulation générale et calcul pratique du coefficient de diffusion dans un réseau comportan de cavités. *Reactor Science* 13:97.

Benoist, P. 1964. Théorie du Diffusion des Neutrons dans un Réseau Comportant des Cavités, Rep. CEA-R-2278, Commissariat a L'Energie Atomique, Saclay.

Benoist, P. 1968. Streaming Effects and Collision Probabilities in Lattices. *Nucl Sci Eng* 34:295.

Briesmeister, J.F. (Ed.), 1997. MCNP™—A General Monte Carlo Code N–Particle Transport Code, Version 4B. LA–12625–M. Los Alamos National Laboratory.

Candelore, N.R., R. C. Gast, and L.A. Ondis II, 1978. RCP01-A Monte Carlo Program for Solving Neutron and Photon Transport Problems in Three-dimensional Geometry with Detailed Energy Description. WAPD-TM-1267. Bettis Atomic Power Laboratory, West Mifflin, PA.

Chapman, S., and T.G. Cowling. 1970. The Mathematical Theory of Non-Uniform Gases. Cambridge, U.K.: Cambridge University Press.

Deniz, V. 1967. Study of the Kinetics of Thermalized Neutron Populations in Multiplying or Nonmultiplying Heterogeneous Media. *Nucl Sci Eng* 28:397-403.

Deniz, V.C. 1986. The theory of neutron leakage in reactor lattices. In Ronen, Y. ed., CRC Handbook of Nuclear Reactor Calculations, Vol II. New York: CRC Press.

Dorr, M.R., J.F. Painter, and S.T. Perkins. 1986. A Flux-Limited Diffusion Model for Charged-Particle Transport. *Nucl Sci Eng* 94:157-166.

Duderstadt, J.J., and W.R. Martin. 1979. Transport Theory. New York: John Wiley & Sons Inc.

Gast, R.C., 1981. A procedure for obtaining neutron-diffusion coefficients from neutron-transport Monte Carlo calculations. WAPD-TM-1446. Bettis Atomic Power Laboratory, West Mifflin, PA.

Gelbard, E.M. 1974. Anisotropic Neutron Diffusion in Lattices of the Zero-Power Plutonium Reactor Experiments. *Nucl Sci Eng* 54:327-340.

Gelbard, E.M. 1983. Streaming in Lattices. *Adv Nucl Sci Technol* 15:223-400.

Gelbard, E.M., and R. Lell. 1977. Monte Carlo treatment of the fundamental-mode neutron leakage in the presence of voids. *Nucl Sci Eng* 63: 9-23.

Gelbard, E.M., D.C. Wade, R.W. Schaefer, R.E. Phyllips. 1977. Calculations of void streaming in the Argonne gas-cooled fast reactor critical experiments. *Nucl Sci Eng* 64:624-637.

Ilas, G., and Farzad Rahnema 2003. A Monte Carlo based nodal diffusion model for criticality analysis of spent fuel storage lattices. *Ann Nucl Energy* 30:1089-1108.

Köhler, P. 1975. A New Definition of the Cell Diffusion Coefficient. *Nucl Sci Eng* 57:333-344.

Larsen, E. W. 1976. Neutron Transport and Diffusion in Inhomogeneous Media. II. *Nucl Sci Eng* 60:357-368.

Levermore, C.D., and G.C. Pomraning. 1981. A Flux-Limited Diffusion Theory. *Nucl Sci Eng* 248:321-334.

Maynard, M.S., 1959. Blackness Theory and Coefficients for Slab Geometry. *Nucl Sci Eng* 6:174-186.

Milgram, M.S., 1997. Estimation of axial diffusion processes by analog Monte Carlo: theory, tests and examples. *Ann Nucl Energy* 24:671-704.

Olson, G. L., L. H. Auer, and M. L. Hall. 2000. Diffusion, P_1, and other approximate forms of radiation transport. *J Quant Spectrosc Radiat Transfer* 64:619-634.

Pomraning, G.C. 1981. Maximum entropy Eddington factors and flux limited diffusion theory. *J Quant Spectrosc Radiat Transfer* 26:385-388.

Pomraning, G.C. 1982. Flux limiters and Eddington Factors. *J Quant Spectrosc Radiat Transfer* 27:517-530.

Pomraning, G.C. 1983. Flux-Limited Diffusion and Fokker-Planck Equations. *Nucl Sci Eng* 85:116-126.

Pomraning, G.C. 1984. Flux-limited diffusion theory with anisotropic scattering. *Nucl Sci Eng* 86:335-343.

Pomraning, G.C. 1986. On Levermore Diffusion Theory. *J Quant Spectrosc Radiat Transfer* 36:325-337.

Pounders, Justin M. 2006. Stochastically Generated Multigroup Diffusion Coefficients. Master's Thesis, Georgia Institute of Technology.

Sanchez, R. and G.C. Pomraning. 1991. A Family of Flux-limited Diffusion Theories. *Nucl Sci Eng* 45:313-337.

Stamm'ler, Rudi J.J., and Máximo J. Abbate. 1983. *Methods of steady-state reactor physics in nuclear design.* London: Academic Press Inc.

Szilard, R.H. and G.C. Pomraning. 1992. Numerical Transport and Diffusion Methods in Radiative Transfer. *Nucl Sci Eng* 112:256-269.